



## "Search for an extended scalar sector through the $H \rightarrow ZA \rightarrow l+l-bb$ process in pp collisions at $\sqrt{s}=13$ TeV"

Saggio, Alessia

### ABSTRACT

The validity of the Standard Model (SM) of particle physics, has been remarkably proven by a large programme of experimental researches, culminating in the discovery of the Higgs boson in 2012 at CERN. Despite this, the existence of new physics is strongly suggested by the inability of the SM to explain in a satisfactory way some observed phenomena, such as the existence of dark matter and the matter/antimatter asymmetry in the Universe. To overcome these problems, many theoretical models beyond the SM predicting the existence of new particles are postulated. Among these, the two-Higgs-doublet model (2HDM) is one of the simplest extensions of the SM scalar sector, and entails the presence of five new bosons. In this thesis, the search for two of these particles, H and A, is presented. The search is performed through a statistical analysis of the data collected by the CMS experiment at the CERN Large Hadron Collider (LHC) during 2016 at a center-of-mass energy of 13 TeV and integrated...

### CITE THIS VERSION

Saggio, Alessia. *Search for an extended scalar sector through the  $H \rightarrow ZA \rightarrow l+l-bb$  process in pp collisions at  $\sqrt{s}=13$  TeV*. Prom. : Delaere, Christophe <http://hdl.handle.net/2078.1/225607>

Le dépôt institutionnel DIAL est destiné au dépôt et à la diffusion de documents scientifiques émanants des membres de l'UCLouvain. Toute utilisation de ce document à des fins lucratives ou commerciales est strictement interdite. L'utilisateur s'engage à respecter les droits d'auteur liés à ce document, principalement le droit à l'intégrité de l'œuvre et le droit à la paternité. La politique complète de copyright est disponible sur la page [Copyright policy](#)

DIAL is an institutional repository for the deposit and dissemination of scientific documents from UCLouvain members. Usage of this document for profit or commercial purposes is strictly prohibited. User agrees to respect copyright about this document, mainly text integrity and source mention. Full content of copyright policy is available at [Copyright policy](#)

**Search for an extended scalar sector  
through the  $H \rightarrow ZA \rightarrow \ell^+ \ell^- b \bar{b}$  process in  
pp collisions at  $\sqrt{s} = 13$  TeV**

Doctoral dissertation presented by

**Alessia Saggio**

in fulfilment of the requirements for the degree of Doctor in Sciences

**Jury de thèse**

Prof. Christophe Delaere (Supervisor)	UCLouvain, Belgium
Dr. Tommaso Dorigo	INFN Padova, Italy
Prof. Ben Kilminster	UZH, Switzerland
Prof. Vincent Lemaître (President)	UCLouvain, Belgium
Prof. Fabio Maltoni (Secretary)	UCLouvain, Belgium

---

*December 16<sup>th</sup>, 2019*



## Acknowledgments

First of all I would like to thank my supervisor, Christophe Delaere, for the guidance that I received over the past four years and for the precious feedback on the work presented in this thesis. Thank you for the support that you showed me in pursuing new projects and for the great working environment that you provided for the CMS group. It was truly a great pleasure to work with you.

I would also like to thank Vincent Lemaître and Fabio Maltoni for the fruitful and enlightening conversations that we have had over the past years. Thank you to Tommaso Dorigo and Ben Kilminster for the valuable feedback during the private defense, that also helped to improve the quality of this manuscript. A special thank you to Tommaso Dorigo and all the members of the AMVA4New-Physics network for the invaluable opportunities that I was given and for all the things that I had the chance to learn. It was a real pleasure to be part of this project.

A very special thank you to (rigorously in alphabetical order) Ambresh Shivaji, Claudio Caputo, Ken Mimasu, Luca Mantani, Manoj Mandal, Pieter David and Pietro Vischia for the countless things that I learned from you and for the support that you always gave me: you are truly amazing!

I would also like to thank Andrea Giammanco, for the precious advice that I always received from you, and that I value a lot; thank you to Miguel Vidal and Olivier Bondu for the support during the first years of my PhD; and to all my friends and colleagues, you made my stay at CP3 the best that I could possibly ask for.

I am very thankful to Carinne Mertens for the excellent administrative support: it was essential.

Un enorme grazie ai miei genitori, a Valeria e a tutta la mia famiglia, per essere sempre stati il mio punto di riferimento durante questi anni (e lo sarete sempre). Grazie di cuore a tutti.



This Report is part of a project that has received funding from the **European Union's Horizon 2020 research and innovation programme** under grant agreement N°675440



# Contents

<b>Introduction</b>	<b>9</b>
<b>1 The scalar sector of the Standard Model</b>	<b>11</b>
1.1 Particles and forces . . . . .	11
1.2 The SM Lagrangian . . . . .	12
1.2.1 The Brout-Englert-Higgs mechanism: breaking the symmetry . . . . .	14
1.3 Higgs physics at the LHC . . . . .	16
1.4 The Standard Model open questions . . . . .	18
<b>2 Extending the Standard Model</b>	<b>21</b>
2.1 A theoretical overview . . . . .	21
2.2 Phenomenology of the 2HDM . . . . .	24
2.2.1 The 2HDM mass spectrum . . . . .	26
2.3 2HDM physics at the LHC . . . . .	28
2.4 What we know so far: the 2HDM current experimental status . . . . .	29
2.5 The SMEFT: a brief overview . . . . .	32
<b>3 The CMS experiment, object reconstruction, and simulation</b>	<b>33</b>
3.1 Physics at CERN . . . . .	33
3.1.1 A proton's journey: destination LHC . . . . .	34
3.1.2 Luminosity and pileup . . . . .	35
3.1.3 A long-term plan: towards High-Luminosity LHC . . . . .	37
3.2 The CMS detector . . . . .	40
3.2.1 The inner tracker . . . . .	41
3.2.2 The CMS calorimeters . . . . .	43
3.2.3 The muon detector . . . . .	46
3.2.4 The trigger system . . . . .	47
3.3 Object reconstruction . . . . .	49
3.3.1 Tracks and vertices . . . . .	50
3.3.2 Electrons . . . . .	52
3.3.3 Muons . . . . .	53

3.3.4	Jets . . . . .	54
3.3.5	Missing transverse energy . . . . .	58
3.4	Simulating (new) physics . . . . .	58
<b>4</b>	<b>Statistical tools and the MEM for future applications to data analysis</b>	<b>63</b>
4.1	Statistical tools . . . . .	64
4.1.1	The likelihood function . . . . .	64
4.1.2	Parameter estimation and confidence intervals . . . . .	65
4.1.3	Hypothesis test and p-value . . . . .	66
4.1.4	Upper limits and CL <sub>s</sub> method . . . . .	67
4.1.5	The look-elsewhere effect . . . . .	69
4.2	Statistical inference with the MEM: a case-study . . . . .	72
4.2.1	The $c_{Qq}^{11}$ degree of freedom . . . . .	72
4.2.2	The Matrix Element Method . . . . .	73
4.2.3	Configuring the process with MoMEMta . . . . .	75
4.2.4	Results . . . . .	78
4.2.4.1	MLE at generator-level . . . . .	79
4.2.4.2	MLE at reconstruction-level . . . . .	81
4.2.5	Final considerations . . . . .	81
<b>5</b>	<b>Search for two new Higgs bosons through the <math>H \rightarrow ZA \rightarrow \ell^+ \ell^- b\bar{b}</math> process</b>	<b>87</b>
5.1	$H \rightarrow ZA \rightarrow \ell^+ \ell^- b\bar{b}$ : signal and backgrounds . . . . .	88
5.1.1	The signal . . . . .	88
5.1.2	The backgrounds . . . . .	89
5.2	Object reconstruction and event selection . . . . .	97
5.2.1	Object reconstruction at a glance . . . . .	97
5.2.2	Identifying the $\ell\ell jj$ final state . . . . .	98
5.3	Signal region definition . . . . .	102
5.3.1	Parametrization of the signal region . . . . .	104
5.3.1.1	Ellipse parametrization . . . . .	108
5.3.1.2	Ellipse size . . . . .	109
5.3.2	Final templates . . . . .	112
5.4	DY reweighting . . . . .	115
5.5	Systematic uncertainties . . . . .	118
5.6	Results . . . . .	122
5.6.1	Upper limits and interpretation in Type-II 2HDM . . . . .	122
5.6.2	Discussion . . . . .	124
5.7	Estimating the LEE in 2D . . . . .	128

---

5.7.1	Background smoothing: a "customized" KDE . . . . .	129
5.7.2	Quantification of the LEE . . . . .	130
5.8	Comparison with previous searches . . . . .	135
<b>Conclusions</b>		<b>139</b>
<b>References</b>		<b>141</b>



# Introduction

Over the last century, a vast experimental and theoretical effort resulted in the *Standard Model* (SM) of particle physics, a theoretical framework that aims at describing fundamental particles and the interactions between them. Its validity has been remarkably proven by a large programme of experimental researches, culminating in the discovery of the Higgs boson in 2012 at CERN [1,2].

Despite this, the SM leaves some fundamental questions open. To name a few, it does not provide an explanation to the observed matter/antimatter asymmetry in the Universe, and it does not accommodate any viable dark matter candidate encompassing all the properties suggested by astrophysical and cosmological observations. Moreover, it describes only three of the four fundamental forces, leaving gravity out of the picture. To remedy the incompleteness of the SM, many scenarios of physics beyond the SM (BSM) have been postulated, among which are extensions of the SM scalar sector. The two-Higgs-doublet model (2HDM) [3] is one of these, and it predicts the existence of five new physical Higgs bosons.

The search for new physics is carried out world-wide. In Geneva, CERN plays a significant role with its laboratories and cutting-edge machines and detectors, among which the Large Hadron Collider (LHC) and the Compact Muon Solenoid (CMS) are two examples of remarkable engineering and technological endeavors. The first accelerates hadrons and makes them collide at very high energy; the second records the information from the particles produced in the collisions.

In this thesis, a search for two new neutral Higgs bosons  $H$  and  $A$ , predicted in the 2HDM, is presented. The statistical analysis, crucial to assess the presence of new particles, is conducted on the data collected by the CMS experiment in 2016. The chosen decay chain for the search is  $H \rightarrow ZA$  with the  $Z$  boson decaying to a pair of leptons and the  $A$  boson decaying to a pair of  $b$  quarks, and is well motivated by the theoretical model. With the exception of these initial assumptions, the search is conducted keeping as much as possible an approach that does not depend on the specific model and represents an optimization of the same search conducted on the data collected by the CMS experiment during the Run 1 data-taking [4], with the purpose of improving the sensitivity of the analysis. Upper limits on the product of the signal production cross section and branching ratio are extracted. They are then used to recast the results in the context of the 2HDM.

While searches for new particles in a specific final state represent a viable way to look for new physics, the energy scale that they can probe is bounded by the current reach of collider experiments. In this context, indirect searches are a valuable alternative of seeking new physics, and the Standard Model Effective Field Theory (SMEFT) [5] represents a well-established framework for this purpose. A case-study for inferring constraints on the  $c_{Qq}^{11}$  Wilson coefficient of the SMEFT on a simulation sample is conducted. The study is carried out using the Matrix Element Method (MEM) [6], a powerful technique for statistical parameter inference that provides a direct connection between the underlying physics processes and the detector-level physical observables. The MEM weights are computed with MoMEMta [7], a software that I contributed to develop during my PhD, specifically designed to facilitate the applicability of the MEM and speed up its computation.

In this thesis, the SM is briefly presented in Chapter 1 with a focus on the Higgs sector, essential to describe the theory of the 2HDM, which is presented in Chapter 2. Chapter 3 is devoted to the description of the LHC and the CMS experiment, particle reconstruction algorithms, and the simulation of processes. The description of the statistical tools used to perform the statistical data analysis and extract the results is given in Chapter 4. In this chapter, the case-study that applies the MEM to infer constraints on the  $c_{Qq}^{11}$  Wilson coefficient is also described. Finally, Chapter 5 is devoted to the  $H \rightarrow ZA \rightarrow \ell^+ \ell^- \bar{b}b$  search, where the strategy of the analysis is largely described and results are presented.

# 1.

## Chapter

# The scalar sector of the Standard Model

The Standard Model (SM) of particle physics provides a description of the interactions between fundamental particles. Its validity has been well established by a large programme of experimental researches carried out world-wide over the last 50 years. A crucial feature of the SM is its scalar or *Higgs* sector. Its existence has been well established with the discovery of the Higgs boson at CERN in 2012 [1,2].

Despite this, a number of fundamental questions remain unanswered. In this chapter, a brief overview of the SM is presented with a focus on the scalar sector theory and phenomenology. A review of some of the open questions that the SM does not address is also given. This will serve as an introduction for the description of new theoretical models predicting not yet experimentally observed particles, in order to provide a theoretical context for the search of two new particles presented in thesis.

### 1.1. Particles and forces

The SM is a theoretical framework that describes interactions between fundamental particles. It provides a successful explanation of three of the four fundamental interactions, also known as fundamental forces: electromagnetic, weak and strong force. The electromagnetic and the weak force are different manifestations of a single unified force called electroweak (EW), while the strong force is governed by the theory of quantum chromodynamics (QCD). Gravity is not accounted for in the SM.

The fundamental particles entailed by the SM are grouped in two categories: fermions, with half-integer spin, and bosons, with integer spin. The fermions are further split into two families: quarks and leptons.

The quarks carry a fractional electric charge and a color charge and exist in three states: "red", "blue", and "green". In nature, color-charged quarks don't exist individually, but they are bound together in mesons (quark-antiquark objects) or baryons (three-quark objects), which are color-neutral. There exist six flavors of quarks: up (u), down (d), charm (c), strange (s), top (t), and bottom (b).

Unlike quarks, leptons carry an electric charge of one fundamental charge unit in the case of electrons ( $e$ ), muons ( $\mu$ ), and tauons ( $\tau$ ), and no charge in case

of the corresponding neutrinos ( $\nu_{e,\mu,\tau}$ ). Moreover, they don't carry any color charge. Twelve bosons are responsible for mediating the three fundamental forces between the fermions: the photon,  $\gamma$ , mediates the electromagnetic interaction between all fermions but neutrinos; the weak gauge bosons  $W^\pm$  and  $Z$  mediate the electroweak interaction between all fermions; while eight gluons mediate the strong interaction between all quarks.

The SM particles are classified as *left-handed* doublets and *right-handed* singlets. A fermion is right-handed when its spin is parallel to its direction of motion and left-handed when it is opposite. From the point of view of the weak interaction, left- and right-handed fermions are different particles, hence they are classified as in Table 1.1, where left-handed and right-handed is indicated with the subscript  $L$  and  $R$ , respectively. The weak interaction acts only on left-handed particles (and right-handed anti-particles).

**Table 1.1.** | Classification of the SM fermions.

$$\begin{aligned}
 1^{st} \text{ family: } & \begin{pmatrix} \nu_e \\ e^- \end{pmatrix}_L, e_{R}^-, \begin{pmatrix} u \\ d \end{pmatrix}_L, u_R, d_R \\
 2^{nd} \text{ family: } & \begin{pmatrix} \nu_\mu \\ \mu^- \end{pmatrix}_L, \mu_{R}^-, \begin{pmatrix} c \\ s \end{pmatrix}_L, c_R, s_R \\
 3^{rd} \text{ family: } & \begin{pmatrix} \nu_\tau \\ \tau^- \end{pmatrix}_L, \tau_{R}^-, \begin{pmatrix} t \\ b \end{pmatrix}_L, t_R, b_R
 \end{aligned}$$

## 1.2. The SM Lagrangian

The SM is built within the quantum field theory framework and it is a non-abelian gauge theory, invariant under the gauge group

$$G = SU(3)_C \otimes SU(2)_L \otimes U(1)_Y, \quad (1.1.)$$

with  $SU(3)_C$  being the symmetry group of the strong interactions and  $SU(2)_L \otimes U(1)_Y$  the symmetry group of the EW interactions.

The Lagrangian density (for simplicity, we will refer to it as just *Lagrangian* in the following) for a free fermion, represented by a four-component field  $\psi$  with mass  $m$ , or Dirac Lagrangian, reads:

$$\mathcal{L}_{Dirac} = \bar{\psi} i \gamma_\mu \partial^\mu \psi - m \bar{\psi} \psi, \quad (1.2.)$$

where  $\bar{\psi} i \gamma_\mu \partial^\mu \psi$  is the kinetic term relative to the motion of the field  $\psi$ , and  $m \bar{\psi} \psi$  is a *mass term*. The Lagrangian of the SM is built starting from the Dirac Lagrangian with the requirement of a local gauge invariance. This implies the

definition of the *covariant derivative*  $D_\mu = \partial_\mu + igA_\mu^a T_a$ , where  $g$  is the gauge coupling,  $A_\mu$  is the gauge field, and  $T_a$  is the generator of the group. The index  $a$  runs over the number of generators of the group being considered, while the index  $\mu$  takes values 0 for time-like components and 1, 2, 3 for space-like components.

- In QED,  $A$  is the photon field  $\gamma$  and  $T_a$  is equal to the electric charge  $Q$  for the symmetry group  $U(1)_Q$ ; while  $A$  is the gauge field  $B$  and  $T_a$  is equal to the weak hypercharge  $Y$  for the symmetry group  $U(1)_Y$ . The  $U(1)_Q$  group is recovered after electroweak symmetry breaking, as explained in Section 1.2.1. Here,  $a = 1$  (only one generator is present);
- in QCD,  $A$  is the gluon field and  $T_a$  is equal to  $\lambda_a/2$  ( $\lambda_a$  being the Gell-Mann matrices), with  $a = 1..8$ ;
- in the theory of weak interactions,  $A$  is the weak field  $W$  and  $T_a$ , called weak isospin, is equal to  $\sigma_a/2$  ( $\sigma_a$  being the Pauli matrices), with  $a = 1..3$ .

Electromagnetism and weak interactions are unified in a theory called *electroweak theory*, with  $SU(2)_L \otimes U(1)_Y$  as its symmetry group. The EW theory has therefore four generators (the hypercharge and the three components of the weak isospin) and four fields associated to it ( $B, W^1, W^2, W^3$ ). Because of this theoretical "mix", the physical gauge bosons  $\gamma, W^\pm$ , and  $Z$  do not have a one-to-one correspondence with the four EW fields, but they are rather a linear combination of them.

It is crucial to underline here that, in order to preserve the gauge invariance, the gauge fields must be massless. While this is the case for the carriers of the electromagnetic (photon) and strong (gluons) interactions, the carriers of weak interactions,  $W^\pm$  and  $Z$ , are found to be massive from experiments at colliders [8,9]. Moreover, the presence of massive fermions breaks the gauge symmetry in the EW sector.

Within the SM, this problem is mathematically solved with the Brout-Englert-Higgs (BEH) mechanism [10–12] via the process of *electroweak symmetry breaking* (EWSB). The SM Lagrangian can therefore be formulated as follows:

$$\mathcal{L}_{SM} = \mathcal{L}_{QCD} + \mathcal{L}_{EW} + \mathcal{L}_{EWSB} , \quad (1.3.)$$

with  $\mathcal{L}_{QCD}$  containing a quark kinetic term resulting in quark-gluon coupling, together with terms describing the self-interaction<sup>1</sup> between three and four gluons (additional quark mass terms can be added to the Lagrangian in pure QCD. In the context of the SM, they are instead generated during EWSB, as described in section 1.2.1);  $\mathcal{L}_{EW}$  containing a kinetic term for the SM fermions and a term describing the gauge boson kinetic energy and self-interactions;

<sup>1</sup> All the self-interaction terms in the SM Lagrangian derive from the non-abelian nature of the  $SU(3)_C$  and  $SU(2)_L$  symmetry groups.

$\mathcal{L}_{EWSB}$  will be described in the next section.

### 1.2.1. The Brout-Englert-Higgs mechanism: breaking the symmetry

As mentioned above, the problem of the masses is solved within the SM by the spontaneous symmetry breaking of the electroweak symmetry from  $SU(2)_L \otimes U(1)_Y$  to  $U(1)_Q$ , via the BEH mechanism. The generator of  $U(1)_Q$  is given by  $Q = Y/2 + T_3$ , where  $T_3$  is third component of the weak isospin.

In order to generate masses for the  $W^\pm$  and  $Z$  bosons while keeping the photon massless, a new complex scalar  $SU(2)$  doublet  $\Phi$  is introduced *ad hoc* such that:

$$\Phi = \begin{pmatrix} \phi^+ \\ \phi^0 \end{pmatrix} = \begin{pmatrix} \phi_1 + i\phi_2 \\ \phi_3 + i\phi_4 \end{pmatrix}, \quad (1.4.)$$

together with a potential  $V(\Phi)$  of the form:

$$V(\Phi) = \mu^2 \Phi^\dagger \Phi + \lambda (\Phi^\dagger \Phi)^2, \quad \lambda > 0. \quad (1.5.)$$

The vacuum expectation value (vev) of the scalar doublet  $\Phi$  is given by its lowest energy state  $\langle \Phi \rangle_0$ , which minimizes the potential defined in Eq. 1.5. Depending on the sign of  $\mu^2$ , two scenarios are possible.

In scenario I (depicted in Fig. 1.1a), where  $\mu^2 > 0$ , there exists a unique minimum at  $\langle \Phi \rangle_0 = 0$  and  $V(\langle \Phi \rangle_0) = 0$ . Conversely, in scenario II (depicted in Fig. 1.1b), where  $\mu^2 < 0$ ,  $\langle \Phi \rangle_0 = 0$  is a local maximum and there exist infinite degenerate minima all having the same  $|\Phi|$  but different complex phases. This is represented by the red dotted line. Here,

$$\langle \Phi \rangle_0 = \sqrt{\frac{-\mu^2}{2\lambda}} \equiv \frac{v}{\sqrt{2}} \neq 0. \quad (1.6.)$$

The choice of a particular value for the vacuum (or complex phase) spontaneously breaks the rotational symmetry. It is always possible to choose a suitable axis rotation such that the real component of the singlet  $\phi^0$  ( $\phi_3$ ) acquires a non-zero vacuum expectation value  $v$ , while the remaining  $\phi_1$ ,  $\phi_2$ , and  $\phi_4$  acquire a null vacuum expectation value. In the SM,  $v \approx 246$  GeV. Then, the lowest energy state of the potential in Eq. 1.5 reads:

$$\langle \Phi \rangle_0 = \frac{1}{\sqrt{2}} \begin{pmatrix} 0 \\ v \end{pmatrix}, \quad v = \sqrt{\frac{-\mu^2}{\lambda}}. \quad (1.7.)$$

When a symmetry is spontaneously broken, massless particles arise called *Goldstone bosons*, and are as many as the number of generators of the broken symmetry ( $SU(2)_L$  in this case). In the BEH mechanism, the Goldstone bosons are associated to perturbations of the lowest energy state along the rotational

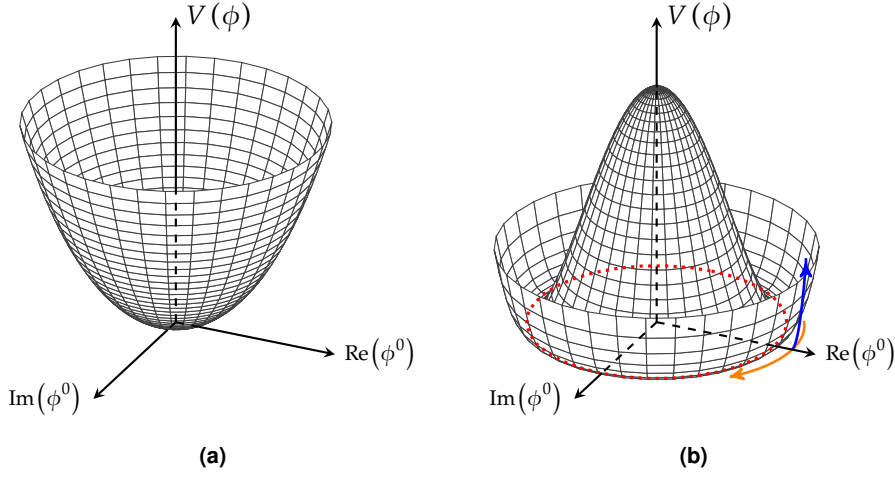


**Figure 1.1.** | Higgs potential, visualized as a function of the complex field  $\phi^0$ , in the case  $\mu^2 > 0$  (a) and  $\mu^2 < 0$  (b).

component (orange arrow in Fig. 1.1b): since the energy in the adjacent states is the same, perturbations in this direction do not face any resistance and the bosons are therefore massless.

Conversely, a perturbation along the longitudinal direction, marked in Fig. 1.1b with a blue arrow, does cost some energy since the adjacent states do not have the same energy anymore: the field associated to such perturbation is the *Higgs boson*. In unitary gauge, the Goldstone bosons are absorbed and the expansion around the minimum is given by:

$$\Phi \rightarrow \frac{1}{\sqrt{2}} \begin{pmatrix} 0 \\ v+H \end{pmatrix}, \quad (1.8.)$$

where H is the above-introduced Higgs boson.

After EWSB, the  $\mathcal{L}_{EWSB}$  in 1.3 reads:

$$\mathcal{L}_{EWSB} = \mathcal{L}_{SBS} + \mathcal{L}_{YW}, \quad (1.9.)$$

where  $\mathcal{L}_{SBS}$  and  $\mathcal{L}_{YW}$  are the symmetry breaking sector Lagrangian and the Yukawa Lagrangian, respectively.

By imposing the gauge invariance through the electroweak covariant derivative on  $\mathcal{L}_{SBS} = (D_\mu \Phi)(D^\mu \Phi)^\dagger - V(\Phi)$ , one finds a mass term for the gauge bosons  $W^\pm$  and Z, a term describing the interaction between the Higgs boson and the  $W^\pm$  (Z) that depends quadratically on the mass of the  $W^\pm$  (Z), and a Higgs boson self-interaction term.

So far, all terms in the SM Lagrangian have been derived under the assumption of massless fermions, since the presence of a mass term would break the gauge

symmetry. This is once again solved by the presence of the Higgs doublet: this introduces a Yukawa term containing mass terms for the fermions and terms describing the interaction between the Higgs boson and the fermions (the latter depending linearly on the mass of the fermions) [13, 14].

The Higgs boson was discovered by the ATLAS [15] and CMS [16] experiments at CERN in 2012 [1, 2], thus validating the hypothesis of the BEH mechanism. Its mass has been measured to be  $125.09 \pm 0.21(\text{stat}) \pm 0.11(\text{syst})$  GeV [17–19].

### 1.3. Higgs physics at the LHC

The Higgs boson plays a crucial role in the modern experimental and theoretical physics scenario. It is considered a portal to new physics, since precise measurements of its properties might shed light on new BSM scenarios.

The production of the Higgs boson at the Large Hadron Collider (LHC) via proton-proton collisions can occur in four different ways, listed below. For each of these production modes, the cross section can be theoretically calculated. The values reported below correspond to a Higgs boson with a mass of 125 GeV and center-of-mass energy of 14 TeV at NNLO+NNLL corrections in QCD and NLO corrections in QED [20]:

- **gluon-gluon fusion** (ggH): the production of a Higgs boson proceeds through triangular heavy-quark loops [21], and in particular the top quark, with small corrections coming from the bottom quark loop. It is the most dominant production channel at the LHC, with a calculated production cross section  $\sigma_{ggF} = 49.47^{+14.7}_{-14.0}$  pb. It is sketched in Fig. 1.2a;
- **vector boson fusion** (VBF): when two (anti-)fermions collide, they can exchange two virtual vector bosons, that interact producing a Higgs boson. This is the second most dominant production mode at the LHC, with a calculated production cross section  $\sigma_{VBF} = 4.23^{+3.7}_{-3.8}$  pb. It is sketched in Fig. 1.2b;
- **Higgs-strahlung**: the Higgs boson is radiated by a vector boson in the process  $q\bar{q} \rightarrow H V$  with  $V = W^\pm, Z$ ; its production cross section is calculated to be  $\sigma_{HS} = 1.52^{+3.0}_{-3.8}$  ( $0.97^{+6.2}_{-6.1}$ ) pb for a Higgs radiated by a W (Z) boson. It is sketched in Fig. 1.2c;
- **associated production with top quark pairs** (ttH): two colliding gluons can split into a heavy quark-antiquark pair each. A quark and antiquark from each pair can then combine to form a Higgs boson. This is the rarest production mode at the LHC, with a calculated production cross section  $\sigma_{ttH} = 0.61^{+14.8}_{-18.2}$  pb. It is sketched in Fig. 1.2d.

A pie chart of the production modes of a Higgs boson with a mass of 125 GeV at the LHC is shown in Fig. 1.3.

The Higgs boson can decay to different channels, yielding a variety of final

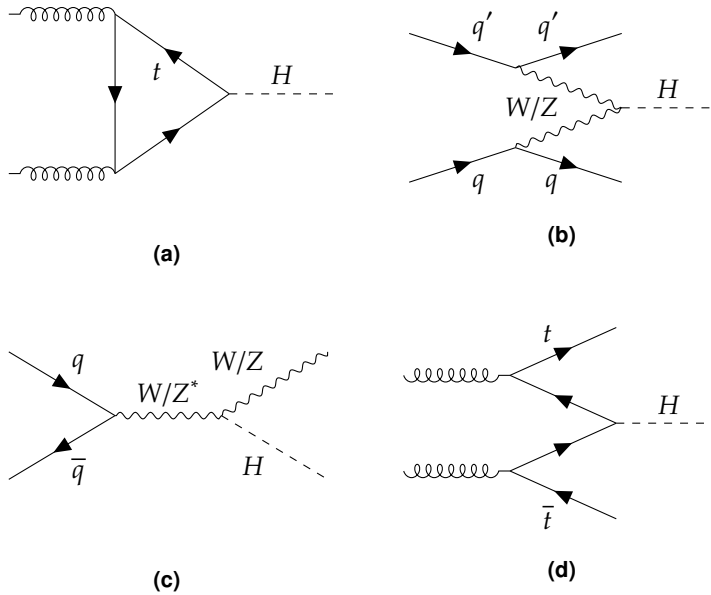


**Figure 1.2.** | Production modes for the Higgs boson at the LHC: gluon-gluon fusion (a), vector boson fusion (b), Higgs-strahlung (c), and associated production with top quark pairs (d).

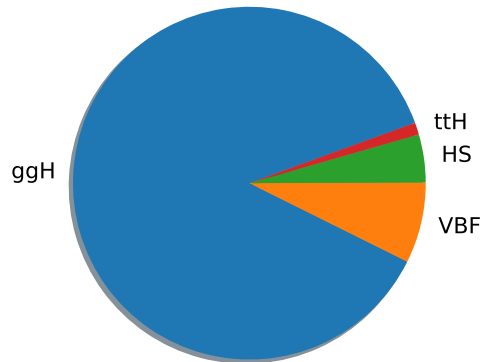


**Figure 1.3.** | Production modes of a Higgs boson with a mass of 125 GeV at the LHC. The production through gluon-gluon fusion (ggH), vector boson fusion (VBF), Higgs-strahlung (HS), and associated production with top quark pairs (ttH) amounts to ~87%, ~7.4%, ~4.4, and ~1% of the total Higgs boson production, respectively.

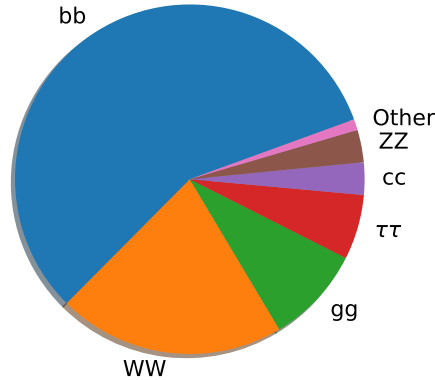


**Figure 1.4.** | Branching ratios for a Higgs boson with a mass of 125 GeV. The highest branching ratio is for decays to  $b\bar{b}$ , which amounts to  $\sim 57\%$ . This is followed by the decay to a pair of W bosons ( $\sim 21\%$ ), gluons ( $\sim 9\%$ ),  $\tau$  leptons ( $\sim 6\%$ ), charm quarks ( $\sim 3\%$ ), and Z bosons ( $\sim 3\%$ ). Decays to other particles are labeled with *Other* and their branching ratio amounts to  $\sim 1\%$ .

states that can be investigated at the LHC, driven by the SM couplings once kinematically allowed. For a Higgs boson mass close to 125 GeV, the main fermionic decay mode is a pair of bottom quarks with a branching ratio of 0.575, followed by a pair of tau leptons with 0.062 [22]. The bosonic decays a pair of W (Z) bosons occur with a branching ratio of 0.22 (0.027), while the branching ratio for a pair of photons is 0.0023. Figure 1.4 shows a pie chart of the Higgs boson decay modes for a Higgs boson with a mass of 125 GeV.

## 1.4. The Standard Model open questions

The validity of the SM has been successfully established by a variety of experimental searches. So far, all measurement are found to be consistent with the predictions from the SM, within uncertainties. Despite this, a number of fundamental questions and problems remain unsolved. In this section, we will give an overview of the main problems that the SM does not address.

### The hierarchy problem

The measured Higgs boson mass can be seen as a combination of two contributions: the bare mass ( $M_{bare}$ ) and the loop corrections ( $\delta M$ ) [23]:

$$M_{measured}^2 = M_{bare}^2 + \delta M^2. \quad (1.10.)$$

The loop corrections to the Higgs boson mass derive from self-interaction, gauge, and fermion (especially top because of its high mass) loops. These corrections are quadratically divergent with  $\Lambda^2$ , where  $\Lambda$  is a cut-off scale. This implies that at very high values of  $\Lambda$ , for instance of the order of the Planck mass  $M_p \approx 10^{19}$  GeV (which is the scale at which the gravitational force is expected to play a significant role), the quantum corrections to the Higgs boson mass become very large. This would boost the Higgs boson mass to values of the order of the Planck mass. However, experimentally we know that this is not the case. This is the so-called *hierarchy problem*. Therefore, the only way to make sense of the  $10^{19}$  GeV mass contribution from the loop corrections is if the tree-level diagram gives the bare mass a (negative) value which precisely cancels out the large number, in order to leave only a  $\sim 125$  GeV mass.

It is important to remark that, despite that this *fine-tuning* phenomenon does not pose any problem to the theory from a mathematical point of view, it should not occur according to the naturalness paradigm [24].

Beyond the Standard Model (BSM) physics is therefore needed to resolve the fine-tuning and therefore the hierarchy problem.

### Dark matter

Nowadays, hints of existence of *dark matter* are striking [25,26] and pose severe doubts on the completeness of the SM, that does not entail its presence within its theoretical framework. Dark matter particles would be electrically neutral, colorless, and very long-lived or stable. Evidence of dark matter results from many considerations pointed out by scientists over the past century [27,28]. Among the others, the rotational curves of the galaxies and the gravitational lensing, which can be properly explained only if the presence of dark matter is taken into account.

### Neutrino masses

Neutrinos are treated as massless particles in the SM. However, experimental observations have pointed out that neutrinos can oscillate between different flavors as they travel long distances [29,30]. Such behavior implies that the neutrinos have a non-zero mass. The absolute scale of neutrino masses and the mechanism by which they are generated in the SM remains still far from understood.

### Baryon asymmetry

The Big Bang should have created equal amounts of matter and antimatter in the early Universe. However, in the Universe as we know it today, only matter is observed rather than an equal amount of matter and antimatter.

The mechanism of CP violation [13] plays a significant role in this context.

The concept of CP-symmetry states that the laws of physics should be the same if a particle is interchanged with its antiparticle (charge conjugation or C-symmetry) while its spatial coordinates are inverted (parity or P-symmetry). One of the conditions to explain the matter-antimatter asymmetry is that a significant source of CP violation is necessary to produce matter and antimatter at a different rate [31]. However, the sources of CP violation in the SM are too small to explain the visible Universe today. Such sources could arise from extensions of the SM, in particular in the scalar sector.

### **Vacuum stability**

When accounting for loop corrections to the Higgs potential described in Section 1.2.1, the Higgs self-coupling can be driven to negative values at high values of the Yukawa coupling between the top quark and the Higgs boson and high energies. The form depicted in Fig. 1.1b is therefore altered in a new potential, with only one minimum or two minima that are not degenerate in energy anymore.

In the case where the electroweak vacuum lies in a global minimum of the potential, the vacuum is said to be *stable*, and the future of the Universe is not threatened. On the other hand, if the electroweak vacuum lies in a local minimum, quantum tunneling could make the vacuum decay towards the lowest minimum. In this case, the vacuum is said to be *meta-stable* [32]. Technically, the transition could occur through quantum processes at any time, but it probably will not due to the predicted much longer lifetime of a metastable universe with respect to the current age of the Universe.

Current experimental measurements place the electroweak vacuum in the meta-stability region, but on the critical border with the stability region [32]. If no new physics at the TeV scale is discovered, precise measurements of the Higgs and top quark masses are key to unveil the underlying principles of nature.

# 2.

## Chapter

# Extending the Standard Model

The Higgs sector in the Standard Model is built on the simplest possible scalar structure, i.e. one  $SU(2)$  doublet. However, as outlined in Section 1.4, the presence of new physics is needed to address problems that the SM is not able to explain. New BSM theoretical frameworks can be obtained by extending the SM scalar sector with singlets, doublets, or triplets. The two-Higgs-doublet model (2HDM) builds on the presence of a second  $SU(2)$  doublet in the Higgs sector.

Theoretical motivations justify well the presence of the 2HDM among the most credited BSM scenarios. The 2HDM is a proposed solution for the strong CP problem [33]<sup>1</sup>, for the observed baryon asymmetry, due to the flexibility of its scalar mass spectrum [35] and fits well the supersymmetry [36] theoretical framework. In this chapter, a theoretical description of the 2HDM is given. Then, the 2HDM phenomenology is described together with the current experimental status. In cases where the additional Higgs bosons are far beyond the reach of direct observations, the Standard Model Effective Field theory can be used to probe new physics through its low-energy manifestations. A brief theoretical overview of this framework is also presented in this chapter.

### 2.1. A theoretical overview

Two complex  $SU(2)$  scalars with identical quantum numbers containing eight fields are defined as follows:

$$\Phi_a = \begin{pmatrix} \phi_a^+ \\ (v_a + \rho_a + i\eta_a)/\sqrt{2} \end{pmatrix}, \quad a = 1, 2. \quad (2.1.)$$

The most general 2HDM potential contains fourteen parameters, making its parameter space and phenomenology very complicated. An approach to tackle this issue is to impose by hand global symmetries in order to lower the number of free parameters.

The complex parameters in the most general potential are responsible for the breaking of the CP symmetry. The potential can then be rephased so that all

---

<sup>1</sup> The QCD Lagrangian contains terms that are able to violate the CP-symmetry. However, no violation has been observed so far. The presence of a new doublet is a possible way to solve the problem in axion models [34].

parameters become real, and therefore CP conservation is enforced. A further restriction on the 2HDM potential is to eliminate tree-level flavor-changing neutral currents (FCNCs). This can be achieved by imposing a  $Z_2$  discrete symmetry on the doublets:  $\Phi_1 \rightarrow \Phi_1$ ,  $\Phi_2 \rightarrow -\Phi_2$  [37]. However, one can choose  $Z_2$  not to be an exact symmetry of the potential but to softly break it. Under these assumptions, the most general scalar potential for the two doublets  $\Phi_1$  and  $\Phi_2$  reads:

$$V(\Phi_1, \Phi_2) = m_{11}^2 \Phi_1^\dagger \Phi_1 + m_{22}^2 \Phi_2^\dagger \Phi_2 - m_{12}^2 (\Phi_1^\dagger \Phi_2 + \Phi_2^\dagger \Phi_1) + \frac{\lambda_1}{2} (\Phi_1^\dagger \Phi_1)^2 + \frac{\lambda_2}{2} (\Phi_2^\dagger \Phi_2)^2 + \lambda_3 \Phi_1^\dagger \Phi_1 \Phi_2^\dagger \Phi_2 + \lambda_4 \Phi_1^\dagger \Phi_2 \Phi_2^\dagger \Phi_1 + \frac{\lambda_5}{2} [(\Phi_1^\dagger \Phi_2)^2 + (\Phi_2^\dagger \Phi_1)^2] \quad (2.2.)$$

where all the parameters are real.

A measure of how much the discrete symmetry is broken is contained in the term with  $m_{12}^2$ , which is therefore called *soft-breaking term*. If  $m_{12} = 0$ , the potential has an exact  $Z_2$  symmetry [38]. It can be seen from Eq. 2.2 that the number of free parameters has been reduced from fourteen to eight:  $m_{1,2}^2$ ,  $m_{12}^2$ , and  $\lambda_{1,5}$ .

The minimization of this potential gives:

$$\langle \Phi_1 \rangle_0 = \frac{1}{\sqrt{2}} \begin{pmatrix} 0 \\ v_1 \end{pmatrix}, \quad \langle \Phi_2 \rangle_0 = \frac{1}{\sqrt{2}} \begin{pmatrix} 0 \\ v_2 \end{pmatrix}, \quad (2.3.)$$

analogously to Eq. 1.7.

Due to the breaking of the  $SU(2)$  symmetry, three Goldstone bosons appear and can be absorbed similarly to the EWSB in the case of one doublet. In this way, the  $W^\pm$  and  $Z$  bosons acquire mass and five new scalar ("Higgs") physical fields are left: two charged bosons, two neutral CP-even bosons (scalars), and one CP-odd boson (pseudoscalar). In particular, the definition of the fields occurs as follows.

With the minima defined in Eq. 2.3, the mass terms for the charged scalars are given by:

$$\mathcal{L}_{\phi^\pm mass} = [m_{12}^2 - (\lambda_4 + \lambda_5)v_1 v_2] (\phi_1^-, \phi_2^-) \begin{pmatrix} v_2 & -1 \\ v_1 & v_1 \\ -1 & v_2 \end{pmatrix} \begin{pmatrix} \phi_1^+ \\ \phi_2^+ \end{pmatrix}, \quad (2.4.)$$

where  $v_1$  and  $v_2$  are the vevs of the two doublets and, assuming no CP violation, they are taken to be both real and non-negative. The matrix corresponding to  $\phi^{+(-)}$  has two eigenvalues: a null one, corresponding to a Goldstone boson (then absorbed to give mass to the  $W^{+(-)}$ ) and a non-zero one that defines the squared mass of the charged Higgs:  $m_{+(-)}^2 = [m_{12}^2 / (v_1 v_2) - \lambda_4 - \lambda_5](v_1^2 + v_2^2)$ .

The mass terms for the pseudoscalars are given by:

$$\mathcal{L}_{\eta mass} = [m_{12}^2/(v_1 v_2) - 2\lambda_5] \begin{pmatrix} \eta_1 \\ \eta_2 \end{pmatrix} \begin{pmatrix} v_2^2 & -v_1 v_2 \\ -v_1 v_2 & v_1^2 \end{pmatrix} \begin{pmatrix} \eta_1 \\ \eta_2 \end{pmatrix}. \quad (2.5.)$$

Again, this matrix yields two eigenvalues: a null one, corresponding to the Goldstone boson (then absorbed to give mass to the Z) and a non-zero one that defines the squared mass of the physical pseudoscalar:  $m_A^2 = [m_{12}^2/(v_1 v_2) - 2\lambda_5](v_1^2 + v_2^2)$ . Finally, the mass terms for the neutral scalars are given by:

$$\mathcal{L}_{\rho mass} = - \begin{pmatrix} \rho_1 \\ \rho_2 \end{pmatrix} \begin{pmatrix} m_{12}^2 \frac{v_2}{v_1} + \lambda_1 v_1^2 & -m_{12}^2 + \lambda_{345} v_1 v_2 \\ -m_{12}^2 + \lambda_{345} v_1 v_2 & m_{12}^2 \frac{v_1}{v_2} + \lambda_2 v_2^2 \end{pmatrix} \begin{pmatrix} \rho_1 \\ \rho_2 \end{pmatrix}, \quad (2.6.)$$

with  $\lambda_{345} = \lambda_3 + \lambda_4 + \lambda_5$ . Here, two important parameters can be introduced:  $\alpha$ , that is the rotation angle that performs the diagonalization of the mass-squared matrix of the scalars; and  $\beta$ , that is the rotation angle that performs the diagonalization of the mass-squared matrices of the charged scalars and of the pseudoscalars. Also, one can write:  $v_1 = v \cos \beta$ ,  $v_2 = v \sin \beta$ . Therefore, the angle  $\beta$  is such that:

$$\tan \beta \equiv \frac{v_2}{v_1}. \quad (2.7.)$$

The two parameters  $\alpha$  and  $\beta$  are of crucial importance for the 2HDM phenomenology, since they define the interactions of the various Higgs fields with the vector bosons and the fermions.

The physical pseudoscalar A is given by a linear combination of the pseudoscalar fields  $\eta_1$  and  $\eta_2$  orthogonal to the above-mentioned Goldstone boson:

$$A = \eta_1 \sin \beta - \eta_2 \cos \beta. \quad (2.8.)$$

The physical neutral scalars, h and H, are orthogonal combinations of the scalar fields  $\rho_1$  and  $\rho_2$ :

$$\begin{aligned} h &= \rho_1 \sin \alpha - \rho_2 \cos \alpha, \\ H &= -\rho_1 \cos \alpha - \rho_2 \sin \alpha. \end{aligned} \quad (2.9.)$$

The SM Higgs boson would be:

$$\begin{aligned} h^{SM} &= \rho_1 \cos \beta + \rho_2 \sin \beta \\ &= h \sin(\alpha - \beta) - H \cos(\alpha - \beta). \end{aligned} \quad (2.10.)$$

Without loss of generality, it can be assumed that  $\beta$  is in the first quadrant [39] (as to keep  $v_1$  and  $v_2$  non-negative reals). In the general 2HDM phenomenology,  $\alpha$  is taken to be in the first and fourth quadrant [3].

## The 2HDM free parameters

The potential in Eq. 2.2 has ten free parameters, if one includes the vevs of the two doublets. However,  $v_1$  and  $v_2$  can be related to the electroweak Higgs vev:  $v = \sqrt{v_1^2 + v_2^2} \approx 246$  GeV. This relation reduces the number of degrees of freedom from ten to nine. Moreover,  $m_{11}^2$  and  $m_{22}^2$  can be fixed by minimization conditions. The number of free parameters is thus reduced to seven:  $\lambda_{1..5}$ ,  $m_{12}^2$ , and  $\tan\beta$ . Equivalently, one can choose a physical basis where with the set:  $m_h$ ,  $m_H$ ,  $m_A$ ,  $m_{H^\pm}$ ,  $\tan\beta$ ,  $\alpha$ , and  $m_{12}^2$  representing the seven independent parameters [38]. If one chooses the  $h \equiv h^{SM}$ , then its mass is fixed to 125 GeV and the number of free parameters is further reduced to six.

## 2.2. Phenomenology of the 2HDM

According to the different couplings of all fermions with the Higgs doublets in the 2HDM, four different scenarios or *types* can be defined:

- **Type I:** all quarks and charged leptons couple to only one of the Higgs doublets (conventionally chosen to be  $\Phi_2$ ) while they don't couple at all with the other doublet;
- **Type II:** the up-type quarks couple to one Higgs doublet (conventionally  $\Phi_2$ ) while the down-type quarks and charged leptons couple to the other one ( $\Phi_1$ );
- **Type III (or *lepton specific*):** all quarks couple to the same Higgs doublet (conventionally  $\Phi_2$ ) while the charged leptons couple to the other one ( $\Phi_1$ );
- **Type IV (or *flipped*):** the up-type quarks and charged leptons couple to one Higgs doublet (conventionally  $\Phi_2$ ) while the down-type quarks couple to the other one ( $\Phi_1$ ).

These are summarized in Table 2.1. For all these four types, the Glashow-Weinberg condition [40] holds true due to the above-mentioned  $Z_2$  symmetry and, as a consequence, FCNCs at tree level do not occur.

The specific parameter configuration where  $\cos(\beta - \alpha) = 0$  is called the *alignment limit*. From Eq. 2.10 it can be seen that in such a case, the neutral scalar  $h$  coincides with the  $h^{SM}$ .

In all models, the couplings of the 2HDM neutral scalars to the vector bosons  $W^\pm$  and  $Z$  (referred to as  $V$  for simplicity) are the SM couplings rescaled by the 2HDM parameters  $\sin(\beta - \alpha)$  and  $\cos(\beta - \alpha)$ :

$$g_{hVV} = \frac{m_V^2}{v} \sin(\beta - \alpha), \quad g_{HVV} = \frac{m_V^2}{v} \cos(\beta - \alpha). \quad (2.11.)$$

It is straightforward to see that in the alignment limit the scalar  $H$  does not

**Table 2.1.** | Models which lead to natural flavor conservation.

Model	up-type quarks	down-type quarks	charged leptons
Type I	$\Phi_2$	$\Phi_2$	$\Phi_2$
Type II	$\Phi_2$	$\Phi_1$	$\Phi_1$
Type III	$\Phi_2$	$\Phi_2$	$\Phi_1$
Type IV	$\Phi_2$	$\Phi_1$	$\Phi_2$

couple to vector bosons and that the SM coupling for the scalar  $h$  is recovered. The coupling of the pseudoscalar  $A$  to vector bosons vanishes and is only possible at loop level, assuming that CP is conserved [3], while the coupling between the  $Z$  and the neutral scalars is parametrized as follows:

$$g_{ZA h} \sim \cos(\beta - \alpha), \quad g_{ZA H} \sim \sin(\beta - \alpha). \quad (2.12.)$$

The Yukawa couplings can be determined from the 2HDM Yukawa Lagrangian. Unlike the couplings to vector bosons, they depend on the model being considered; like the couplings to vector bosons, they modify the SM Higgs couplings through a modification factor that depends on  $\alpha$  and  $\beta$ . A summary of the modification factors is reported in Table 2.2. We indicate with  $\xi_X^Y$  the modification factor of the Yukawa couplings between  $X = h, H, A$  and  $Y = u$  (up-type quarks),  $d$  (down-type quarks), and  $\ell$  (charged leptons).

**Table 2.2.** | Yukawa couplings of up-type ( $u$ ), down-type ( $d$ ) quarks and charged leptons  $\ell$  to the neutral scalars  $h$ ,  $H$ , and the pseudoscalar  $A$  in the four different models [3].

Coupling	Type I	Type II	Type III	Type IV
$\xi_h^u$	$\cos\alpha/\sin\beta$	$\cos\alpha/\sin\beta$	$\cos\alpha/\sin\beta$	$\cos\alpha/\sin\beta$
$\xi_h^d$	$\cos\alpha/\sin\beta$	$-\sin\alpha/\cos\beta$	$\cos\alpha/\sin\beta$	$-\sin\alpha/\cos\beta$
$\xi_h^\ell$	$\cos\alpha/\sin\beta$	$-\sin\alpha/\cos\beta$	$-\sin\alpha/\cos\beta$	$\cos\alpha/\sin\beta$
$\xi_H^u$	$\sin\alpha/\sin\beta$	$\sin\alpha/\sin\beta$	$\sin\alpha/\sin\beta$	$\sin\alpha/\sin\beta$
$\xi_H^d$	$\sin\alpha/\sin\beta$	$\cos\alpha/\cos\beta$	$\sin\alpha/\sin\beta$	$\cos\alpha/\cos\beta$
$\xi_H^\ell$	$\sin\alpha/\sin\beta$	$\cos\alpha/\cos\beta$	$\cos\alpha/\cos\beta$	$\sin\alpha/\sin\beta$
$\xi_A^u$	$\cot\beta$	$\cot\beta$	$\cot\beta$	$\cot\beta$
$\xi_A^d$	$-\cot\beta$	$\tan\beta$	$-\cot\beta$	$\tan\beta$
$\xi_A^\ell$	$-\cot\beta$	$\tan\beta$	$\tan\beta$	$-\cot\beta$

The subject of this thesis is the experimental search for the bosons H and A. Their branching ratios (BRs) can be parametrized as a function of the 2HDM parameters  $\tan\beta$  and  $\cos(\beta - \alpha)$ . Figure 2.1 shows this parametrization for the Type-II 2HDM. It can be noticed that the  $\text{BR}(H \rightarrow ZA)$  is maximal for values of  $\cos(\beta - \alpha)$  close to zero and over a wide range of the  $\tan\beta$  parameter space. The  $\text{BR}(A \rightarrow b\bar{b})$  dominates over the other decays for all values of  $\cos(\beta - \alpha)$  and for values of  $\tan\beta$  roughly above 1.

### 2.2.1. The 2HDM mass spectrum

Critical evidence about the scalar structure is represented by the parameter  $\rho$ . In the  $SU(2) \otimes U(1)$  gauge theory, for  $n$  scalar multiplets  $\phi_i$  with weak isospin  $T_i$ , weak hypercharge  $Y_i$ , and vev of the neutral components  $v_i$ , at tree level [41]:

$$\rho = \frac{\sum_{i=1}^n \left[ T_i(T_i + 1) - \frac{1}{4} Y_i^2 \right] v_i}{\sum_{i=1}^n \frac{1}{2} Y_i^2 v_i}. \quad (2.13.)$$

Experimentally, this parameter has been measured to be very close to 1 [42]. To ensure that  $\rho$  matches this value, a *custodial symmetry* is enforced in the 2HDM. From a phenomenological point of view, this gives rise to two different scenarios:

- the charged scalars and the pseudoscalar are degenerate in mass:  $m_{H^\pm}^2 = m_A^2$ . Since the charged bosons are usually assumed to be rather heavy, this implies a relatively high mass for the A. Assuming the pseudoscalar to be heavier than the scalars H and h, a *conventional* mass scenario is defined;
- the charged scalars and the neutral scalar H are degenerate in mass:  $m_{H^\pm}^2 = m_H^2$ . Assuming the scalar H to be heavier than the pseudoscalar, a *twisted* mass scenario is defined.

This is summarized in Fig. 2.2. For each scenario, two possible cases are allowed: the (pseudo)scalar can be lighter or heavier than the measured Higgs at 125 GeV. It is worth noticing that in the 2HDM, conventionally, the scalar h is defined as the lightest scalar. Below the threshold of 125 GeV, the angle defining the alignment limit condition is rotated by  $\pi/2$ , and therefore the two scalars swap. It follows that for consistency, we should have interchanged the notation between h and H in the conventional scenario in Fig. 2.2. However, since the search discussed in this thesis is conducted for H and A over a wide mass spectrum, for simplicity we refer to the scalar always with the notation H for any probed value of its mass.

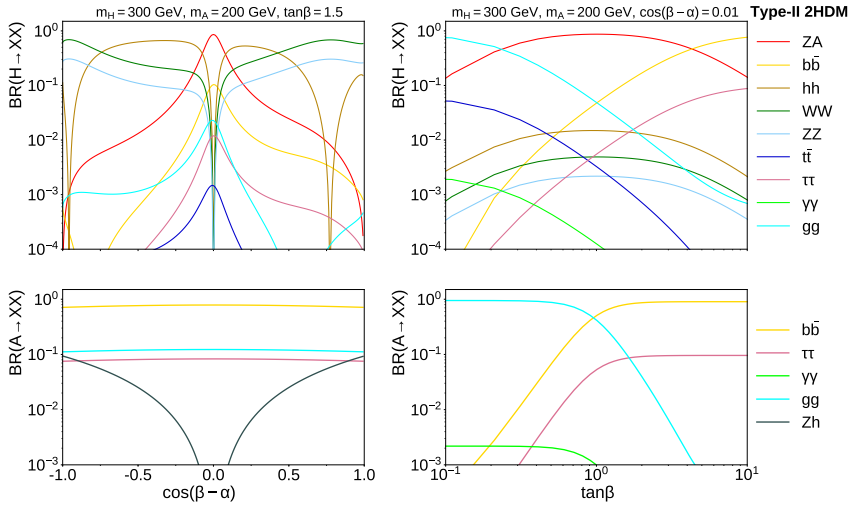


**Figure 2.1.** | Branching ratios of the H (top) and A (bottom) as a function of  $\cos(\beta - \alpha)$  ( $\tan\beta$ ) for the parameters  $m_H = 300$  GeV,  $m_A = 200$  GeV,  $\tan\beta = 1.5$  ( $\cos(\beta - \alpha) = 0.01$ ).

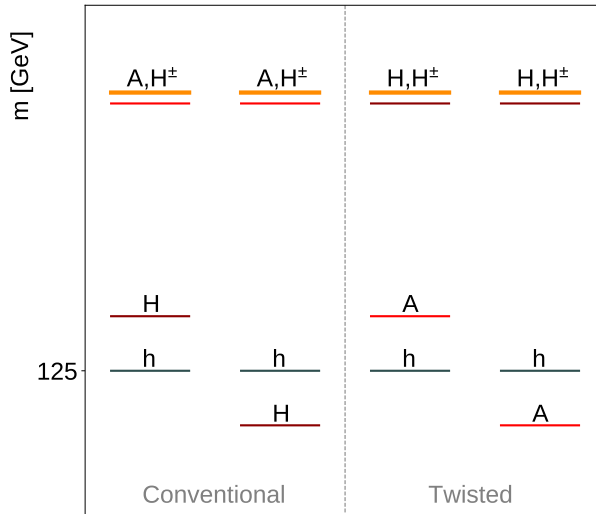


**Figure 2.2.** | Mass hierarchies in the 2HDM.

### 2.3. 2HDM physics at the LHC

Similarly to what happens for the Higgs boson in the SM, the 2HDM bosons can be produced at the LHC through different production modes. The proximity to the alignment limit derived from measurements of the couplings of the SM-like Higgs (see Section 2.4) implies a whole hierarchy of production modes. Since the results shown in this thesis are interpreted in the context of the Type-II 2HDM, we will focus on this particular model.

Inferring the dominant and negligible production modes in the alignment limit is quite straightforward knowing the coupling of the 2HDM bosons to vector bosons (listed in Section 2.2) and fermions (listed in Table 2.2). In Type II, since the  $g_{\text{HVV}}$  coupling is suppressed close to the alignment limit, the vector boson associated production modes of H represent only a tiny fraction of the total production cross section, and it is at most  $\sim 1\%$  of the SM Higgs boson production. Instead, production modes that occur through the strong interaction are still appreciable. In particular, gluon-gluon fusion production of both H and A proceeds through fermion loops, with the top-quark loop contribution proportional to  $\cot^2\beta$  and the bottom loop contribution proportional to  $\tan^2\beta$  at leading order. Indeed, the strength of the couplings of H to fermions approaches that of the A when close to alignment limit condition. The  $\text{ttH/A}$  production mode again scales as  $\cot^2\beta$ , while the  $\text{bbH/A}$  production mode scales as  $\tan^2\beta$ . The production of the charged Higgs is a function of both  $\tan\beta$  and  $\cot\beta$  in the alignment limit [43].

The most important contribution to the total production cross section in Type II is then given by resonant production of heavy neutral Higgses via gluon-gluon fusion and associated production with a pair of b jets. Because of its dependence on  $\tan\beta$ , the latter is sub-dominant at low values of this parameter, becoming the dominant contribution as  $\tan\beta$  increases.

The heavy Higgs bosons can yet decay to a variety of final states. The branching ratios for H and A as a function of  $\cos(\beta - \alpha)$  and  $\tan\beta$  are shown in Fig. 2.1. Several searches are being carried out at the LHC on both gluon-gluon fusion and  $\text{bb}$  associated production of heavy scalars. They include decays to  $\text{bb}$ ,  $\tau^+\tau^-$ ,  $\gamma\gamma$ ,  $\mu^+\mu^-$ , as well as to  $\text{WW}$ ,  $\text{ZZ}$ ,  $\text{Zh}$ ,  $\text{hh}$ . Moreover, processes that include intermediate decays of one heavy Higgs into the other one are considered. In this thesis, the H and A bosons are searched for through the process  $\text{H/A} \rightarrow \text{Z}(\rightarrow \ell^+\ell^-)\text{A/H}(\rightarrow \text{bb})$ , with  $\ell = e, \mu$ . A detailed description of the analysis specifics, the method adopted, the obtained results and the interpretation in the context of Type-II 2HDM is given in Chapter 4.

## 2.4. What we know so far: the 2HDM current experimental status

The main experimental searches for an extended scalar sector can be divided into direct and indirect searches. Direct searches are key for the discovery of new particles that may match the 2HDM properties, thus validating its existence. A huge effort is currently ongoing for the analysis of the data collected during Run 2 at the LHC to search for deviations from the Standard Model that might reveal the presence of new physics. These searches are conducted for all the five 2HDM bosons, in different final states and production modes. Another way to probe the extended scalar sector is to focus on precision measurements of the properties of the 125 GeV Higgs boson. Small deviations from the couplings predicted in the SM could be present, so far possibly not detected because of still poor experimental precision. Detection of such discrepancies would open the door to new physics scenarios, either validating or discrediting the 2HDM.

The main question to address is which part of the 2HDM parameter space is favored and which is rejected by taking into account the experimental constraints from the latest data at the LHC. If  $h$  is assumed to be the 125 GeV Higgs boson, precision measurements of its couplings in different final states and production modes are crucial to shed light on the value of its modification factors  $\xi_h^P$ , with  $P = u, d, \ell, W^\pm, Z$ . So far, all measurements constrain these values to around 1. In other words, no significant deviation from the SM couplings is observed yet [44].

Both the ATLAS [15] and CMS [16] collaborations at CERN have measured the signal strength for the 125 GeV Higgs boson in a variety of final states. Always assuming that this boson corresponds to the 2HDM  $h$ , a Bayesian fit can be performed in order to extract the impact of the signal strength on the 2HDM parameters in the  $\tan\beta$  vs.  $\beta - \alpha$  plane. Indeed, every signal strength depends on the 2HDM  $h$  couplings of all decay products. The results are shown in Fig. 2.3 for the four 2HDM models (Type II, II, III, and IV are indicated with I, II, X, and Y, respectively). All contours delimit the regions allowed with a probability of 95.4%. The gray area is the final combination of the impact of all the analyzed signal strengths. It can be seen that the allowed region is compatible with  $\beta - \alpha = \pi/2$ , which is the value that satisfies the alignment limit. More details can be found at Ref. [45].

Exclusion regions in the parameter space can be as well obtained from direct searches. Both experiments have performed dedicated searches for new signatures in various possible final states at the LHC: fermionic ( $t\bar{t}$ ,  $b\bar{b}$ ,  $\tau^+\tau^-$ ,  $tb$ ,  $\tau^+v$ ), bosonic ( $\gamma\gamma$ ,  $Z\gamma$ ,  $ZZ$ ,  $W^+W^-$ ), and Higgs particles ( $hh$ ,  $hZ$ ,  $HZ$ ,  $AZ$ ). Figure 2.4 shows the available parameter space for 2HDM masses and angles from the fit where the  $H$ ,  $A$ , and  $H^+$  searches (which we refer to as *heavy*

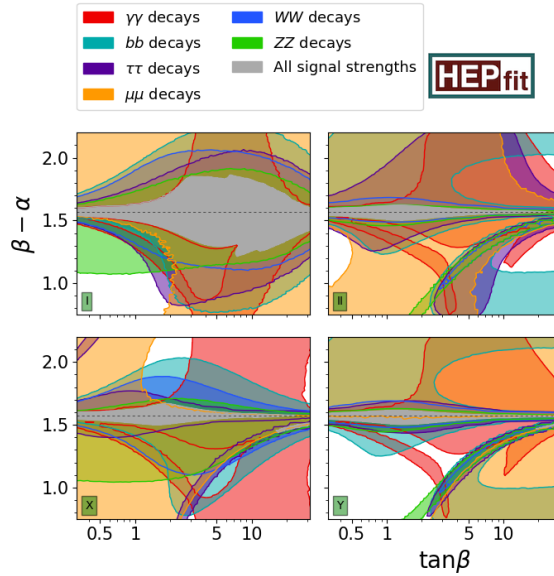


**Figure 2.3.** | Impact of the  $h$  signal strength on the 2HDM parameters in the  $\tan\beta$  vs.  $\beta - \alpha$  plane for the four 2HDM models: Type I (up left), II (up right), III (bottom left), and IV (bottom right). All contours delimit the regions allowed with a probability of 95.4% [45].

*searches* for simplicity) are taken into account. The region inside the various colored patches are disfavored by the corresponding search category denoted in the legend. The central areas inside the solid gray line mark the 95.4% excluded regions when all the Higgs searches are considered in the fit. The combination of all  $H/A/H^+$  searches is represented by the orange/blue/green dashed contours. The first row of this figure conveys the same message as Fig. 2.3: the region around  $\beta - \alpha = \pi/2$  remains unconstrained in all 2HDM types.

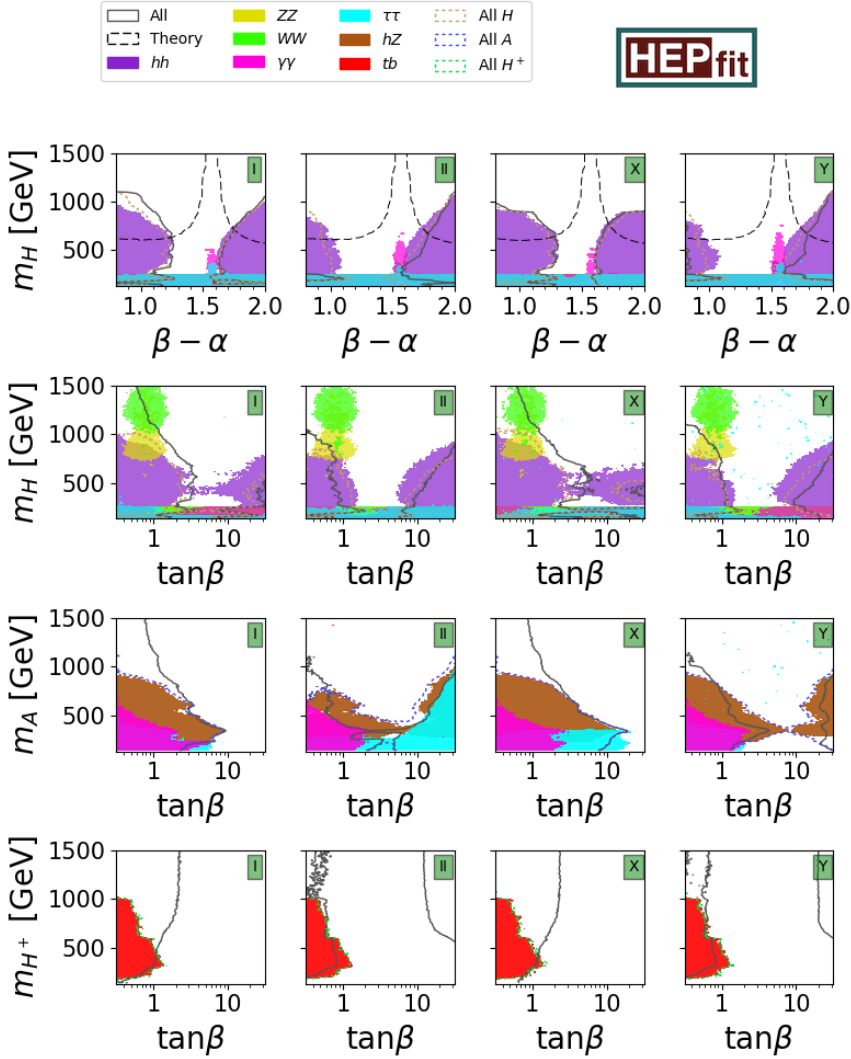


**Figure 2.4.** | Regions in the angles vs. masses planes excluded by all heavy Higgs searches with a probability of 95.4% by the central area inside the solid gray line. Areas excluded by searches in various final states are represented by the colored patches. The areas inside the colored dashed lines correspond to the exclusion at 95.4% when all H searches (orange), all A searches (dark blue) and all  $H^+$  searches (dark green) are considered [45].

## 2.5. The SMEFT: a brief overview

As seen in the previous section, both direct and indirect searches are viable ways to look for new physics. With the former, the energy scale that can be probed is bounded by the current reach of collider experiments. Moreover, direct searches are built from the (even if minimal) assumption of a specific theoretical model, which is not always beneficial. This might induce a bias in the search and "trick" scientists into looking for new physics in a different phase space from the one where it might actually be lying. Indeed, no clear hints about where new physics hides have been provided by experimental results so far.

In this context, indirect and model-independent searches represent a valuable alternative of seeking new physics, and a well-established framework for this purpose is the Standard Model Effective Field Theory (SMEFT) [5]. A complete overview can be found at Refs. [46,47], while a brief description is given below.

An effective field theory (EFT) is a type of approximation for an underlying physical theory. Its purpose is to include the appropriate degrees of freedom to describe physical phenomena occurring at a chosen length scale or energy scale, while ignoring substructure and degrees of freedom at shorter distances (or, equivalently, at higher energies). In short, the main idea behind an EFT is to derive a simplified model at lower energies that describes the behavior of the underlying theory at higher energies.

An EFT constructed from the SM fields and their symmetries is referred to as Standard Model Effective Field Theory, and is used to analyze deviations from the SM. Indeed, the effects of new heavy BSM particles with typical mass scale  $M \approx \Lambda$  can be parametrized at a lower energy  $E \ll \Lambda$  in a model-independent way in terms of a basis of higher-dimensional operators. The effective SM Lagrangian is the result of the following power expansion:

$$\mathcal{L}_{SMEFT} = \mathcal{L}_{SM} + \sum_i^{N_{d_6}} \frac{c_i}{\Lambda^2} \mathcal{O}_i^{(6)} + \sum_i^{N_{d_8}} \frac{b_i}{\Lambda^4} \mathcal{O}_i^{(8)} + \dots \quad (2.14.)$$

where  $\mathcal{L}_{SM}$  is the SM Lagrangian introduced in Chapter 1, and  $\{\mathcal{O}^{(6)}\}$  and  $\{\mathcal{O}^{(8)}\}$  represent the elements of the operator basis of mass-dimension  $d=6$  and  $d=8$ , respectively. The coefficients  $c_i$  are called *Wilson coefficients*. Operators with  $d=5$  and  $d=7$  violate lepton and/or baryon number conservation [48] and thus are not reported.

Searches for extended scalar sectors can be interpreted within this framework only if the masses of the particles being searched for lie at much higher energy scale than the one probed at the LHC. However, a large range of new heavy physics can be accommodated for in the SMEFT, and for this reason this field is nowadays drawing more and more attention.

# 3.

## Chapter

# The CMS experiment, object reconstruction, and simulation

Many experiments installed at the CERN laboratory in Geneva, Switzerland, have the quest for new physics as their primary goal. In this chapter, a short description of CERN together with its accelerator complex is given. We then focus on the Compact Muon Solenoid (CMS) experiment, since the data collected with it in 2016 have been used to carry out the analysis presented in this thesis. A review of the particle reconstruction techniques is then given, together with an overview of how the event simulation is performed for CMS.

### 3.1. Physics at CERN

The Conseil Européen pour la Recherche Nucléaire (CERN) is a research organization that operates the largest particle physics laboratory in the world, situated in a suburb of Geneva on the border between Switzerland and France. The quest for new physics at CERN is mostly carried out with collisions between hadrons (heavy ions and/or protons) at very high energy. The acceleration process is made possible due to a complex of accelerators, with the LHC as the final stage. Two beams of protons are accelerated up to an energy of 6.5 TeV each in opposite directions and collided onto each other, with a center-of-mass energy  $\sqrt{s} = 13$  TeV. Heavy-ion beams are instead accelerated up to an energy of 2.3 TeV per nucleon.

Collisions take place in four distinct places along the LHC, where detectors are located in order to record the information produced by the particles created in the collision, used for subsequent data analysis:

- the ATLAS [15] and CMS [16] detectors are general-purpose detectors and they are similar in design and goals. The range of physics studies targeted by both collaborations is wide and covers precision tests of the SM (electroweak measurements, QCD, top, Higgs, b-physics, etc.) and direct searches for BSM physics (supersymmetry, dark matter, etc.);
- the ALICE [49] detector is optimized to study heavy-ion collisions at  $\sqrt{s} = 2.76$  TeV per nucleon pair. The resulting temperature and energy density are expected to be high enough to produce the quark-gluon plasma, a state of matter where quarks and gluons are freed. Its main goal is the

study of strongly interacting matter at extreme energy densities;

- the LHCb [50] detector focuses its goals on the study of B mesons physics, and it is primarily designed to measure the parameters of CP violation in the disintegration of B hadrons.

### 3.1.1. A proton's journey: destination LHC

The CERN's proton accelerator complex is a chain of accelerators that gradually bring the energy of the protons to their nominal value. The proton source is hydrogen gas. The hydrogen is passed through an electric field that strips off its electrons, leaving only protons to enter the accelerator. Since the acceleration process occurs due to radiofrequency cavities, the protons are accelerated in packets or *bunches*, in order to be synchronous with the accelerating electric field.

The first step of the acceleration process takes place in a linear accelerator called LINAC2, which brings the energy of the protons to 50 MeV. The protons are then injected into the Proton Synchrotron Booster, composed of four superimposed synchrotron rings, that brings the energy up to 1.4 GeV. Next, the Proton Synchrotron splits the proton bunches into smaller bunches, providing *trains* of 72 bunches separated by 25 ns, and accelerates them up to 25 GeV. Then, the bunches are injected into the Super Proton Synchrotron (SPS), a 6.9 km circumference circular accelerator, where they are further accelerated to 450 GeV. As well as having its own beamlines (or beam pipes) for fixed-target experiments (currently COMPASS and NA62), the SPS is used for injecting protons in two opposite directions into the final stage of acceleration: the LHC. This circular collider lies in a tunnel of 27 km in circumference and about 100 m underground. The collider tunnel contains two adjacent beam pipes: the two beams circulate in opposite directions in the two beam pipes. The beam pipes intersect at four points along the ring, which is where the particle collisions take place as described above. The proton beams are kept on their circular path by 1232 dipole magnets, that reach a magnetic field of 7.7 T at a beam energy of 6.5 TeV. An additional 392 quadrupole magnets are used to keep the beams focused, with stronger quadrupole magnets close to the intersection points in order to maximize the chances of interaction where the two beams cross. Since these magnets are superconducting, their operating temperature is kept at 1.9 K (-271.25 °C) with superfluid helium-4. A schematic overview of the CERN's accelerator complex is depicted in Fig. 3.1. This acceleration scheme was used up to 2018. During the so-called Long Shutdown 2 in 2019-2020, the accelerator complex will undergo some changes. For instance the LINAC2 will be replaced by LINAC4, which will accelerate negative hydrogen ions to 160 MeV and then stripped of the two electrons before being injected into the Proton Synchrotron Booster.

The standard LHC beam production and filling scheme foresaw 2808 bunches, each bunch containing  $1.5 \times 10^{11}$  protons in a beam size of  $3.5 \mu\text{m}$ . However, since 2016, a new beam production scheme called Batch Compression Merging and Splitting (BCMS) [52] was developed. It entails the same number of protons per bunch, 2220 bunches per beam, and the beam size is reduced to around  $2.5 \mu\text{m}$ . This ensures much higher brightness.

### 3.1.2. Luminosity and pileup

Besides collision energy, luminosity is the most important parameter in a collider. The number of events per second generated in the LHC collisions is given by:

$$N_{event} = L\sigma_{event} \quad (3.1)$$

where  $\sigma_{event}$  is the cross section of the event under study and  $L$  is the *instantaneous luminosity*, that is, the number of events per unit of time and cross section. It can be seen from Eq. 3.1 that it is crucial to maximize the luminosity in order to increase the number of events produced and hence the chance of discovering new physics. The instantaneous luminosity can be written as follows:

$$L = \gamma \frac{n_b N^2 f_{rev}}{4\pi\beta^* \epsilon_n} R \quad (3.2.)$$

where:

- $\gamma$  is the proton beam energy in unit of rest mass;
- $n_b$  is the number of bunches in the machine (nominal is 2808 for bunch crossing every 25 ns);
- $N$  is the bunch population (nominal is  $1.5 \times 10^{11}$  protons for bunch crossing every 25 ns);
- $f_{rev}$  is the revolution frequency (11.2 kHz);
- $\beta^*$  is the beam beta function at the collision point (nominal is 0.55 m). This parameter quantifies how narrow the beam is: the lower  $\beta^*$ , the narrower (i.e. the more "squeezed") the beam;
- $\epsilon_n$  is the transverse normalized emittance (nominal is  $3.75 \mu\text{m}$ ). A low emittance particle beam is a beam where the particles are confined to a small distance and have nearly the same momentum. In a colliding accelerator, keeping the emittance small means that the likelihood of particle interactions will be greater, resulting in higher luminosity. The transverse emittance is the emittance measured in the two directions perpendicular to the beam direction. The normalized emittance is constant with the acceleration, as opposed to the emittance which is inversely proportional to the momentum of the particles;

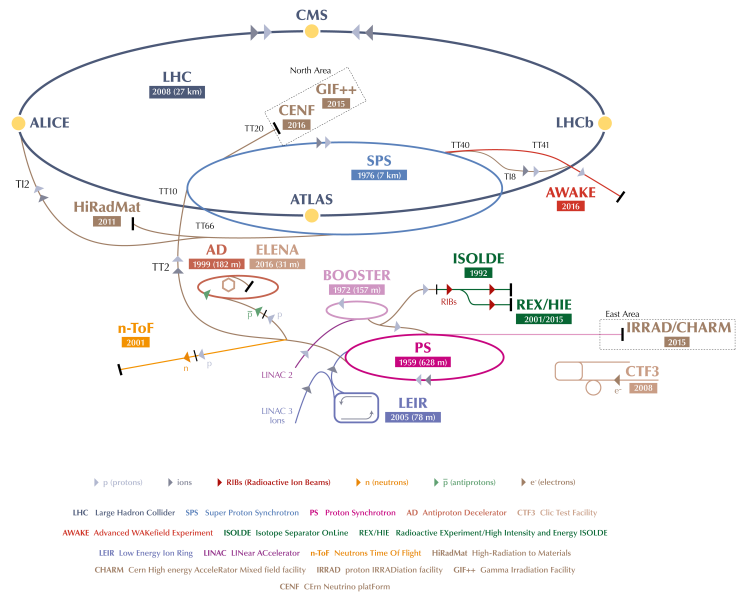


Figure 3.1. | CERN’s accelerator complex [51] up to 2018.

- $R$  is a correction factor (nominal is 0.85 for nominal  $\beta^*$ ).

With these parameters, the nominal (design) LHC luminosity is  $\sim 10^{34} \text{s}^{-1} \text{cm}^{-2}$  [53]. For measurement purposes, a relevant parameter is the luminosity integrated over time or *integrated luminosity*. Figure 3.2 shows how the integrated luminosity recorded by the CMS experiment in proton-proton (pp) collisions increased over the past years (from 2010 to 2018).

As explained above, the LHC beam is bunched rather than continuous. Every time that two bunches collide, multiple protons can interact with each other. The total pp interaction cross section  $\sigma^{pp}$  is  $\sim 100$  mb, comprising elastic and inelastic scattering processes. To discover new physics, we are mostly interested in *hard scattering* processes, that is, processes that involve large momentum transfer. However, these processes are very rare and represent only a tiny fraction of the total inelastic pp cross section  $\sigma_{in}^{pp}$ , which is about 70 mb. Hard collisions are therefore contaminated by several soft ones. This effect is known as *pileup*, and pollutes the reconstruction of the final state of the collision. We have seen that maximizing the luminosity is crucial to increase the number of events generated and hence the chance of observing hard scattering ones. However, this inherently implies a growth of the mean number of interactions per bunch crossing  $\langle \mu \rangle$  (average pileup). In the 2016 and 2017+2018 data taking periods, CMS recorded  $\langle \mu \rangle = 23$  and  $\langle \mu \rangle = 32$ , respectively.

### 3.1.3. A long-term plan: towards High-Luminosity LHC

The LHC operations are committed to a schedule that spans over many years, and foresees a series of data taking periods or *runs*, where hadrons are collided and the information is recorded by the detectors, alternated with periods of maintenance and upgrade of both the accelerators and the detectors. This aims at increasing the center-of-mass energy and/or the luminosity and at making the detectors suitable for higher and higher-radiation environments, as well as to improve the performance of the detectors. The first beam was circulated through the LHC in September 2008. However, nine days after the start of the run, an incident occurred due to a faulty electrical connection between two of the accelerator's magnets. This resulted in mechanical damage and release of helium from the magnet into the tunnel, forcing the operations to stop immediately. Most of the following year was spent on repairs and reviews from the damage. The run started again at the end of 2009, and continued smoothly until 2013. This is called *Run 1*. During Run 1, protons were collided at a center-of-mass energy of 7 and subsequently 8 TeV, collecting data at an integrated luminosity of  $30 \text{ fb}^{-1}$ .

A period of shutdown of the accelerator followed, called *Long Shutdown 1* (LS1), where upgrades were performed to bring the energy of the protons up to 13 TeV and increase the machine luminosity. *Run 2* started in 2015 and continued up

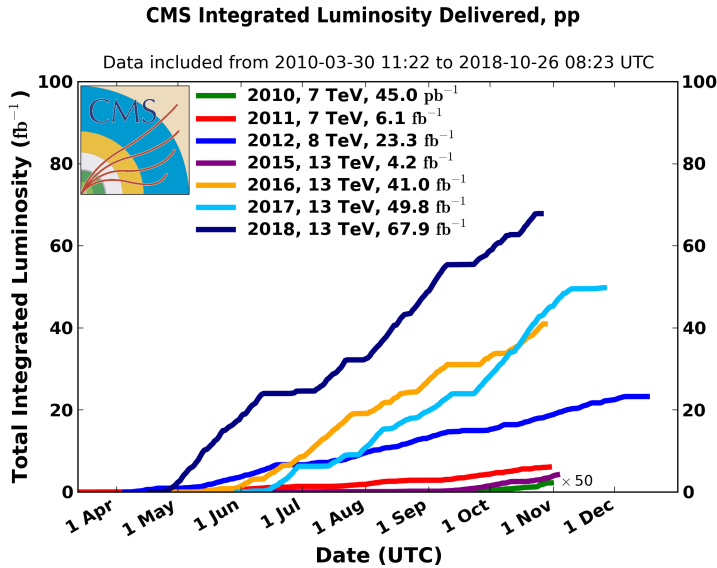


**Figure 3.2.** | Total integrated luminosity delivered by the LHC and recorded by the CMS experiment from 2010 to 2018 [54].

to the end of 2018. During this run, the instantaneous luminosity reached twice its design value and the protons were collided at a center-of-mass energy of 13 TeV. The integrated luminosity reached at the end of the run was of  $150 \text{ fb}^{-1}$ . Currently, the *Long Shutdown 2* (LS2) is ongoing, where an upgrade of the accelerator is performed in order to bring the center-of-mass energy potentially up to 14 TeV, as dependent on the current that can be held by the dipole magnets, and the luminosity to twice its design value. After LS2, *Run 3* is foreseen to start in 2021 and last three years. At the end of this run, the integrated luminosity is expected to reach  $300 \text{ fb}^{-1}$ .

From 2024 to mid-2026, the *Long Shutdown 3* (LS3) is scheduled to prepare for the *High-Luminosity LHC* (HL-LHC) era. The objective is to increase the instantaneous luminosity by a factor 5 to 7 beyond the original design value and the integrated luminosity by a factor 10, in order to enhance the potential for discoveries after 2025. The new machine configuration will rely on a number of innovative technologies such as the use of cutting-edge 11-12 T superconducting magnets, new technology for beam collimation and high-power superconducting links with almost zero energy dissipation [55]. The detectors will therefore undergo major upgrades as well. For the CMS detector, this includes, among others, a new tracker, a high-granularity calorimeter and a muon spectrometer with increased sensitivity. The LHC baseline plan is summed up schematically in Fig. 3.3.

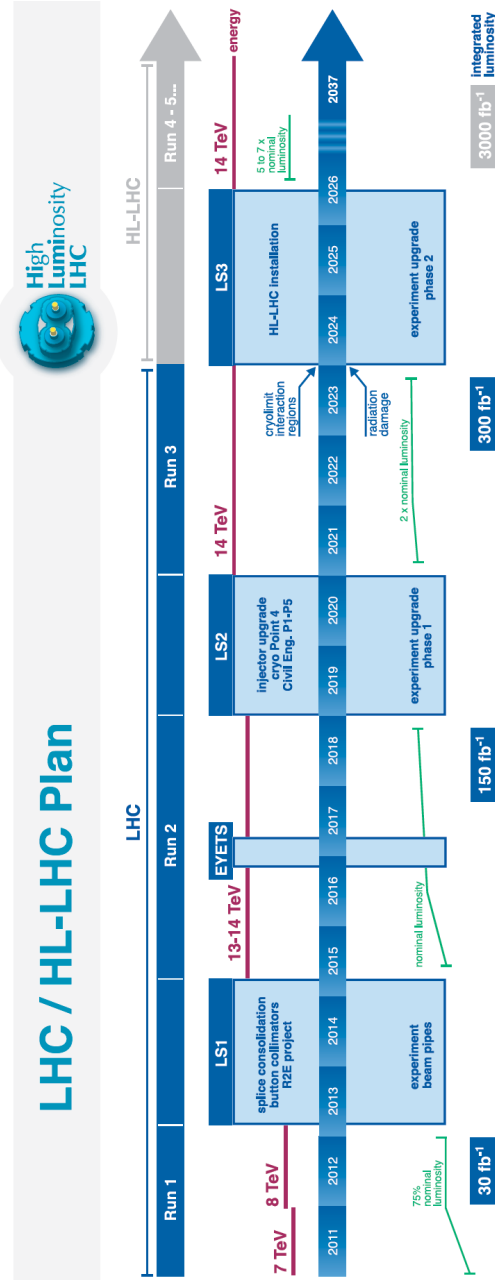


Figure 3.3. | LHC baseline plan for the next decade and beyond showing the energy of the collisions (upper red line) and luminosity (lower green lines) [56].

### 3.2. The CMS detector

The CMS experiment is one of the two large general-purpose particle physics detectors built on the LHC. It is located at Cessy, in France, about 100 meters underground. One of the main achievements of the CMS collaboration was the discovery of the Higgs boson, in July 2012, along with the ATLAS collaboration [2].

The geometry and structure of the CMS detector is specifically conceived for head-on collisions in order to maximize particle detection and reconstruction performance. Its shape is cylindrical, with the beam pipe placed along the axis of the cylinder and the two LHC beams colliding in the middle of the detector. It is 21.6 meters long with a diameter of 15 meters, and weighs about 14,000 tonnes.

Since particle detection occurs by exploiting the properties of the interaction between particles and matter, the detector consists of concentric layers of material, each optimized for specific purposes. The interaction of the particles emerging from high-energy collisions with the material of these sub-detectors generates an electric signal. For instance, charged particles passing through silicon detectors generate ionization currents; particles impinging on a scintillating material produce scintillation light; particles traversing a transparent material might produce Cherenkov [57] photons. All these signals are measured and digitized and are eventually analyzed by computers.

An exceptional feature of the detector is its solenoid magnet, inside which the inner part of the detector is built. This takes the form of a cylindrical coil of superconducting cable that generates a 4 T magnetic field parallel to the beam line. Outside the solenoid, the muon detectors are installed in the iron return yoke frame. A schematic view of the CMS detector is given in Fig. 3.4.

The CMS experiment uses a right-handed coordinate system, with the origin at the nominal collision point, the  $x$ -axis pointing to the center of the LHC ring, the  $y$ -axis pointing up (perpendicular to the LHC plane), and the  $z$ -axis along the anticlockwise beam direction. The polar angle ( $\theta$ ) is measured from the positive  $z$ -axis and the azimuthal angle ( $\phi$ ) is measured from the positive  $x$ -axis in the  $x - y$  plane. The radius ( $r$ ) denotes the distance from the  $z$ -axis and the pseudo-rapidity is defined as  $\eta = -\ln[\tan(\theta/2)]$ . A pseudo-solid angle ( $\Delta R$ ) is defined as a distance in the  $\eta - \phi$  plane as  $\Delta R = \sqrt{(\Delta\eta)^2 + (\Delta\phi)^2}$ .

The experiment has almost a full solid angle coverage and it can be divided into three sectors: the central barrel, covering a pseudo-rapidity region  $|\eta| < 1.48$ , and the two end-caps, installed at both sides of the barrel, which extend coverage to  $|\eta| = 3$ . The pseudo-rapidity coverage is further extended in the

forward and very forward regions of the detector up to  $|\eta|=5$ .

The innermost sub-detector of CMS is the tracker (Pixel detector and Silicon Strip tracker), followed by the electromagnetic calorimeter (ECAL) and the hadronic calorimeter (HCAL). Outside the coil there is the muon system, made of Cathode Strip Chambers, Resistive Plate Chambers, and Drift Tubes. A short overview of each of these detector components is given in the next subsections, together with a description of the trigger system. A thorough description of these sub-detectors can be found at Ref. [58].

### 3.2.1. The inner tracker

The CMS inner tracker is the closest detector to the interaction point. It consists of a pixel detector, that has the main task to define the position of the vertices (origins of the charged-particle trajectories along  $z$ ), and of a silicon strip tracker, which allows for the measurement of the momentum of charged particles due to the bending of their tracks in the homogeneous magnetic field. Tracks are reconstructed with very high efficiency within the pseudo-rapidity range  $|\eta| < 2.5$ . The geometry of the CMS tracking system is depicted in Fig. 3.5.

The pixel detector consists of:

- **a barrel region**, made up of 53 cm long layers at  $r = 4.4, 7.3$ , and 10.2 cm. The space resolution is  $10 \mu\text{m}$  along the  $r - \phi$  plane and  $15 \mu\text{m}$  along  $z$ ;
- **two end-cap disks** at  $|z| = 34.5$  and 46.5 cm covering a radius from 6 to 15 cm. The space resolution is  $15 \mu\text{m}$  along the  $r - \phi$  plane and  $20 \mu\text{m}$  along  $z$ .

Each layer is composed of  $100 \times 150 \mu\text{m}^2$  silicon pixels. Every pixel generates a digital signal when hit by a charged particle. Specific algorithms allow to measure the curvature of tracks, reconstructed from the hits left by particles along their trajectories.

The silicon strip tracker is the outermost part of the tracker and covers the region with radius between 20 and 120 cm. The barrel region is equipped with ten layers of microstrips, while every end-cap region ( $1.5 < |\eta| < 2.5$ ) has three inner mini-disks and nine outer disks. The detector is divided in four parts:

- **Tracker Inner Barrel (TIB)**: it contains the four innermost layers of the barrel region, covering up to  $|z| < 65$  cm and  $r < 55$  cm. Strips have a cell size of  $10 \text{ cm} \times 80 \div 120 \mu\text{m}^2$  and they are parallel to the beam pipe. It provides position measurements in the  $r - \phi$  plane with a resolution of approximately  $13\text{-}38 \mu\text{m}$ ;
- **Tracker Outer Barrel (TOB)**: it contains the six outermost layers of the barrel region, covering up to  $|z| < 110$  cm and  $r > 55$  cm. Strips have a cell size of  $25 \text{ cm} \times 120 \div 180 \mu\text{m}^2$ . It provides position measurements in the  $r - \phi$  plane with a resolution of approximately  $18\text{-}47 \mu\text{m}$ ;

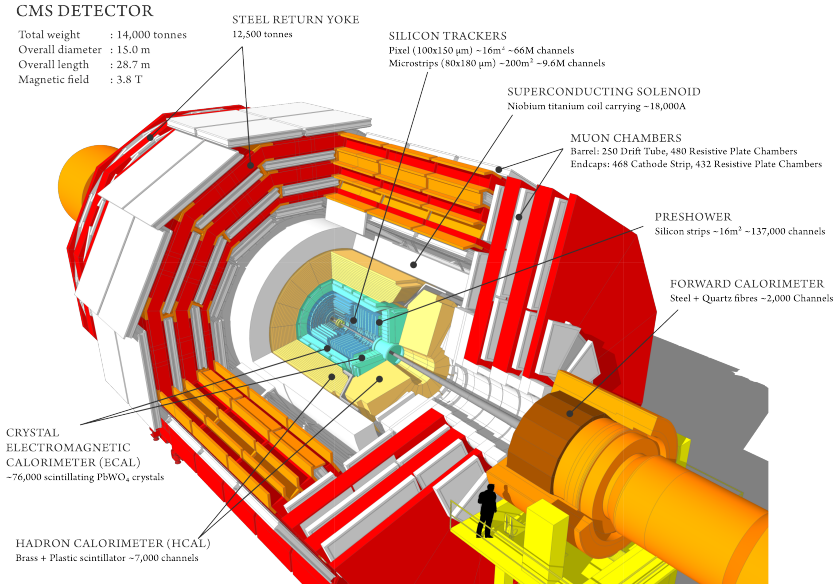


**Figure 3.4.** | Sectional view of the CMS detector [59]. The LHC beams travel in opposite directions along the central axis of the CMS cylinder colliding in the middle of the CMS detector.

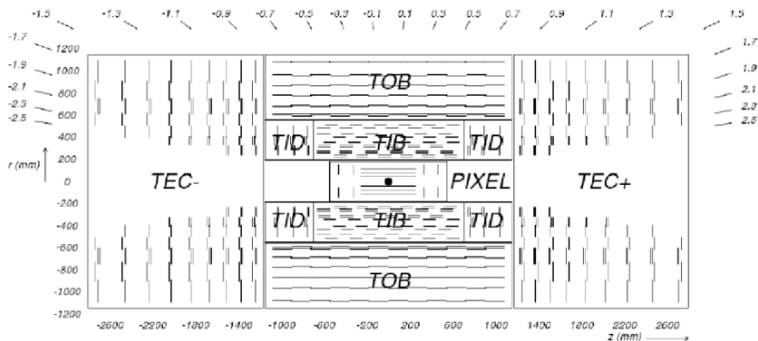


**Figure 3.5.** | View of the CMS tracker in  $r$ - $z$  plane. It shows the pixel and the strip detectors [16].

- **Tracker Inner Disks (TID):** it contains three mini-disks per side, covering the region  $65 < |z| < 120$  cm and  $20 < r < 55$  cm. It provides position measurements in  $\phi$  with a resolution of approximately 15 (50)  $\mu\text{m}$  at low (high)  $r$ ;
- **Tracker End-Caps (TEC):** it covers the region  $120 < |z| < 282$  cm. Each TEC is composed of nine disks, divided in seven to four rings according to the pseudo-rapidity considered. The resolution on the measurement of the position is roughly the same as the TID.

The first two layers of the TIB and TOB are made of two single-sided modules mounted back to back at a stereo angle of 100 mrad providing a 3D view of the impact point, thus improving the tracks reconstruction.

The basic unit of the silicon strip tracker is made up of a module, housing 512 or 768 silicon strips (depending on the location in the tracker) and a Front-End Hybrid (FEH) for signal readout. The signals of the strips of a module are processed by four or six APV25 readout chips, mounted on the FEH. The analogue data from pairs of APV25 chips are converted to optical signals before being transmitted via optical fibers to the off-detector Front-End Driver (FED) boards. The FEDs digitize, process and format the data from up to 96 APV25 pairs before forwarding zero-suppressed data to a computing farm for further event filtering.

Within the tracking region, cables, the cooling system, and more in general the whole mechanical structure of the detector constitute a *material budget* that poses some limitations to the track reconstruction efficiency, since this will induce multiple scattering effects, bremsstrahlung and nuclear interactions of the particles with the material. The material budget in unit of radiation length of the CMS detector is shown in Fig. 3.6.

### 3.2.2. The CMS calorimeters

A calorimeter is an experimental apparatus that measures the energy of particles. A particle impinging on the material of the calorimeter initiates a particle shower that develops throughout the material until it is partially or fully absorbed. There exist various types of calorimeters for high-energy particle physics. Examples are Cherenkov calorimeters, where Cherenkov light is produced by the relativistic electrons in the shower, and scintillating calorimeters, where the material is excited by ionizing radiation and fluorescence light is emitted.

Specifically, an electromagnetic calorimeter is designed to measure the energy of particles that interact primarily via the electromagnetic interaction (electrons and photons), while a hadronic calorimeter is designed to measure particles that interact via the strong nuclear force. It is important to stress that particles carrying a color charge, such as quarks and gluons, cannot exist in free

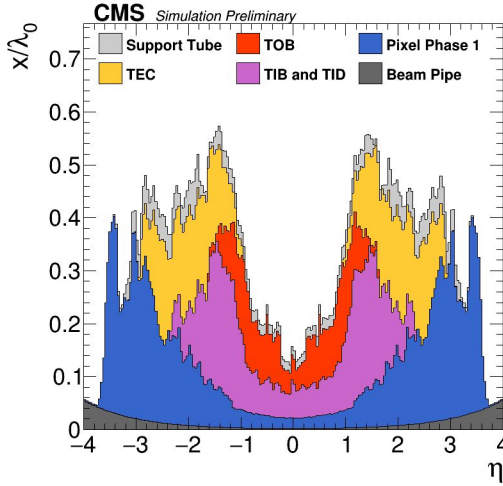


**Figure 3.6.** | Material budget in unit of hadronic interaction length  $\lambda_0$  as a function of the pseudo-rapidity  $\eta$ . The contribution of the support tube (light gray), the beam pipe (dark gray), and sub-detectors: TOB (red), Pixel (blue), TEC (yellow) and TID+TIB (magenta) are stacked [60].

form because of QCD confinement which only allows for colorless states [61]. Therefore, only a narrow cone of hadrons and other particles produced by the hadronization of a quark or gluon, called *jet*, can be detected in the hadronic calorimeter.

Important variables in the description of an electromagnetic calorimeter are: the *radiation length*  $\lambda_0$  (average distance that an electron needs to travel in a material to reduce its energy to  $1/e$  of its original energy); and the *Molière radius* (average lateral deflection of electrons after traversing one radiation length). For a hadronic calorimeter, the *interaction length*  $\lambda_I$  is defined similarly to the radiation length, typically bigger than  $\lambda_0$ . These parameters depend on the material that the calorimeter is made of.

### The electromagnetic calorimeter

The CMS electromagnetic calorimeter (ECAL) is a scintillating hermetic, homogeneous, fine grained lead tungstate ( $PbWO_4$ ) crystal calorimeter. The barrel region (EB) is composed of 61,200 crystals with a front face cross-section of  $22 \times 22 \text{ mm}^2$  and a length of 230 mm ( $25.8\lambda_0$ ), placed with an inner radius of 129 cm and tilted at 3 degrees. The end-caps (EE) are 7,324 crystals with a front face of  $28.6 \times 28.6 \text{ mm}^2$  and a length of 220 mm ( $24.7\lambda_0$ ). It covers the rapidity range  $1.479 < |\eta| < 3.0$ . In the region between  $1.65 < |\eta| < 2.6$ , a 20 cm thick preshower detector is placed between the tracker and the ECAL end-caps. It is made of two lead radiators interleaved with two silicon strip detectors.

The preshower increases the ECAL radiation length, enhancing the  $\gamma - \pi_0$  discrimination.

The electromagnetic energy resolution is parametrized by:

$$\frac{\sigma}{E} = \frac{a}{\sqrt{E}} \oplus \frac{b}{E} \oplus c \quad (3.3.)$$

where  $E$  is the energy of the particle; the first term on the right-hand side is the *stochastic* term, and includes intrinsic energy fluctuations in the shower; the second term is the *noise* term, and includes electronic noise and/or energy fluctuations initiated by external sources; the third term is a *constant* term, including constant discontinuities such as calibration errors and/or non-uniformity in the digital signal acquisition.

The coefficients in Eq. 3.3 are measured to be:  $a = 2.8\%$  (5%)  $\text{GeV}^{1/2}$  in the barrel (end-caps);  $b = 0.125(0.5)$   $\text{GeV}$  in the barrel (end-caps);  $c = 0.3\%$  in both barrel and end-caps, with  $E$  measured in  $\text{GeV}$  [62].

### The hadronic calorimeter

The CMS hadronic calorimeter (HCAL) is divided into four distinct subsystems: the barrel (HB), end-cap (HE), outer (HO) and forward (HF) calorimeters, as shown in Fig. 3.7. The HB and HE, which are inside the cryostat of the CMS superconducting solenoid, are sampling calorimeters (in which the material that produces the particle shower is distinct from the material that measures the deposited energy). The absorber material is brass and the active material is scintillator. The HB covers the  $|\eta|$  range from zero to approximately 1.4; the  $|\eta|$  range between 1.3 and 1.4 is shared by the HB and the HE; the HE covers  $|\eta|$  from 1.3 to 3.0. The HB is built of 17 wedges, each of which covers 20 degrees in  $\phi$ , and are divided in 5 sectors. It is 5.8 interaction lengths thick at  $\eta = 0$  and it reaches 10 interaction lengths at  $\eta = 1.2$ . The HE is made of brass disks, interleaved with scintillator wedges which cover 20 degrees in  $\phi$ , which in turn are divided in four 5-degree sectors. Layers of tiles in depth are called *towers*. To catch the energy leakage from HB, layers of scintillators are placed outside the solenoid cryostat: they constitute the HO. Here, the CMS magnet coil/cryostat and the steel of the magnet return yoke are used as absorber. About 5% of all hadrons above 100  $\text{GeV}$  deposit energy in the HO [64].

The HF is placed at  $\pm 11.15$  m from the interaction point and covers a pseudo-rapidity up to 5. It is made of steel absorbers and quartz fibers as active material, that causes the production of Cherenkov radiation when particles pass through the fibers. Such a design is essential to improve the detection of forward jets and of particles scattered in the very forward region.

For the CMS detector, the hadronic energy resolution can be parametrized as:

$$\frac{\sigma}{E} = \frac{a}{\sqrt{E}} \oplus b \quad (3.4.)$$

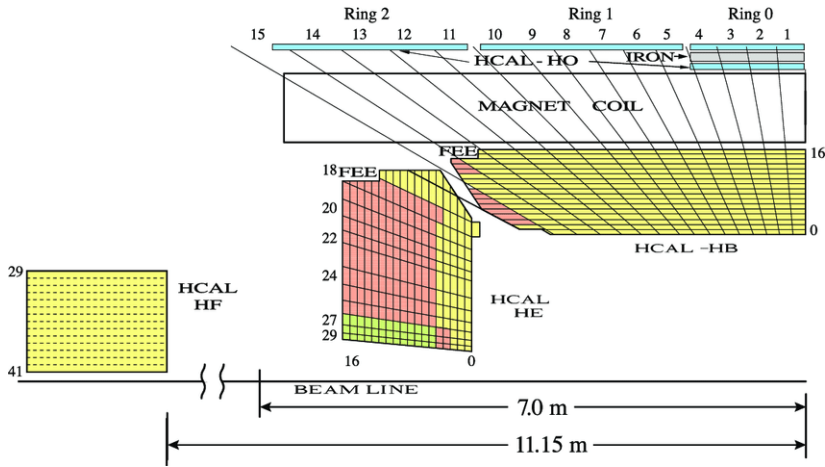


**Figure 3.7.** | A sketch of the CMS hadronic calorimeter [63]. The numbers on top and on the left refer to the tower numbers.

where the first term on the right-hand side is the stochastic contribution and the second term is constant, similarly to Eq. 3.3. These coefficients are measured to be:  $a = 0.85$  (1.98)  $\text{GeV}^{1/2}$  in the barrel (endcaps);  $b = 0.074$  (0.09) in the barrel (endcaps) [65], with  $E$  measured in GeV.

### 3.2.3. The muon detector

Outside the magnet, the CMS muon detector system is placed, interleaved with the steel return yoke. This has three primary functions: muon triggering, identification, and momentum measurement.

The basic detection process used in the muon system detector is gas ionization. Charged particles that traverse the muon detector ionize the gas in the chambers, which eventually causes electric signals to be produced on the wires and strips. These signals are read out by electronics and are associated with well-defined locations, called *hits*, in the detector. The precise location of each hit is reconstructed from the electronic signals using different algorithms depending on the detector technology.

The muon system uses three different technologies to detect and measure the muons; drift tubes (DTs) in the barrel region, cathode strip chambers (CSCs) in the end-cap region, and resistive plate chambers (RPCs) in both barrel and end-cap. For all the three different technologies, the basic physical modules are called *chambers*. The muon chambers measure the traversing muon track, bent by the presence of the magnetic field, at several points, thus allowing for momentum measurement. At  $|\eta| < 1.2$ , the muon system is then still inside a return magnetic field of  $\sim 2$  T, oriented backwards with respect to the inner field. Muons in this region are bent in the reverse direction drawing a characteristic

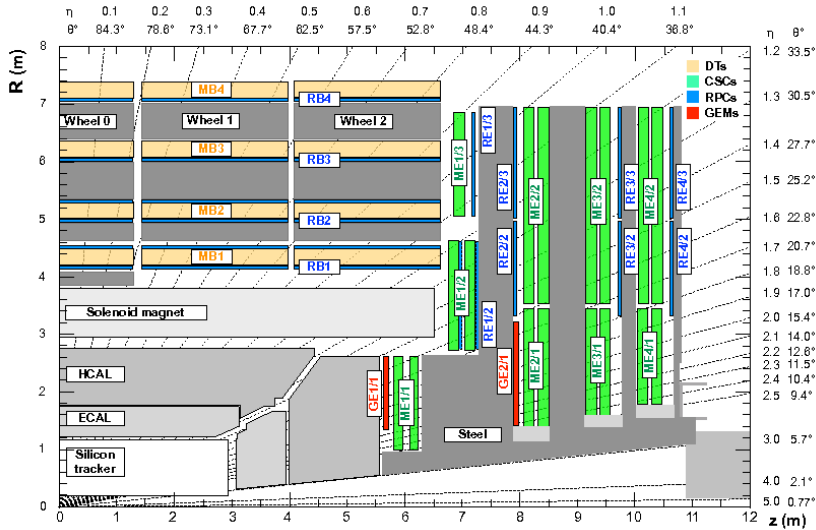


**Figure 3.8.** | A sketch of the CMS muon detector system [66].

S-shaped trajectory. In order to measure the muon track with high precision, in the barrel region chambers are positioned at several different values of  $r$  from the beam line, and in the end-cap region at several different values of distance along  $z$ . A *station* is an assembly of chambers around a fixed value of  $r$  (in the barrel) or  $z$  (in the end-cap). There are four stations in the barrel and in each end-cap, labeled MB1-MB4 and ME1-ME4, respectively. Along  $z$ , the DT and RPC in the barrel are divided into 5 *wheels*, with wheel 0 centered at  $z = 0$  and wheels  $W+1$  and  $W+2$  ( $W-1$  and  $W-2$ ) in the  $+z$  ( $-z$ ) direction. Similarly, in the  $r$  direction in the end-caps, there are *rings* of RPC and CSC. The latter are labeled ME1/ $n$ -ME4/ $n$ , where integer  $n$  increases with the radial distance from the beam line.

Figure 3.8 shows a sketch of the CMS muon detector system. The spatial resolution in the  $r - \phi$  plane is  $\sim 100 \mu\text{m}$ , while the time resolution is 5, 6, and 3 ns for DT, CSC, and RPC, respectively [67].

### 3.2.4. The trigger system

The LHC collides proton bunches every 25 ns, with a pp interaction rate that reaches very high values (40 MHz). At such a rate, CMS would then need to read, process, and store tens of terabytes per second. Nevertheless, only a small fraction of these collisions contains events of interest to the CMS physics program, and only a small fraction of those can be stored for later offline analysis. It is the job of the trigger system to select the interesting events for offline storage from the bulk of the inelastic collision events.

To select events of potential physics interest, CMS uses a trigger system consisting of two levels: Level 1 (L1) and high-level trigger (HLT). A description of these is given below.

## Level 1 trigger

The CMS Level 1 trigger (L1) is a hardware system. Within  $3.8 \mu\text{s}$  of a collision, the L1 trigger system decides if an event should be tentatively accepted or rejected using information from the calorimeter and muon detectors. A global decision is taken based on the presence of energy deposits compatible with physics objects such as photons, electrons, muons, jets or hadronically decaying tau leptons. A schematic view of the L1 trigger system is depicted in Figure 3.9. The L1 is split into two sub-systems, working in parallel: the Calorimeter Trigger, and the Muon Trigger. The Calorimeter Trigger processes data from ECAL and HCAL (including HF), segmented into trigger towers corresponding to detector regions in  $\Delta\eta \times \Delta\phi$  of about  $0.087 \times 0.087$ . This size corresponds to HCAL towers and to  $5 \times 5$  ECAL crystals. Each trigger tower encodes the energy deposits in the calorimeters at a specific position. The trigger exploits this information by clustering together the trigger towers and applying some requirements in order to reconstruct electrons/photons and hadronic candidates and pass them on to the final stage, the Global Trigger (GT).

At the same time, the Muon Trigger receives information from the DTs, CSCs and RPCs. For the DTs and CSCs, the front-end trigger electronics identifies track segments from the hit information registered in these sub-detectors. These segments are collected and transmitted via optical fibers to regional track finders in the electronics service cavern, which then applies pattern recognition algorithms that give a rough estimate of the muon position, direction and bending angle. For the RPCs, adjacent hits are clustered together. These segments and hits are then sent to the muon track finder which reconstructs the candidate muon. In a further stage, the identified muon candidates found by more than one system are merged to eliminate a single candidate passing multiple-muon triggers, then they are sorted and transmitted to the global muon trigger (GMT). The GMT also exploits information from the Calorimeter Trigger to compute the pileup-corrected muon isolation, and forwards up to eight candidates to the next layer, the GT. This is the final stage of the L1 trigger, combining calorimeter and muon candidates. Here, a decision is made whether to *trigger* the event for read out or not by a menu of triggers (a menu contains up to 512 conditions or *trigger paths*, based on the candidates position, momentum, reconstruction quality, and isolation, that are evaluated in the decision process) [68]. The L1 trigger system restricts the output rate to 100 kHz for subsequent processing [69].

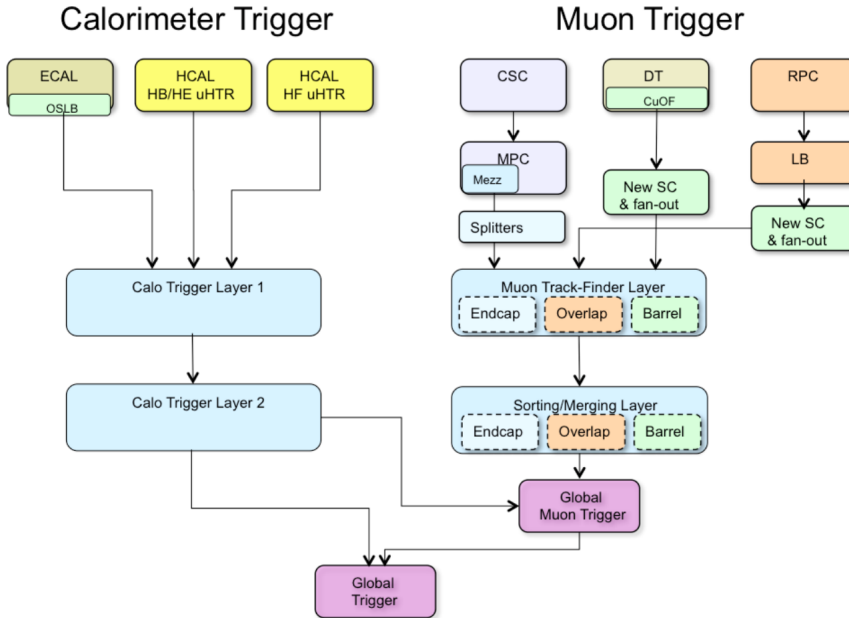


**Figure 3.9.** | A schematic view of the CMS L1 trigger system as of 2016 [68].

### High-level trigger

The second level of the CMS trigger system is the high-level trigger (HLT), implemented in software, that further refines the purity of the output stream, selecting an average rate of 400 Hz for offline event storage. The data processing of the HLT is structured around the concept of an *HLT path*, which is a set of algorithmic processing steps run in a predefined order, that both reconstructs physics objects and makes selections on these objects. Each HLT path is implemented as a sequence of steps of increasing complexity, reconstruction refinement, and physics sophistication [69]. The events that pass the HLT step are stored and ready for offline reconstruction and analysis. The output rate is narrowed down to 1 kHz, a significant decrease with respect to the initial 40 MHz rate delivered by the LHC.

### 3.3. Object reconstruction

The CMS detector records digital particle information in the various sub-detectors, each optimized for a specific task, as seen in Section 3.2. For the purpose of a thorough event reconstruction essential for offline analysis, particle objects (muons, electrons, photons,  $\tau$  leptons, jets, and missing transverse energy) must be reconstructed starting from the raw information. In CMS, this is achieved via crossing the information between the various sub-detectors and applying specific algorithmic processing, with a technique called *Particle Flow*

(PF) [70].

In this section, an overview of the identification and reconstruction techniques of the various physics objects is presented, starting from low-level objects such as tracks and vertices to more complicated objects such as b jets.

### 3.3.1. Tracks and vertices

The process of track reconstruction proceeds through two phases: local and global reconstruction. In the first phase, zero-suppressed signals above specified thresholds in pixel and strip channels are clustered into hits, and then the cluster positions and their uncertainties are estimated. In the second phase, tracks are constructed from groups of these hits.

**Local reconstruction.** In the data acquisition system of the pixel detector, zero-suppression is performed in the readout chips of the sensors, with adjustable thresholds for each pixel. Offline, pixel clusters are formed from adjacent pixels, including both side-by-side and corner-by-corner adjacent cells. Algorithms are used to determine the position of pixel clusters.

In the silicon strip tracker, the local reconstruction proceeds as follows. The signal from each strip is pulse-shaped in its corresponding APV25 channel. The FEDs can format these raw data in four different ways:

- *Scope Mode*: it consists of a bare capture of the raw data within a given time window of configurable size. It is used for detector commissioning;
- *Virgin Raw*: it provides the digitized pulse height data from the sensors and is used for detector testing, commissioning, and calibration;
- *Processed Raw*: data are reordered to reflect the strip order and pedestals are subtracted;
- *Zero-suppressed*: it is the normal FED operating mode. The zero-suppression algorithm applies a configurable threshold to the signals. Pedestals and common-mode noise are also subtracted.
- *Zero-suppressed lite*: like zero-suppression, but carries less information. This is designed for high luminosity data taking.

The raw data output from each FED encodes the basic hit information necessary for the tracking. Among the four readout modes, zero-suppression is the default operation mode for pp collisions. These raw data need to be interpreted and the strip information extracted (known as *digis*). This process is the so-called *unpacking* of the data. I was involved in the maintenance of the CMS silicon strip local reconstruction software, specifically in the development of the unpacker for support of zero-suppressed lite readout modes and fixes in the packer, used in simulation to repack data collected from heavy-ion collisions in the HLT.

After unpacking, neighboring digis are grouped via a dedicated algorithm in a process called *clustering*. Finally, the clusters are translated into possible

hit measurements. This is done with a cluster parameter estimator algorithm. The hits are assigned a position and a corresponding uncertainty in a local orthogonal coordinate system in the plane of each sensor, in a process called *cluster parameter estimate* [71,72]. With this information, global reconstruction of tracks can be performed.

**Global reconstruction.** The algorithm for track reconstruction used in CMS is called *combinatorial track finder* (CTF), and can be decomposed into four main logical parts:

- **Seed generation:** it provides initial track candidates found using only 2 or 3 hits from the innermost tracker layers;
- **Trajectory building:** this step consists in an outwards extrapolation of the track path. It begins with a coarse estimate of the track path provided by the trajectory seed, and then builds track candidates by looking for hits from successive detector layers, compatible with the extrapolated track path. If such hits are found, the track parameters are updated. The information needed at each layer includes the location and uncertainty of the detected hits, as well as the amount of material crossed [73]. This procedure is repeated until no valid hit is found anymore or the tracker material has ended;
- **Track fitting:** after building the trajectory, this step provides the best possible estimate of its parameters:  $d_0$ , distance in the transverse plane between the origin and the point of closest approach between the track and the beam axis (impact point);  $z_0$ , longitudinal coordinate of impact point;  $\phi_0$ , azimuthal angle of the track at impact point;  $\theta$ , polar angle of the track;  $p_T$ , the transverse momentum;
- **Track selection:** the track of a single charged particle can be reconstructed more than once, either starting from different seeds, or when a given seed develops into more than one track candidate. To remedy this feature, one calculates the fraction of shared hits between two track candidates:
 
$$f_{shared} = \frac{N_{shared}^{hits}}{\min(N_1^{hits}, N_2^{hits})}$$
 where  $N_1^{hits}$  and  $N_2^{hits}$  are, respectively, the number of hits used in forming the first (second) track candidate. If this fraction exceeds the (configurable) value of 19% (determined empirically), the track with the fewest hits is removed; if both tracks have the same number of hits, the track with the largest  $\chi^2$  value is discarded. The procedure is repeated iteratively on all pairs of track candidates [73].

The four steps listed above are repeated iteratively in order to maximize the track reconstruction efficiency and minimize the number of falsely reconstructed (fake) tracks. Each iteration works on the hits that in the previous iterations were not associated to the highest quality tracks.

When particles are produced at the same place in a pp collision, their tracks originate from a common point, within uncertainties, called a *vertex*. Because of inelastic pp interactions, one single bunch crossing gives rise to many vertices: one signal vertex, containing the interaction of interest, and other vertices originating from pileup interactions (in 2016, this translates into 1 signal vertex out of  $\sim 23$  minimum-bias vertices). Moreover, a vertex is called *primary* if it coincides with the interaction point of a pp collision, and *secondary* when it originates from tracks of particles that decay within the detector volume, displaced from the primary vertex due their relatively long lifetime.

Using the available reconstructed tracks, the location and the associated uncertainty of the all pp interaction vertices in each event can be determined. The procedure consists of three steps: selection of the tracks, clustering of the tracks that appear to originate from the same interaction vertex, and fitting for the position of each vertex using its associated tracks [73].

### 3.3.2. Electrons

Since electrons are charged particles and interact electromagnetically, they leave hits in the tracker and clusters (a group of neighboring calorimeter cells containing energy deposits) in the ECAL as they traverse the CMS detector. Therefore, the electron reconstruction algorithms combine information from both these sub-detectors in order to maximize the reconstruction performance. Due to the relatively large amount of material between the interaction point and the ECAL, propagating electrons are likely to emit bremsstrahlung photons before they reach the ECAL. On average, 33% of the electron energy is radiated before it reaches the ECAL where the intervening material is minimal ( $\eta \sim 0$ ), and about 86% of its energy is radiated where the intervening material is the largest ( $|\eta| \sim 1.4$ ) [74]. Some of these photons convert into electron-positron pairs well before the calorimeter, thus leaving energy deposits in the ECAL crystals along a line in the  $\phi$  direction because of the presence of the magnetic field. This spread in energy is grouped along  $\phi$  in a cluster of clusters, called a *super-cluster* (SC). More details about the clustering procedure can be found at Ref. [75]. The reconstruction of an electron consists in matching a SC with a track obtained fitting different hits in the tracker.

The position of the SC is obtained by calculating the energy-weighted mean position of the crystals in the cluster, while the total SC energy is obtained by summing the energy deposits of all crystals of the SC.

Once the electrons have been reconstructed, one needs to apply some identification (ID) criteria in order to discriminate prompt electrons, of interest for the analysis discussed in this thesis, from secondary electrons produced from

photon conversion, misidentified jets, electrons coming from b or c-decays, etc. This is achieved via applying cuts on some well understood variables:

- ratio of energy deposit in the HCAL to the energy of the ECAL SC, of relevance to reject jets with large electromagnetic shower component, as it makes it possible to exploit the geometry of the particle shower;
- $\sigma_{\eta\eta}$  (shower shape along  $\eta$ );
- $\Delta\eta_{in}$  (difference between the  $\eta$  value of the track and the SC);
- $\Delta\phi_{in}$  (difference between the  $\phi$  value of the track and the SC).

According to the entity of the cuts applied, one can distinguish various categories or *working points* (WP), each characterized by a certain identification efficiency. The one used in the analysis presented in this thesis is called *medium* and it has an identification efficiency of 80%.

To further reject jets misidentified as electrons or non-prompt electrons, isolation (ISO) criteria are required as well. Electrons with a small energy flow surrounding their trajectory are indeed more likely to be prompt. This is achieved via comparing the sum of the PF charged hadrons, neutral hadrons, and photons candidates to the energy of the selected electron in a cone of  $\Delta R = \sqrt{\Delta\phi^2 + \Delta\eta^2} = 0.3$  around the electron.

### 3.3.3. Muons

Due to their small interaction cross section, muons are the only charged particles that traverse the whole CMS detector. Muons are minimum ionizing particles<sup>1</sup> (MIPs) and leave corresponding energy deposits in the calorimeters along their trajectory. Therefore, their typical signature consists in hits in the tracker, energy deposits both in the ECAL and HCAL, and finally hits in the muon chambers.

The muon track reconstruction is performed by first locally reconstructing the track in each sub-detector, and subsequently combining the information together with a global fit. First, hits are reconstructed in each of the muon sub-detectors (a detailed description for each of the sub-detectors can be found at Ref. [76]). A track is then built by gathering the information from the three muon sub-detectors together. This is called *standalone-muon track*.

Separately, reconstructed hits in the inner tracker are exploited to build the *tracker track*. These tracks are then propagated to the muon system with loose matching to DT or CSC segments. If at least one muon segment matches the extrapolated track, the tracker track qualifies as a *tracker muon track*.

Then, *global muon tracks* are built by matching standalone-muon tracks with

<sup>1</sup> A minimum ionizing particle (MIP) is a particle with energy loss close to the minimum ( $\sim 2 \text{ MeV/g/cm}^2$ ) as it traverses matter.

tracker tracks. The matching is done by comparing parameters of the two tracks propagated onto a common surface and a combined fit is performed.

Owing to the high efficiency of the tracker track and muon segment reconstruction, about 99% of the muons produced within the geometrical acceptance of the muon system are reconstructed either as a global muon track or as a tracker muon track, and very often as both. Global muons and tracker muons that share the same tracker track are merged into a single candidate [77].

Reconstructed muons are fed into the PF algorithm, where information from all the sub-detectors is combined together in order to identify and reconstruct all individual particles for each event, also applying identification and isolation criteria. Indeed, similarly to the case of the electrons, such criteria need to be applied in order to discriminate prompt muons from muons coming from b or c-decays and from *punch-through* fake muons, i.e. particles passing through the calorimeter and producing hits in the muon chambers. Muons are identified by imposing cuts on some variables based on the muon reconstruction, such as the track fit  $\chi^2$ , the number of hits per track (either in the inner tracker or in the muon system, or both), or the degree of matching between tracker tracks and standalone-muon tracks (for global muons). Different WPs are then defined according to the entity of the cut. For the purpose of the analysis presented in this thesis, a *tight* WP is used for the identification of muons, yielding an identification efficiency of  $\sim 95\%$ .

The combination of the scalar  $p_T$  sum of charged and neutral hadrons and photons, corrected for the contribution of pileup to the muon energy, can be condensed in the following variable:

$$I_{rel} = \frac{\sum p_T^{charg. hadr.} + \max(\sum E_T^{neutr. hadr.} + \sum E_T^\gamma - 0.5 \sum p_T^{charg. PU}, 0)}{p_T^\mu} \quad (3.5.)$$

called *relative isolation*. In the analysis presented in Chapter 4, all muons are required not to exceed the threshold of 0.15 in a cone of radius  $\Delta R = 0.4$  around the muon. Such isolation requirement is used to further suppress fake muons from decay in flight. Moreover, effects from detector misalignment or errors in the magnetic field might affect the muon momentum. Therefore, a correction is applied to the MC muon momentum in order to incorporate such effects, called the *Rochester correction*.

### 3.3.4. Jets

As pointed out in Section 3.2.2, jets are the experimental signatures of quarks and gluons produced in high-energy processes such as hard scattering of partons in pp collisions. Indeed, partons produced from the pp interactions radiate other partons and form hadrons as a result of the hadronization process,

which then, in turn, can decay into lighter hadrons, leptons or photons. A jet can be therefore seen as a spray of collimated particles. Because of this inherent geometry that characterizes them, jets can be reconstructed by clustering particles together to form a geometrical cone. The cone shape will be, with good approximation, exclusively driven by hard particles, while soft particles have no impact. In CMS, the *anti- $k_t$*  algorithm [78], implemented in the FASTJET package [79], fulfills the purpose of jet clustering.

Jets can be reconstructed in three ways, depending on how the individual contributions from sub-detectors are combined:

- **Calorimeter jets:** they are reconstructed from energy deposits in the calorimeter towers. A calorimeter tower consists of an HCAL tower and the geometrically corresponding ECAL crystals;
- **Jet-Plus-Track jets:** they are reconstructed calorimeter jets with energy response and resolution improved by incorporating tracking information, according to the Jet-Plus-Track algorithm [80];
- **Particle flow jets:** they are reconstructed by clustering the four-momenta of PF candidates. The PF jet momentum and spatial resolutions are greatly improved with respect to calorimeter jets, as the use of the tracking detectors and of the high granularity of ECAL allows the measurement of charged hadrons and photons inside a jet, which together constitute  $\sim 85\%$  of the jet energy [81].

A simulation-based correction (called *jet energy scale* or JES) is applied to the reconstructed jet to account for the bias due to the reconstruction and to remedy an energy offset coming from pileup. Once this correction is applied, generator-level jets are matched to the closest reconstructed jets and a correction factor is extracted in  $p_T$  and  $\eta$  bins. This factor is then applied to modify the momentum of the reconstructed jet. A residual correction is extracted from data using  $\gamma$ +jets events [82].

Moreover, another correction factor is applied to simulated jets to account for the fact that the jet energy resolution (JER) is different for the real and simulated detector. This factor is derived using di-jet events. The derivation of these corrections is impacted by uncertainties which are treated as sources of systematic errors in the statistical analysis presented.

In the analysis presented in Chapter 4, the four-momenta of PF candidates are clustered to form jets by using the *anti- $k_t$*  algorithm with a distance parameter of 0.4, and they are required to be separated from identified leptons by a distance  $\Delta R$  of at least 0.3. Moreover, the simulated jet energies are reweighted by the two correction factors JES and JER, which are then propagated to the missing transverse energy of the event.

## b tagging

The identification of jets originating from heavy-flavor quarks (b or c tagging) is of particular relevance for searches for new physics and for measurements of SM processes. Due to their long lifetime, b hadrons will decay displaced from the primary vertex, giving rise to a distinct feature which is exploited for b tagging. The algorithms used for b tagging rely on three main observables:

- **the impact parameter significance of the track:** the impact parameter (IP) is defined as the distance between the track and the PV at the point of closest approach. It is positive (negative) if the track is produced downstream (upstream) with respect to the PV along the jet direction. Due to the b hadron lifetime, the typical IP scale is set by  $c\tau \sim 480 \mu\text{m}$ . In practice, the impact parameter significance  $\text{IP}/\sigma(\text{IP})$  is used in order to take into account resolution effects. Due to the long lifetime of the b hadrons, the IP from b jets is expected to be mainly positive, while for the light jets it is almost symmetric around zero;
- **the secondary vertex:** due to the high resolution of the CMS tracking system, it is possible to directly reconstruct the secondary vertex. The significance of the 3D flight distance is used as a discriminating variable in some b tagging algorithms;
- **the transverse momentum of the muon:** semi-leptonic decays of b hadrons give rise to b jets that contain a muon with a branching ratio of about 11%, or 20% when  $b \rightarrow c \rightarrow l$  cascade decays are included. This is why the reconstructed muons inside a jet are used to study the performance of the lifetime-based tagging algorithms.

Regardless of what the algorithm used for b tagging is, the output is a discriminator value on which the user can cut to select different regions in the efficiency versus purity. The value of such cut determines the WP of the algorithm, usually classified in *loose*, *medium*, and *tight*, for which the misidentification rate of a light-flavor jet as a b jet is usually 10, 1, and 0.1%, respectively.

The algorithm used for b tagging purposes in the analysis presented in this thesis is called *deepCSV* [84], which is based on the same set of observables used by the older *CSVv2* algorithm [83], with a simple extension to use more charged particle tracks. This algorithm is based on a deep neural network training, with four hidden layers (i.e. six layers altogether) of a width of 100 nodes each. It gives the best b tagging performance when compared to previous algorithms. It is seen that the *deepCSV* algorithms outperform the previous *CSVv2* tagger with an absolute b tagging efficiency improvement of about 4% [84]. Efficiencies and misidentification probabilities for the *deepCSV* tagger for the three different WPs are shown in Fig. 3.10. In this analysis, jets are considered as b tagged if they pass the medium WP of the algorithm, that yields a b-tagging efficiency of  $\sim 70\%$ . Correction factors are applied in

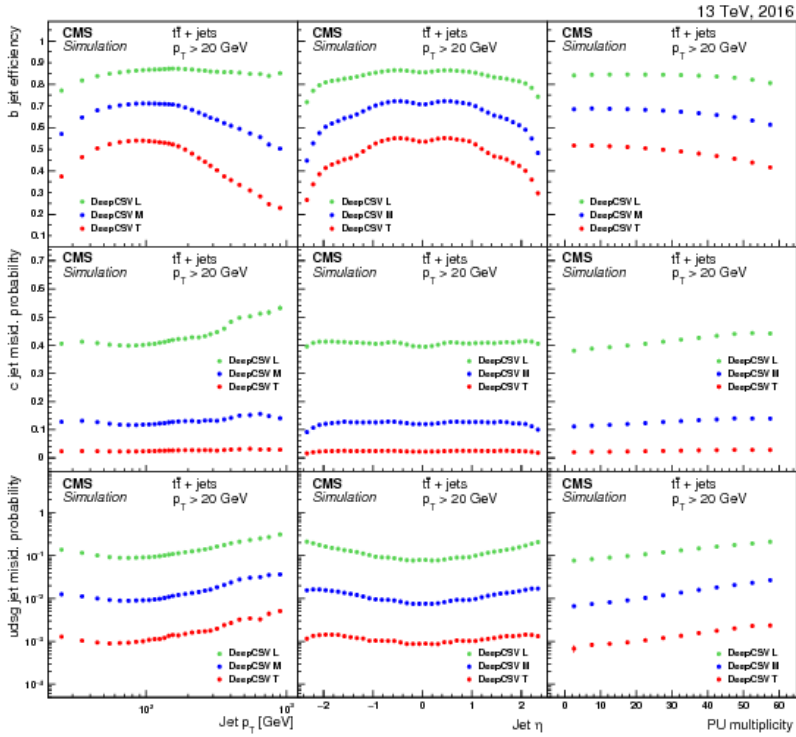


**Figure 3.10.** | Efficiencies and misidentification probabilities for the deepCSV tagger as a function of the jet  $p_T$  (left), jet  $\eta$  (middle), and PU multiplicity (right), for b (upper), c (middle), and light-flavor (lower) jets in  $t\bar{t}$  events. Each panel shows the efficiency for the three different working points with different colors [83].

the simulation to the selected jets to account for the different response of the deepCSV algorithm between data and simulation.

### 3.3.5. Missing transverse energy

The missing transverse energy ( $E_T^{\text{miss}}$ ) is a measurement of the energy imbalance in an event due, for example, to the presence of neutrinos or other weakly interacting neutral particles, or to particles that escape the detector acceptance and therefore are not detected. Since the transverse momentum of the partons inside the colliding protons is null with very good approximation, the sum of the transverse momenta of the final state particles must be zero as well according to the energy-momentum conservation law. However, if a particle is not detected, the following relation holds:

$$\vec{p}_T^{\text{visible}} = \sum_{i \in N_{\text{vis}}} p_T^i \equiv -\vec{p}_T^{\text{miss}} \quad (3.6.)$$

where  $N_{\text{vis}}$  is the number of particles detected and  $\vec{p}_T^{\text{visible}}$  is the sum of their transverse momenta. This allows for the missing transverse energy to be retrieved as follows:

$$E_T^{\text{miss}} = |-\vec{p}_T^{\text{visible}}| \quad (3.7.)$$

In CMS, the  $E_T^{\text{miss}}$  reconstruction is performed by defining the negative vectorial sum over the transverse momenta of all PF particles. A more detailed description of the techniques used for  $E_T^{\text{miss}}$  reconstruction can be found at Ref. [85]. It is important to notice that, in the case of an event with no visible particles in the final state, the  $E_T^{\text{miss}}$  would not be null because of the finite precision of the detector and because of particles that might escape the detector acceptance.

## 3.4. Simulating (new) physics

Predictions of well known physics processes as well as new physics signatures and phenomena is one of the essential components for the realization of a statistical analysis. Simulations are crucial for background modeling as well as for predictions on the number of expected events that, compared to the number observed in data, can give indication about the presence of new physics. Simulated Monte Carlo (MC) samples in CMS are produced in three steps: event generation, simulation of detectors and event reconstruction. The whole simulation chain in CMS is performed within a framework called CMSSW [86], containing several thousands of software lines, including event generators, a GEANT4 [87] simulation of the experiment, and digitization to model the detector's electronics response.

## Event generation

The first step of the simulation procedure is the generation of events at generator level, containing the full matrix element information. In this step, hard scattering processes, parton showering, and hadronization are simulated. In CMSSW, the generation of processes is accomplished with event generators such as MADGRAPH [88] or POWHEG [89], while the parton shower and hadronization are simulated with PYTHIA 8 [90].

## Detector simulation

Once generator-level events are produced, it is crucial to simulate the propagation of the particles throughout the detector, their interactions with its material, and the detector's response, exactly like in real LHC events. A detailed model of the CMS experiment, comprising both the geometry and the materials, is implemented in GEANT4.

First of all, the interactions of all the visible particles with the material of the detector are simulated, and hits are reproduced in the different sub-detectors. In CMS, what has been described so far consists of a single step in the MC generation, called *GEN-SIM*.

Afterwards, the read-out electronics response to the created hits is simulated, in a process called *digitization*. Then, minimum-bias events are superimposed in the so-called *pileup mixing* step to reproduce the presence of pileup in data. The number of minimum-bias events is randomly extracted from a Poisson distribution with mean equal to the expected number of interactions, depending on the total inelastic pp cross section and the luminosity. Trigger effects can be added. Finally, the information from the sub-detectors is combined together to reconstruct the particles. In CMS this is the so-called *DIGI-RECO* step.

The last step needed for the MC samples used in this analysis is the *MiniAOD* step, where the produced DIGI-RECO events are skimmed and reduced in size: information of physics objects can now be directly used for analyses.

Recently, CMS has introduced an additional step: the produced MiniAOD events are further skimmed and reduced in size to create the NanoAOD format. The idea is to have a plain-root sample, which can be analyzed outside any CMSSW environment. The whole production chain is summarized in Fig. 3.11.

## Scale factors

Once the MC simulation is ready, a good agreement between data and simulation must be ensured. To do this, simulation events are rescaled by means of correction factors called *scale factors*. Examples of constant scale factors are the theoretical cross section of the simulated process and the value of the integrated luminosity of the LHC data that one wants to compare the simulation to. In addition to this, the agreement is not always guaranteed to be good due to, for

instance, different reconstruction or trigger efficiencies. Therefore, scale factors are derived to account for this discrepancy by comparing the efficiencies in data and simulation. In CMS, this is commonly done with the *Tag & Probe* method [91]. The derived scale factors are usually binned in  $\eta$  and  $p_T$  regions. If the simulation is performed without knowing exactly the final luminosity of the data sample that one intends to use, the distribution of the mean number of interactions per bunch crossing is only an expected one. This may lead to some disagreement between data and MC simulation. Therefore, once the luminosity is well measured, simulated events are reweighted by comparing the expected and measured distributions of the mean number of interactions. This is called *pileup reweighting* and it is applied to all simulated events used in the analysis presented in this thesis.

The uncertainties associated to scale factors are treated as systematics uncertainties in statistical analyses.

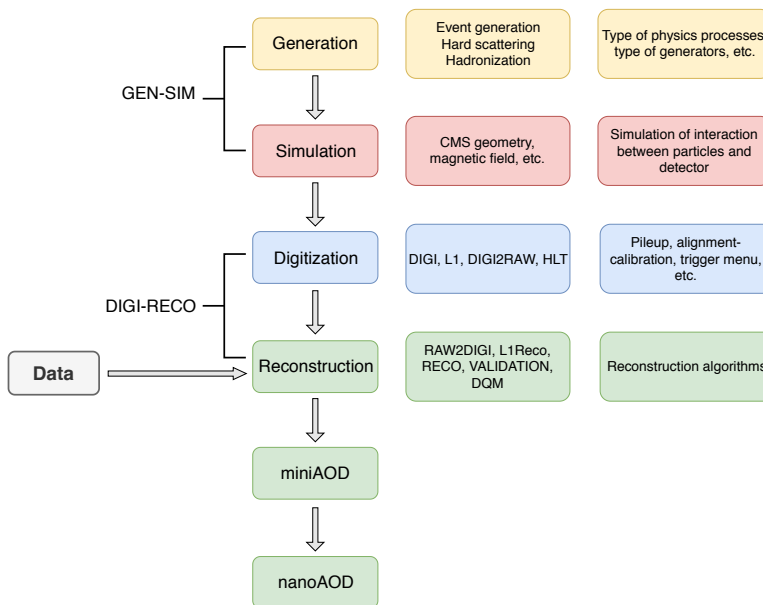


**Figure 3.11.** | MC simulation production chain in CMS. First, in the GEN-SIM step parton-level events are generated and interactions with the detector are simulated. Then, in the DIGI-RECO step digitization and reconstruction are performed. Two output formats can then be extracted: miniAOD and nanoAOD.



# 4.

## Chapter

### **Statistical tools and the MEM for future applications to data analysis**

When searching for a new resonance in experimental data, dedicated statistical methods are required to assess the existence of the particle being searched for. In this chapter, the most important techniques are outlined in Section 4.1. This is not intended to be a comprehensive review of statistics and its methods, which instead can be found at Ref. [92].

Many problems in the analysis of the LHC data are multivariate, since multiple measurements can be performed in an event at once. Therefore, multivariate analysis (MVA) techniques can be used to perform the searches, allowing for extraction of additional information about the hidden structure behind, for instance, a certain event configuration, that one-dimensional analyses are not able to provide. Machine learning techniques and neural networks are nowadays one of the most accredited methods to fulfill this purpose. However, such techniques need training on simulated samples, and their use can be severely limited by the size of the latter. The Matrix Element Method (MEM) [6] is an example of MVA technique through which one can compute the probability that an event is signal-like starting from first principles, and without any training. The MEM is able to provide a direct connection between the underlying physics processes and the detector-level physical observables, resulting in a very powerful technique for signal vs. background discrimination and parameter inference. Section 4.2 is devoted to the description of a case-study that uses the MEM to infer constraints on a Wilson coefficient of the SMEFT (described in Section 2.5) in the top quark sector on a simulation sample. The study is a proof of concept and is intended to investigate the performance of the MEM for measurements in this field, as well as to assess whether it can represent an alternative to traditional techniques, that use measured observables in a simultaneous fit to constrain the Wilson coefficients that they are sensitive to. The results look promising, showing potential for future applicability of this method to constrain coefficients of the SMEFT.

## 4.1. Statistical tools

### 4.1.1. The likelihood function

The correspondence between what we observe experimentally and theoretical predictions is quantified through the definition of a statistical modeling of the data to which statistical procedures are then applied.

The data modeling is defined through probability density functions (pdfs) that represent the probability of observing certain events, and can be parametrized according to some parameters: the parameters that one is interested in, called *parameters of interest* (POIs), and the remaining ones, called *nuisance parameters*, that one must account for even though they are not considered directly related to the physics quantities under study. In the case of the analysis presented in this thesis, the POI is the *signal strength*  $\mu$  of the process being searched for:  $\mu = 0$  indicates absence of signal, while  $\mu = 1$  indicates presence of signal under some theory predictions. The nuisance parameters are instead related to unknown properties of the detector response or of a theory parameter.

In a *cut & count* approach, the number of observed events  $n$  is compared to the number of events predicted by the theory. Events can be counted in one bin only, or in mutually exclusive regions of the phase space (such as different bins in a histogram and/or orthogonal categories of events) that we will refer to as *channels*. This is more general and it is always assumed to be the case in this section.

If the signal and backgrounds are perfectly known, the set of parameters is reduced to only the POI(s). In this case, defining with  $v = \mu s + b$  the number of events predicted by the theory, with  $s$  and  $b$  signal and background counts, respectively, the probability to observe  $n$  events for different values of the statistical parameters, or *likelihood function*, reads:

$$L(n|\mu) = \prod_i Pois(n_i|v_i(\mu)) = \prod_i \frac{v_i(\mu)^{n_i}}{n_i!} e^{-(v_i(\mu))}. \quad (4.1.)$$

However, in realistic measurements many effects that we do not control may influence measurements of POI(s) and bring nuisance parameters into play. In this case, labeling with  $\alpha$  a set of nuisance parameters and with  $a$  their default/measured value, the likelihood reads:

$$L(n, a|v(\mu, \alpha)) = \prod_i Pois(n_i, a_i|v_i(\mu, \alpha)) \prod_p \pi(a_p|\alpha_p). \quad (4.2.)$$

Here, the expected number of events in a channel  $i$  is a function of the nuisance parameters (besides the signal strength), and their uncertainties affect the measured yield. To reduce the impact of these uncertainties, subsidiary measurements on the nuisance parameters can be conducted, so that additional information is obtained and can be encoded in the likelihood function by means

of the constraint terms  $\pi(a_p|\alpha_p)$ .

The functional form for the constraint terms is chosen differently depending on the type of nuisance parameter being considered. For nuisance parameters affecting only the overall normalization of each simulated process (such as the integrated luminosity and the theoretical cross sections) their constraint term is typically a log-normal distribution, centered at the measured value and with a width reflecting the corresponding uncertainty (also called *normalization uncertainty*). The choice of this functional form comes from its property of being positive-definite, so that negative (unphysical) values of these nuisance parameters are never reached, as opposed to a Gaussian distribution.

For nuisance parameters that affect both the shape and the normalization of each process, incorporating the additional information into the likelihood is less trivial since they bring a higher level of complexity: the signal and background yields depend on the value of  $\alpha$ . Therefore, to be able to take their uncertainties into account (also called *shape uncertainties*), one should run the full simulation chain for any arbitrary systematic variation in order to obtain the "response functions"  $s_i(\alpha)$  and  $b_i(\alpha)$  in a channel  $i$ . However, since this is very time consuming, a practical solution is represented by generating the MC simulation samples with a nominal value of the nuisance parameter and then again with the nominal value varied "up" and "down" by a reasonable amount. A renormalization of the constraint term associates the down, nominal, and up templates to the values  $\alpha_p = -1, 0, 1$ , respectively. The response for other values of the nuisance parameter is then approximated by interpolation/extrapolation of the signal and background yields in each channel. In particular, yields are interpolated quadratically for  $\alpha_p$  between -1 and 1, and extrapolated linearly beyond this range. The constraint term on  $\alpha_p$  is usually taken to be a Gaussian with mean zero (i.e. centered at the nominal value) and unit variance.

### 4.1.2. Parameter estimation and confidence intervals

A method often used in statistics to estimate a parameter  $\theta$  of a distribution is, for a set  $X$  of  $n$  observations, to maximize the likelihood function with respect to  $\theta$ :

$$\frac{\partial L(X|\theta)}{\partial \theta} = 0. \quad (4.3.)$$

The value  $\hat{\theta}$  that solves this equation is called *maximum likelihood estimator* (MLE). It is common practice to minimize the function  $-\ln L(X|\theta)$ , called *negative log-likelihood*, which is equivalent to maximizing the likelihood, given that the logarithm of  $L$  is a monotonic function of  $L$ .

For a large number of observations (asymptotic condition), the MLE is: unbiased (its expectation value agrees with its true value), consistent (it tends to its true value), and normal-distributed around its true value. This implies that as  $n$

grows, the log-likelihood approaches a quadratic function (i.e. a parabola) centered at the MLE. The latter point forms the basis for constructing asymptotic confidence intervals (CIs) for the unknown parameter. A practical way to set  $1\sigma$  and  $2\sigma$  CIs around the MLE is to intersect the parabola defined by the negative log-likelihood at 0.5 and 2, respectively, provided that a constant term has been subtracted in order to bring the minimum of the parabola at zero. Indeed, it is easily shown that these values correspond to a  $1\sigma$  and  $2\sigma$  interval in a Normal distribution. In a frequentist approach, setting a  $1\sigma$  ( $2\sigma$ ) CI means that, when computing the intervals for many independent repetitions of the experiment, about 68% (95%) of them contains the true value of the parameter being estimated.

### 4.1.3. Hypothesis test and p-value

The search for new physics is carried out through a statistical procedure where two hypotheses are compared: the *null hypothesis*  $H_0$ , that assumes the absence of the signal, and the *alternative hypothesis*  $H_1$ , that assumes the presence of the signal. The claim of discovery is a statement that the data are incompatible with the null hypothesis.

If  $H_0$  and  $H_1$  are two simple hypotheses, the Neyman-Pearson lemma [93] states that the statistical power of rejecting  $H_0$  in favor of  $H_1$  is maximized by the ratio of the two corresponding likelihoods. In the case where subsidiary measurements are performed, one uses the *profile log-likelihood ratio*:

$$q_\mu = \begin{cases} -2 \ln \frac{L(n,a|\mu,\hat{\nu}(\mu;\alpha))}{L(n,a|\nu(\hat{\mu},\hat{\alpha}))} & \hat{\mu} \geq 0, \\ 0 & \hat{\mu} < 0 \end{cases} \quad (4.4.)$$

where  $\hat{\mu}$  and  $\hat{\alpha}$  represent the MLE of the parameters  $\mu$  and  $\alpha$ , respectively, while  $\hat{\nu}(\mu;\alpha)$  is  $\nu$  computed for the value of  $\alpha$  that maximizes the likelihood and  $\mu$  fixed. The null and alternative hypotheses are defined for  $\mu = 0$  and  $\mu = 1$ , respectively.

The profile likelihood ratio is an example of a *test statistic*, a real-valued function that summarizes the data in a way relevant to the hypotheses that are being tested. Probability density functions of this test statistic  $f(q_\mu)$  can be built by sampling  $n$  from a Poisson distribution under, for instance, the null and alternative hypotheses. Once inputting the observed number of events, the profile likelihood ratio is a single number  $q_{obs}$  that quantifies the entire experiment and represents a proxy to establish the degree to which the data are unexpected for a given hypothesis, the p-value. This is defined as:

$$p = \int_{q_{obs}}^{\infty} f(q_\mu|H_0) dq_\mu . \quad (4.5.)$$

A graphical representation is shown in Fig. 4.1. The null hypothesis is rejected if the p-value is found to be less or equal to a threshold that is chosen to be 0.05. More in general, if the p-value for a given hypothesis is less or equal to 0.05, the hypothesis is rejected at 95% confidence level (CL).

Depending on their nature, statistical tests can be one-sided or two-sided. In the first case, the critical value of 0.05 is allotted in one tail of the distribution, while in the second case the value is split in half, with each half allotted in each of the two tails of the distribution. When performing a measurement, any deviation above or below the expected value might serve an indication of some anomaly or new physics, hence a two-sided test is needed. However, when looking for new resonances, one has an assumption about the "direction" of the effect: if only an excess of events is significant to claim new physics, but not a deficit, then the one-sided represents the suitable test.

The p-value can be converted in *significance*  $\sigma$  through the relation  $\sigma = \Phi^{-1}(1 - p)$ , where  $\Phi$  is the Gaussian cumulative distribution function. The result of a hypothesis test comparing the null against the alternative hypothesis assuming a new particle with  $\sigma \geq 3$  is called an *evidence* of this new particle, while for  $\sigma \geq 5$  the *observation* can be claimed.

#### 4.1.4. Upper limits and $CL_s$ method

A common procedure when looking for new physics is to set *upper limits* bounding the value of the signal strength determining the observed data at hand. A slightly different test statistic from the one in Eq. 4.4 is used for this purpose:

$$q_\mu = \begin{cases} -2 \ln \frac{L(n,a|\mu,\hat{v}(\mu;\alpha))}{L(n,a|v(0,\hat{\alpha}))} & \hat{\mu} < 0, \\ -2 \ln \frac{L(n,a|\mu,\hat{v}(\mu;\alpha))}{L(n,a|v(\hat{\mu},\hat{\alpha}))} & 0 < \hat{\mu} < \mu, \\ 0 & \hat{\mu} > \mu \end{cases} \quad (4.6.)$$

Again, one can build pdfs of this test statistic under the null and alternative hypotheses. Varying  $\mu$  in the test statistic in Eq. 4.6 under the alternative hypothesis, the *upper limit* at 95% CL is the value of  $\mu$  that satisfies:

$$p_\mu = \int_{q_{obs}}^{\infty} f(q_\mu|H_1) dq_\mu = 0.05. \quad (4.7.)$$

*Expected* upper limits on the signal strength are also usually derived. This is done by computing the median  $q_{med,\mu}$  of the distribution of the test statistic in Eq. 4.6 under the assumption of no signal, and extracting the associated upper limit  $\mu_{exp}$  similarly to Eq. 4.7. Error bands on  $\mu_{exp}$  at  $1\sigma$  and  $2\sigma$  can also be determined, indicating that in a high number of samples these intervals contain the value  $\mu_{exp}$  68% and 95% of the times, respectively.

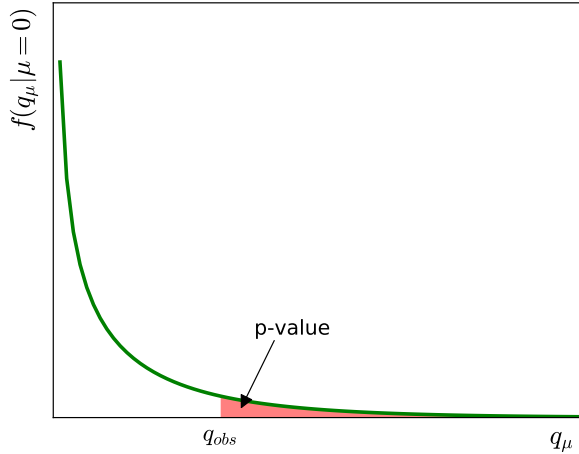


**Figure 4.1.** | Probability density function of test statistic  $q_\mu$  under the null hypothesis. The p-value is represented by the red area.

In experiments with little sensitivity, the pdfs  $f(q_\mu|H_0)$  and  $f(q_\mu|H_1)$  may overlap significantly. This introduces a probability that the upper limit derived on  $\mu$  might be very low if the data happen to fluctuate downwards compared to the background-only expectation. To protect from this, a modification to the p-value is introduced through the *CL<sub>s</sub> method* [94]. Indicating with  $p_\mu$  the p-value derived when testing a hypothesis with a signal strength  $\mu$ , and with  $p_b$  the p-value derived when testing the background-only hypothesis, the p-value used to determine whether the signal hypothesis can be rejected reads:

$$CL_s(\mu) = \frac{p_\mu}{1 - p_b} . \quad (4.8.)$$

The signal hypothesis is rejected at 95% CL when  $CL_s(\mu) \leq 0.05$ . Moreover, by solving this for  $CL_s(\mu) = 0.05$  with respect to  $\mu$ , upper limits on  $\mu$  at 95% CL can be set. This is known as the *CL<sub>s</sub> method*.

A schematic visualization is shown in Fig. 4.2. Here,  $p_\mu$  is the p-value derived when testing a signal hypothesis with  $\mu = 1$  and is referred to as  $p_{s+b}$ . If  $p_{s+b}$  is below a certain rejection threshold (for instance 0.05), the signal would be rejected even though there is zero or little sensitivity to it. By applying the correction from Eq. 4.8, the big value of  $p_b$  acts as a penalty on  $p_{s+b}$ : if  $p_b$  is sufficiently large, it is possible for  $CL_s(\mu)$  to "jump" above the rejection threshold, thus making it not possible to reject the signal-plus-background hypothesis anymore.

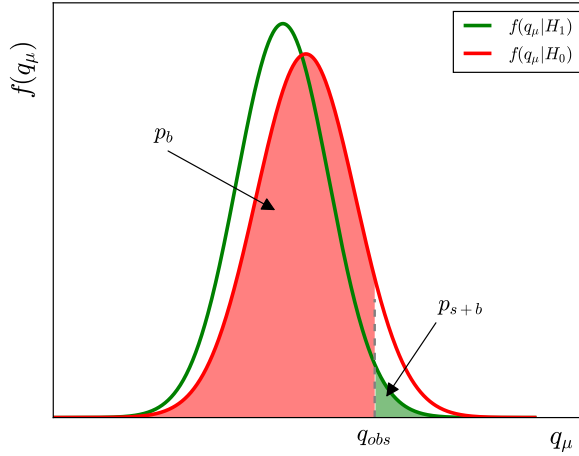


**Figure 4.2.** | Probability density functions of the test statistic  $q_\mu$  under the null hypothesis (red curve) and the alternative hypothesis (green curve). The p-value  $p_{s+b}$  derived when testing  $H_1$  is represented by the red area, while  $p_b$  represents the p-value derived when testing  $H_0$ .

### 4.1.5. The look-elsewhere effect

**One-dimensional case.** When evaluating the significance of an excess of events, one must be careful in accounting for the probability that the observation may have actually arisen by chance because of the size of the parameter space being searched in. This is called *look-elsewhere effect* (LEE) [95]. In practice, when looking for an excess of events compatible with the hypothesis of a new particle, one has to probe a large region of the parameter space because it is not known beforehand where the signal might appear. This causes a "probability boost" of observing some excess of events, because of the many regions being probed instead of an *a priori* defined one. Therefore, the observed p-value, called *local p-value*, must be transformed into a *global* one through the probability of observing an excess *anywhere* in the search region. This can be done as follows. When searching for a new particle, some nuisance parameters are defined only under the alternative hypothesis and not under the null, given that no particle is foreseen under the latter. An example of such nuisance parameter is the mass of the particle. The test statistic defined in Eq. 4.4 under the background only hypothesis reads, in a simplified notation [96]:

$$q_0(m) = \begin{cases} -2 \ln \frac{L(0, \hat{\mu})}{L(\hat{\mu}, m)} & \hat{\mu} \geq 0, \\ 0 & \hat{\mu} < 0 \end{cases} \quad (4.9.)$$

where  $m$  is the mass of the new particle. Given some data set, one finds the value  $\hat{m}$  that maximizes  $q_0(m)$  for all possible masses. For a high observed local significance  $Z$ , the following relation holds:

$$\mathbb{P}[q_0(\hat{m}) > u] \approx \frac{1}{2}\mathbb{P}[\chi_1^2 > u] + N\mathbb{P}[\chi_2^2 > u], \quad (4.10.)$$

where  $u = Z^2$ ,  $N$  is the number of independent search regions, and  $\chi_i^2$  the chi-square distribution with  $i$  degrees of freedom.  $N$  is found by estimating the average number of upcrossings of the test statistic in Eq. 4.9 at level  $u$ , i.e.  $\mathbb{E}(n_u) = Ne^{-u/2}$ . However, since the level  $u$  is rather high, the number of upcrossings is relatively low, yielding a high statistical error. Therefore, one can pick a lower level  $u_0$  where the number of upcrossings is high, and in this case  $\mathbb{E}(n_{u_0}) = Ne^{-u_0/2}$ . This can be obtained by computing the average number of upcrossings through toys. It is straightforward to see that:

$$\mathbb{E}[n_u] = \mathbb{E}[n_{u_0}]e^{(u-u_0)/2} \quad (4.11.)$$

through which one can estimate the average number of upcrossings. The local p-value can now be corrected through the relation:

$$p_{global}(u) \approx p_{local}(u) + \mathbb{E}[n_{u_0}]e^{(u-u_0)/2}. \quad (4.12.)$$

The ratio between global and local p-value is called *trial factor* [95,96].

A practical example can be found in the Higgs boson discovery [1, 2]. Figure 4.3 [97] shows the local p-value  $p_0$  as a function of the Higgs mass. The upcrossings are counted at a threshold  $u_0$  corresponding to  $0\sigma$  (equivalently  $p_0 = 0.5$ ), and it is found:  $n_{u_0} = 9 \pm 3$ . With an observed significance of  $5\sigma$ , from Eq. 4.12 it is possible to extract the global p-value:

$$p_{global} = O(10^{-7}) + 9 \times e^{-25/2} = 3.3 \times 10^{-5} \quad (4.13.)$$

with a trial factor  $t \approx \frac{10^{-5}}{10^{-7}} \approx 100$ , reducing the significance from  $5\sigma$  to  $4\sigma$ .

**Two-dimensional case.** When the alternative hypothesis encodes more than one parameter, the estimation of the LEE becomes a multi-dimensional problem. The procedure described in one dimension can be generalized, for a two-dimensional (2D) case, as follows.

It can be shown that in two dimensions, under the assumption that the two theoretical parameters are independent of each other, the global and local p-value are linked by the following relation [98], similarly to Eq. 4.12:

$$p_{global}(u) \approx p_{local}(u) + \mathbb{E}[n_{u_0}]e^{-\frac{u}{2}}(N_1 + N_2\sqrt{u}) \quad (4.14.)$$

where  $u = Z^2$ , with  $Z$  being the maximum local significance observed, and  $N_1$  and  $N_2$  are coefficients that need to be estimated.

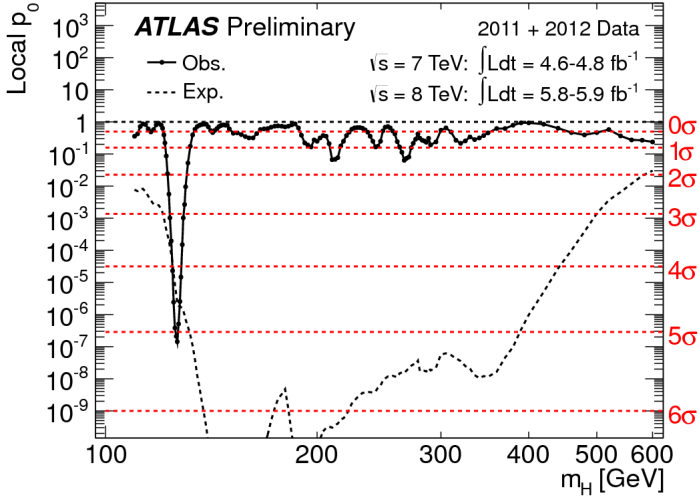


**Figure 4.3.** | The local probability  $p_0$  for a background-only experiment to be more signal-like than the observation in the full mass range as a function of  $m_h$ . The horizontal dashed lines indicate the p-values corresponding to significances of  $1\sigma$  to  $6\sigma$  [97].

These coefficients are found by solving the following system of equations:

$$\begin{cases} \mathbb{E}[\phi(A_{u_0})] = \mathbb{P}[\chi_1^2 > u_0] + e^{u_0/2}(N_1 + N_2 \sqrt{u_0}) \\ \mathbb{E}[\phi(A_{u_1})] = \mathbb{P}[\chi_1^2 > u_1] + e^{u_1/2}(N_1 + N_2 \sqrt{u_1}) \end{cases} \quad (4.15.)$$

where  $u_0$  and  $u_1$  are two arbitrarily chosen thresholds and  $\mathbb{E}[\phi(A_{u_0})]$  ( $\mathbb{E}[\phi(A_{u_1})]$ ) is the average Euler characteristic of the 2D mass parameter space, indicated with  $A$ , at threshold  $u_0$  ( $u_1$ ). In a 2D manifold with closed islands, some with holes, the Euler characteristic  $\phi$  is obtained as follows: each disconnected full island contributes with the value  $+1$ , while each hole contributes with  $-1$ . This is shown, for illustration purposes only, in Fig. 4.4, where one island gives  $\phi = 1$ , one island with a hole inside  $\phi = 0$ , and two disconnected islands  $\phi = 2$ . Obtaining the Euler characteristic can be seen as a generalization of counting the number of upcrossings in the one-dimensional case. The expectation values  $\mathbb{E}[\phi(A_{u_0})]$  and  $\mathbb{E}[\phi(A_{u_1})]$  are obtained with toys, similarly to the one-dimensional case. This allows for the solution of the system in Eq. 4.15 for  $N_1$  and  $N_2$ . Then, one can finally calculate  $p_{global}$  from Eq. 4.14.

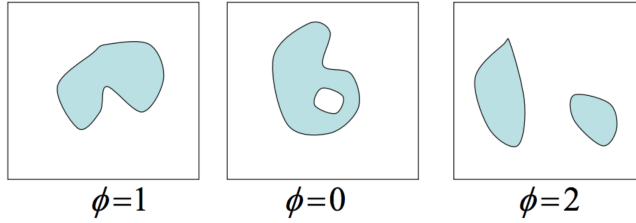


**Figure 4.4.** | Illustration of the Euler characteristic of some two-dimensional manifold [98].

## 4.2. Statistical inference with the MEM: a case-study

It was pointed out in Section 4.1 that a method often used in statistics to perform inference of an unknown parameter is to minimize the negative log-likelihood function with respect to the parameter itself. In this section, this method is used to get an estimate of the degree of freedom  $c_{Qq}^{11}$  of the SMEFT on a top quark pair production ( $t\bar{t}$ ) MC simulation sample in the fully-leptonic final state. The event-by-event likelihoods are estimated with the MEM using MoMEMta [7], a modular toolkit for the MEM that I contributed to develop. A brief overview of the  $c_{Qq}^{11}$  coefficient and the MEM is given. The MoMEMta software is also presented, where the main issues in numerical integration are tackled, together with a description of how the fully-leptonic  $t\bar{t}$  process is configured in MoMEMta to get the event-by-event likelihoods. Then, results are presented and discussed.

### 4.2.1. The $c_{Qq}^{11}$ degree of freedom

Considering only the dimension-6 operators in Eq 2.14, of particular interest is the top quark sector, which provides 34 independent operators in the Warsaw basis [99]. These comprise 11 four-heavy-quark operators, 14 two-heavy-two-light quark operators, and 9 operators involving two heavy quarks and bosonic fields. Linear combinations of these coefficients are usually considered, that are aligned with physically relevant directions of the SMEFT parameter space [5], and are referred to a *degrees of freedom* (d.o.f.). In particular, the d.o.f.  $c_{Qq}^{11}$  is a linear combination of three of the two-heavy-two-light quark operators and the quantity  $c_{Qq}^{11}/\Lambda^2$  is measured in this work on a SM simulation sample. The  $t\bar{t}$  process provides high sensitivity to this degree of freedom: the presence of this operator affects the coupling between the top quarks and the light quark-antiquark pair of the initial state, as shown in Fig. 4.5.

To investigate the effect of a non-null  $c_{Qq}^{11}$  d.o.f. in the SMEFT framework on kinematic distributions of particles of interest, a fully-leptonic  $t\bar{t}$  simulation sample was produced with MADGRAPH5\_aMC@NLO version 2.6.5 [88] in the di-muon final state at LO in QCD precision and with corrections up to  $1/\Lambda^2$  at the amplitude level. The quantity  $\Lambda$  is set to 1 TeV. Figure 4.6 shows the

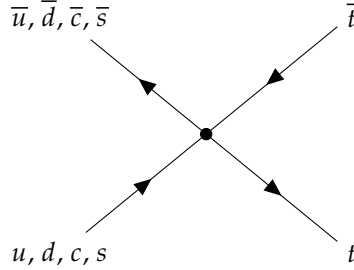


**Figure 4.5.** | Example of  $t\bar{t}$  process production at LO, where the vertex between the quark-antiquark pair and the top pair is described by a dimension-6 effective operator.

$p_T$  distributions of the top and b quarks and the muons together with their corresponding antiparticles in the two cases  $c_{Qq}^{11} = 0$  (SM-like) and  $c_{Qq}^{11} = 1$  at generator level (that is, no parton shower, hadronization, or detector effect is accounted for). The effect of a non-null  $c_{Qq}^{11}$  can be mainly noticed in the tails: the distribution generated with  $c_{Qq}^{11} = 1$  exhibits a less steep spectrum with respect to the SM case. In other words, this SMEFT benchmark shows a tendency to favor more energetic particles.

The current 95% confidence level bounds on this coefficient from direct analysis of top quark production are  $[-3.1, 3.2]$  in units of  $\text{TeV}^{-2}$ , assuming  $\Lambda = 1 \text{ TeV}$ , extracted from a global fit [100]. Without marginalization of all the coefficients, the single-operator bounds (obtained by setting all coefficients to 0 except  $c_{Qq}^{11}$ ) are  $[-0.2, 0.02]$  [5]. Such a difference in the bounds lies in the fact that within the single-operator fits one is neglecting the cross-correlations between the different directions spanned by the fitted degrees of freedom.

## 4.2.2. The Matrix Element Method

The Matrix Element Method is a technique to calculate the conditional probability density  $P(x|\alpha)$  to observe an experimental event  $x$ , given a specific theoretical hypothesis  $\alpha$ . Details can be found at Ref. [101], while a brief review is given below.

Indicating with  $y$  a partonic final state, the probability  $P(x|\alpha)$  is given by:

$$P(x|\alpha) = \frac{1}{\sigma_\alpha} \int d\sigma_\alpha(y) T(x|y), \quad (4.16.)$$

where  $\sigma_\alpha$  is the cross section of the process under the theoretical hypothesis  $\alpha$ , that can be estimated from a simulated sample. The term  $d\sigma_\alpha(y)$  represents the differential cross section in hadron collisions, while  $T(x|y)$  indicates the *transfer functions*. These two terms are described in detail below.

The above-mentioned  $d\sigma_\alpha(y)$  is the convolution of the differential cross section corresponding to the hard-scattering process  $d\sigma_\alpha(q_1, q_2, y)$ , with  $q_1$  and  $q_2$

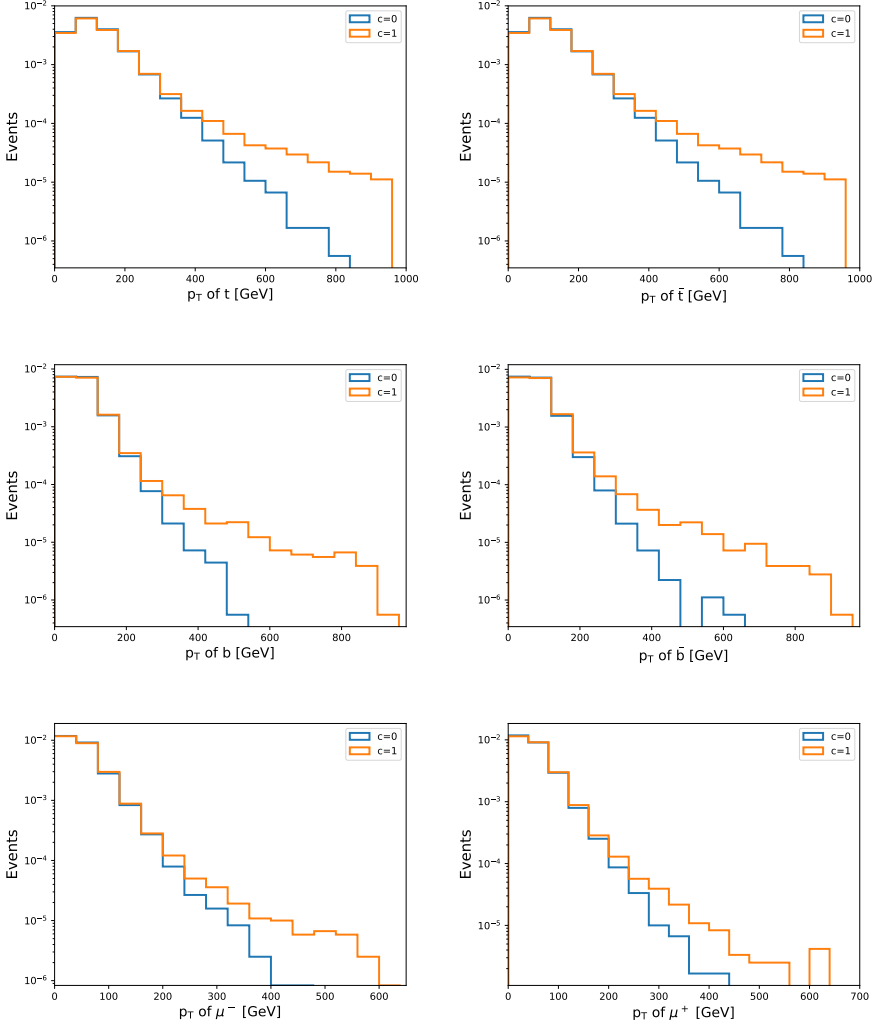


**Figure 4.6.** | Distribution of the generator-level  $p_T$  of some of the particles in a fully-leptonic  $t\bar{t}$  simulation sample in the di-muon final state for  $c_{Qq}^{11} = 0$  (SM-like) in blue and  $c_{Qq}^{11} = 1$  in orange. On the left the distributions for the top (upper), bottom (middle) quark and the muon (lower) are shown, with the corresponding antiparticles shown on the right.

fractions of the initial state parton momentum, and of the parton distribution functions  $f_{a_1}(q_1)$  and  $f_{a_2}(q_2)$  for a given flavor  $a_i$  and momentum fraction  $q_i$ , summed over all possible flavor compositions of the colliding partons. Mathematically, it reads:

$$d\sigma_\alpha(y) = \int \sum_{a_1, a_2} dq_1 dq_2 f_{a_1}(q_1) f_{a_2}(q_2) d\sigma_\alpha(q_1, q_2, y). \quad (4.17.)$$

The differential cross section  $d\sigma_\alpha(q_1, q_2, y)$  can be considered the "core" element of the MEM, since it encodes the theoretical assumptions through the squared matrix element  $\mathcal{M}$  of the process under study:

$$d\sigma_\alpha(q_1, q_2, y) = \frac{|\mathcal{M}_\alpha(q_1, q_2, y)|^2}{q_1 q_2 s} d\Phi(y). \quad (4.18.)$$

Here,  $s$  represents the squared center-of-mass energy of the colliding hadrons, while  $\Phi(y)$  is the differential partonic phase space of the final state and it can be defined as, for an  $n$ -particle final state:

$$d\Phi(y) = (2\pi)^4 \delta^4(P_{in} - P_{fin}) \prod_{i=1}^n \frac{d^3 p_i}{(2\pi)^3 2E_i}, \quad (4.19.)$$

where  $p_i$  represents the three-vector component of the particle labeled with  $i$  and the  $\delta^4(P_{in} - P_{fin})$  ensures the energy-momentum conservation.

The transfer functions  $T(x|y)$  can be interpreted as "response functions" encoding the detector reconstruction effects. Normalized as probability densities over  $x$ , they provide the probability to reconstruct the event  $x$  in the detector provided that the hard process led to the partonic configuration  $y$ .

In view of this, Eq. 4.16 can be then explicitly written as follows:

$$P(x|\alpha) = \frac{1}{\sigma_\alpha} \int \sum_{a_1, a_2} \int dq_1 dq_2 f_{a_1}(q_1) f_{a_2}(q_2) \frac{|\mathcal{M}_\alpha(q_1, q_2, y)|^2}{q_1 q_2 s} T(x|y) d\Phi(y), \quad (4.20.)$$

The bare integral without the normalization factor  $\sigma_\alpha$  is referred to as *matrix element weight*  $w(x|a)$ . The ME weight thus quantifies the agreement between the theoretical process  $\alpha$  and the experimental event  $x$ : the higher  $w(x|a)$ , the more likely to observe the reconstructed event  $x$  provided that the hypothesis  $\alpha$  is true.

### 4.2.3. Configuring the process with MoMEMta

In order to compute the ME weight, one has to compute the integral in Eq. 4.20. The structure of the integrand is generally non-trivial, as it may contain localized peaks arising from resonances in the matrix element or from the transfer functions when the partonic configuration  $y$  gets kinematically close to the

reconstructed event  $x$ . This makes the numerical integration extremely challenging. Indeed, many numerical integration algorithms try to optimize the integration grid in order to focus the integration in regions of the phase space where the density is higher, that is, where the integrand peaks are. However, if the peaks in the multi-dimensional domain are too narrow, they might just be overlooked with the unintended result of not being integrated over. A solution to this problem was implemented in `MadWeight` [102], where suitable changes of variables are designed to remove as much as possible the peaks in the integrand, simplifying the integration process. However, the `MadWeight` implementation shows lack of flexibility and is not supported anymore. The `MoMEMta` toolkit [7], a modular C++ software package to compute the convolution integrals for the MEM, is used instead.

In `MoMEMta`, a software that I contributed to develop, the computation of the ME weights occurs via *modules* specifically designed for various purposes. Examples are the matrix element module and the transfer function modules that evaluate, respectively, the matrix element of the process and the chosen transfer functions, modules to perform the change of variables, and a module to handle the combinatorics of the final state. Moreover, the matrix element can be exported by the user from any generator (e.g. `MadGraph`) and plugged in `MoMEMta`. The user can "assemble" these modules into a configuration file in the Lua scripting language according to their needs. In order to provide a practical example, a description of how the change of variables works for the fully-leptonic  $t\bar{t}$ , together with the `MoMEMta` modules and parameters used for the computation of its associated weights is given. This then allows for extraction of the ME weights, used to build the likelihood function and therefore to infer constraints on the  $c_{Qq}^{11}$  coefficient.

The fully-leptonic  $t\bar{t}$  process exhibits six particles in its final state: two leptons and two b jets (that we are able to detect in our experiment), and two neutrinos (that instead escape observation). This can be seen in Fig. 4.7, where  $p_1$  and  $p_2$  represent the four-momenta of the two neutrinos, indicated with bold lines,  $p_4$  and  $p_6$  indicate the four-momenta of the two b jets, and  $p_3$  and  $p_5$  those of the two leptons. Thus, 20 d.o.f. characterize this process: the energy and the two directions of all final-state particles ( $3 \times 6$ ) and the longitudinal momentum of the initial-state partons (2). At this stage, the standard phase space parametrization together with the parton momentum fractions reads:

$$dq_1 dq_2 (2\pi)^4 \delta^4(P_{in} - P_{fin}) \prod_{i=1}^6 \frac{d^3 p_i}{(2\pi)^3 2E_i}. \quad (4.21.)$$

By integrating out the  $\delta^4(P_{in} - P_{fin})$ , 4 d.o.f are removed. Assuming that the directions of the visible particles are perfectly reconstructed, that is, their

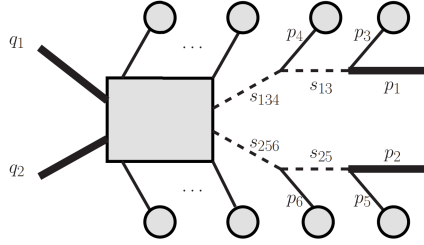


**Figure 4.7.** | Schematic view of fully-leptonic  $t\bar{t}$  process production. The neutrinos are indicated with bold lines. The four-momenta of the two neutrinos are indicated with  $p_1$  and  $p_2$ , those of the jets with  $p_4$  and  $p_6$ , and those of the leptons with  $p_3$  and  $p_5$  [102].

transfer functions are Dirac deltas, we are left with 8 d.o.f. to integrate over, since this assumption removes 2 d.o.f. for each of the 4 visible particles. Here, the peaks in the multi-dimensional domain arise from the Breit-Wigner resonances in the matrix element associated to the top quarks and the  $W$  bosons, from the parton distribution functions, and from the transfer functions on the energies of the visible particles  $T(E_i^{reco} | E_i)$ . However, each of the four transfer functions is a function of the integration variable  $E_i$ . This means that their peaks are already aligned with the corresponding integration grid, while this is not the case for the Breit-Wigner peaks. Moreover, the neutrinos are not constrained by any transfer function, and removing these variables from the integrand parameterization can improve significantly the numerical convergence. A change of variables is then performed by removing four d.o.f. in favor of the squared invariant masses of the top quarks ( $s_{134}, s_{256}$ ) and of the  $W$  bosons ( $s_{13}, s_{25}$ ). The new parametrization of the phase-space is proportional to:

$$ds_{134}, ds_{256}, ds_{13}, ds_{25} \times \text{Jacobian} , \quad (4.22.)$$

and the Jacobian associated to this change of variable is automatically evaluated by the MoMEMta software for each integration point. In this way, the integration grid is now aligned with the peaks from the matrix element, improving the convergence of the integral. For the work presented in this chapter, an additional dimension of integration is introduced in order to handle the combinatorial ambiguity in the assignment between reconstructed final-state  $b$  jets and  $b$  quarks in the matrix element. The integration is performed with the VEGAS [103] algorithm implemented in the CUBA [104] library with a number of phase space points used for the integration of 25 million. The transfer functions on the energies of the visible particles are parametrized with a Gaussian distribution with a std. dev. of 5% for the leptons and 10% for the jets is chosen, in order to reflect the lower detector resolution for hadronic objects in high-energy physics experiments.

#### 4.2.4. Results

It is essential to underline here that the integral defined in Eq. 4.20 is typically a small number that varies over several orders of magnitudes from event to event, and it is therefore common to use instead the quantity  $I = -\ln P(x|\alpha)$ . For more than one event, one considers the quantity  $J = -\sum_{events} \ln P(x|\alpha)$ . In order to estimate a parameter of interest, it is necessary to run the MEM under several different theoretical hypotheses. In the case of this work, this corresponds to running MoMEMta under several different values of  $c_{Qq}^{11}$ , called  $c$  in the following for shortness. This provides a scan of the quantity  $J$  over this parameter, and its minimum corresponds to the MLE of its true value.

The contribution of the SMEFT term to the matrix element of the process can be broken down into three parts: a SM contribution; a quadratic contribution from the dimension-6 operator only; and an interference term between the two. Indicating with  $c$  the parameter to be estimated, this translates into:

$$|\mathcal{M}_{SMEFT}|^2 = |\mathcal{M}_{SM} + c\mathcal{M}_{NP}|^2 = A_{SM} + cA_{int} + c^2A_{quad}. \quad (4.23.)$$

The integral in Eq. 4.20 can be then written, for a given  $c$ , as the sum of three separate integrals:

$$P(x|c) = \frac{1}{\sigma_c} \left( w_{SM} + cw_{int} + c^2w_{quad} \right). \quad (4.24.)$$

The same applies to the cross section for a given  $c$ :

$$\sigma_c = \sigma_{SM} + c\sigma_{int} + c^2\sigma_{quad}. \quad (4.25.)$$

To obtain  $P(x|c)$ , one would then have to run MoMEMta with the three different matrix elements in Eq 4.23 (i.e. three times only) and then use Eq. 4.24. However, exporting the interference matrix element from MADGRAPH5\_mC@NLO in a format suitable for MoMEMta is not yet possible. This obstacle is worked around with the following parametrization:

$$\begin{aligned} w_{SM} &= w(x|c=0), \\ w_{int} &= \frac{w(x|c=1) - w(x|c=-1)}{2}, \\ w_{quad} &= \frac{w(x|c=1) + w(x|c=-1)}{2} - w(x|c=0) \end{aligned} \quad (4.26.)$$

This implies that MoMEMta can be run with one matrix element only ( $|\mathcal{M}_{SMEFT}|^2$ ) and with three different values used for the desired parametrization (in this case  $c=0,1,-1$ ). Then, one can compute  $P(x|c)$  in Eq. 4.24 for any desired value of the parameter. The likelihood scan over  $c$  can therefore be performed with arbitrary resolution.

The simulation sample described in Section 4.2.1 contains 100,000 events at generator level, and they are used to study the behavior of the MLE without shower

and detector effects. The same events are then showered with PYTHIA 8.212 [90] and the simulation of particles interactions with the CMS detector is performed with DELPHES 3.4.1 [105]. These events are then reconstructed and we will refer to them as reconstruction-level events.

#### 4.2.4.1. MLE at generator-level

At generator level, one has access to the partonic kinematics of the six final-state particles of the  $t\bar{t}$  process. Given that no detector effect is present, the transfer functions on the visible particles mentioned in Section 4.2.2 are Dirac deltas in both the energy and directions. Moreover, the information about neutrinos and the presence of the  $\delta^4$  to ensure energy-momentum conservation removes all the remaining d.o.f. from the system, making it over-constrained, that is, with no d.o.f. left as integration variables. The evaluation of  $P(x|c)$  is then reduced to a mere evaluation of its integrand.

The results are shown in Fig. 4.8 in terms of  $c/\Lambda^2$ . As expected from the properties of the MLE, the parabolas' widths get narrower the more events are used to build the log-likelihood. For 100,000 events, the estimated value is given in Table 4.1 together with the  $1\sigma$  and  $2\sigma$  confidence intervals, showing consistency with the true value  $\frac{c}{\Lambda^2_{true}} = 0$ .

It can be noticed that Fig. 4.8 exhibits a strange feature when the number of events is 500: two minima are there instead of one, away from the true value where instead lies a maximum. This feature is explained below.

Since the simulation sample used for this study is SM-like, the MEM should in principle output weights that, once normalized to the corresponding cross sections, are higher for  $c = 0$  than for  $c \neq 0$ . However, it is statistically possible for some SM-like events to be generated in a kinematic configuration that looks more likely to come from a BSM scenario. The double minima structure visible in Fig. 4.8 is caused by one event only, where one of the particles is generated with very high momentum, thus favoring the  $c \neq 0$  scenario. This can be seen in Fig. 4.9, where the generated  $p_T$  values of the b quarks and muons of the event yielding two minima are indicated with a black arrow on their corresponding distributions (shown in Fig. 4.6). The  $p_T$  of the b quark lies at

**Table 4.1.** † Maximum likelihood estimator  $\frac{\hat{c}}{\Lambda^2}$  with the corresponding  $1\sigma$  and  $2\sigma$  confidence intervals for 100,000 generator-level events. The true value is also displayed for reference.

$\frac{c}{\Lambda^2_{true}} [\text{TeV}^{-2}]$	$\frac{\hat{c}}{\Lambda^2} [\text{TeV}^{-2}]$	$1\sigma \text{ CI} [\text{TeV}^{-2}]$	$2\sigma \text{ CI} [\text{TeV}^{-2}]$
0	-0.017	[-0.038,0.005]	[-0.06,0.027]

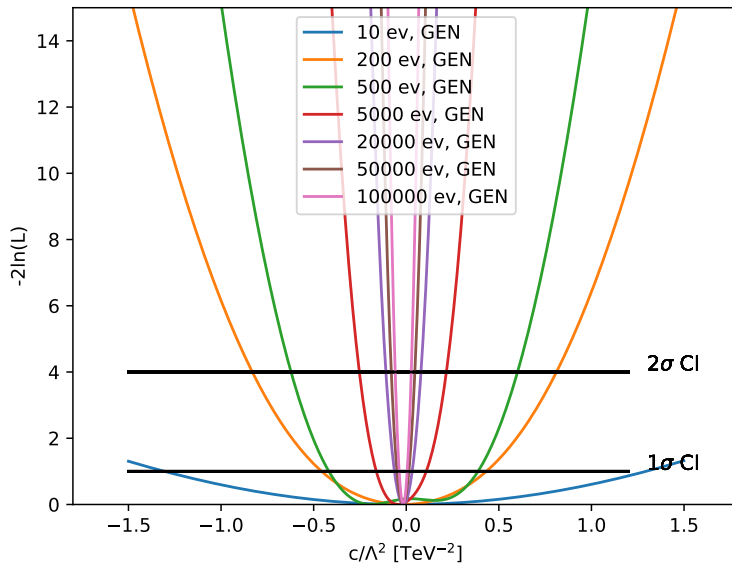


**Figure 4.8.** | Negative log-likelihood as a function of  $c/\Lambda^2$  on generator-level events. The different colors indicate the distribution for different number of events. The black lines define the  $1\sigma$  and  $2\sigma$  confidence intervals over  $c/\Lambda^2$ .

a value that disfavors the SM-like scenario. In this case, the MEM outputs  $P(x|0) \ll P(x|1)$ , thus making the  $c = 0$  configuration no longer the most likely, lifting the minimum corresponding to it and turning it into a local maximum. As expected, this feature tends to disappear the more the statistics increases.

#### 4.2.4.2. MLE at reconstruction-level

For an event where particles interact with the detector, the reconstructed four-momenta of the visible particles are no longer equal to the generator-level ones, and transfer functions come into play to encode the detector reconstruction effects. Unlike the generator-level case, the neutrino variables are no longer known, and the  $E_T^{\text{miss}}$  is the only information that one owns about them. The system is kinematically constrained by the energy-momentum conservation law and the additional kinematic constraints coming from the on-shell decays of the top quarks and the W bosons. Their invariant masses appear as Breit-Wigner peaks in the integrand of Eq. 4.20. Moreover, transfer functions for the visible particles are needed to encode the detector effects. Therefore, the integration is needed and details about it can be found in Section 4.2.3.

A basic selection is applied to select the  $t\bar{t}$  events: jets and muons with at least 15 GeV are considered, and at least two OS muons and two b tagged jets are required. Only the two muons and two b jets with the highest  $p_T$  are kept.

In this case, the negative log-likelihood is built with 20,000 events, out of which 2949 pass the selection. The results are shown in Fig. 4.10a, where the negative log-likelihood functions built with both generator and reconstruction-level events are plotted together. It can be noticed that at reconstruction level better sensitivity is achieved with respect to the generator-level case. This is counter-intuitive, since the most complete information about the events is held at generator level, and therefore the best possible information can be extracted with the MEM. However, this feature finds its origin in four events that yield  $P(x|0) \ll P(x|1)$ , as seen in the previous section: the presence of the two minima slightly broadens the bottom of the parabola at generator level. The corresponding reconstructed events are all characterized by particles with a lower  $p_T$ , favoring the SM scenario and therefore yielding one minimum only. This is confirmed in Fig. 4.10b, where the four "outliers" are removed: the best sensitivity is now provided in the generator-level case, as expected. The value of the MLE at reconstruction level for 2949 events together with the  $1\sigma$  and  $2\sigma$  confidence intervals is reported in Table 4.2. This value is in agreement with its true value, within uncertainties.

#### 4.2.5. Final considerations

The MEM is a well-established technique for parameter inference. The measurement of the top mass with the D0 and CDF experiments at Fermilab [101,106,107]

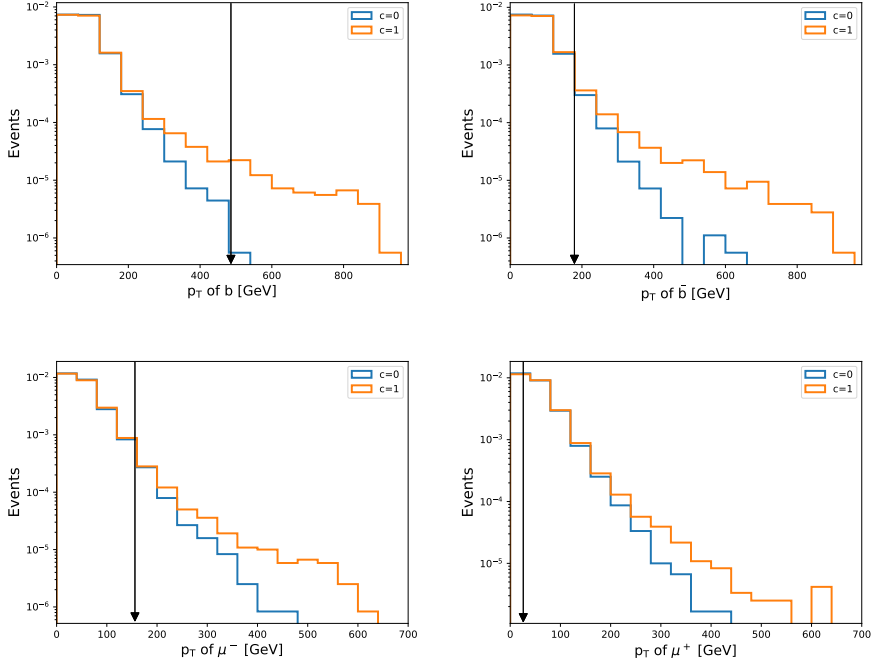
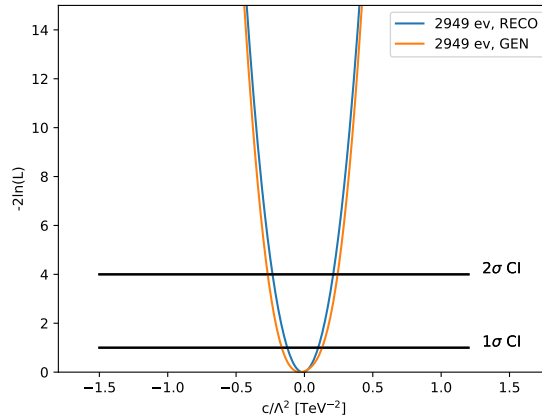


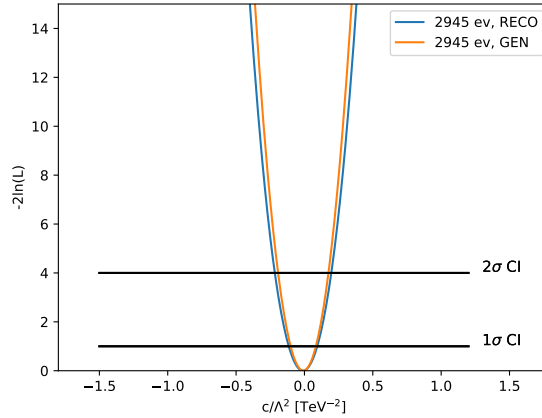
**Figure 4.9.** | Distributions of  $p_T$  of the four visible particles where the  $p_T$  associated to the particles contained in the event yielding the two-minima structure are shown with a black arrow.

**Table 4.2.** | Maximum likelihood estimator  $\frac{\hat{c}}{\hat{\Lambda}^2}$  with the corresponding  $1\sigma$  and  $2\sigma$  confidence intervals for 2949 reconstruction-level events. The true value is also displayed for reference.

$\frac{c}{\Lambda^2 \text{ true}} [\text{TeV}^{-2}]$	$\frac{\hat{c}}{\hat{\Lambda}^2} [\text{TeV}^{-2}]$	$1\sigma \text{ CI} [\text{TeV}^{-2}]$	$2\sigma \text{ CI} [\text{TeV}^{-2}]$
0	-0.013	[-0.125,0.103]	[-0.233,0.210]



(a)



(b)

**Figure 4.10.** | Negative log-likelihood as a function of  $c/\Lambda^2$  built on generator-level (orange line) and reconstruction-level (blue line) events for 2949 (a) events and 2945 (b) events, where the ones yielding a double-minima structure in the gen-level case are skipped. The black lines define the  $1\sigma$  and  $2\sigma$  confidence intervals over  $c/\Lambda^2$ .

represents a valid example of its applicability. This chapter demonstrates its usefulness in measuring the SMEFT  $c_{Qq}^{11}$  coefficient. From Fig. 4.10b it can be noticed that the  $1\sigma$  CI is very similar in the generator-level and reconstruction-level case. This proves the strength of the MEM: the detector effects are encoded in the computation of the ME weight by means of well-parametrized transfer functions.

To estimate the effect of statistical fluctuations on the measurement of the parameter, the minimization of the negative log-likelihood was repeated 10 times for independent batches of 10,000 events each on generator-level events. The MLE together with its  $1\sigma$  and  $2\sigma$  CI is reported in Table 4.3 for each batch. Statistical fluctuations slightly shift its value for each batch of events, as one would expect. The consistency between the MLE and the true value of the parameter is always ensured within the  $1\sigma$  CI. However, it can be noticed that for all batches of events the value of the MLE is always slightly shifted towards negative values. Assuming a non-biased measurement, the expected fraction of upwards and downwards fluctuations with respect to the true value is  $1/2$ . The probability that the value would always be shifted downwards is of the order of 0.001. Interpreting this probability as a p-value and setting a threshold of 0.05, the hypothesis of an unbiased measurement can be rejected at the commonly used 95% CL. Different PDF sets and factorization and renormalization scales were used in the MoMEMt configuration and the MADGRAPH settings when the sample was generated. Explanations for such bias might lie in these mismatches. Despite this, all values are consistent with the true one within uncertainties, making this small bias something to account for in possible future applications of this method, but without significantly impacting the results of this study.

At reconstruction level, this study is carried out on a sample with a luminosity of  $3.8 \text{ fb}^{-1}$ . It is interesting to estimate how the sensitivity would improve at the luminosities delivered by the LHC, in order to get a feeling on how this search would apply to measurements on real data. At a luminosity of  $36 \text{ fb}^{-1}$ , the  $1\sigma$  CI in Table 4.2 would be reduced by roughly a factor 3. Assuming for simplicity a symmetric CI around 0, this would become  $[-0.04, 0.04]$ . One must notice that no systematic uncertainty is taken into account in this study, and that a proper inclusion of these uncertainties in the estimate of the parameter would degrade the sensitivity. However, these bounds are comparable to the existing single-operator bounds  $[-0.2, 0.02]$ , derived using CMS datasets up to  $36 \text{ fb}^{-1}$  and ATLAS datasets up to  $80 \text{ fb}^{-1}$  [5]. Finally, it is to be noticed that, while in traditional methods usually only one coefficient at the time is constrained (with all the others set to 0), the MEM represents a generalization since the maximization of the likelihood can easily be multi-dimensional. These considerations make the method interesting for future applications to collider data.

**Table 4.3.** † Maximum likelihood estimator  $\frac{\hat{c}}{\Lambda^2}$  with the corresponding  $1\sigma$  and  $2\sigma$  confidence intervals for 10 independent batches of 10,000 generator-level events each.

Batch	$\frac{\hat{c}}{\Lambda^2}$ [TeV <sup>-2</sup> ]	$1\sigma$ CI [TeV <sup>-2</sup> ]	$2\sigma$ CI [TeV <sup>-2</sup> ]
#1	-0.019	[-0.091,0.055]	[-0.157,0.125]
#2	-0.014	[-0.077,0.049]	[-0.138,0.112]
#3	-0.021	[-0.094,0.056]	[-0.160,0.127]
#4	-0.030	[-0.104,0.061]	[-0.167,0.134]
#5	-0.015	[-0.079,0.050]	[-0.142,0.114]
#6	-0.013	[-0.074,0.048]	[-0.133,0.109]
#7	-0.017	[-0.085,0.053]	[-0.151,0.120]
#8	-0.016	[-0.084,0.052]	[-0.149,0.119]
#9	-0.014	[-0.077,0.050]	[-0.139,0.112]
#10	-0.017	[-0.086,0.053]	[-0.152,0.121]



## 5.

## Chapter

**Search for two new Higgs bosons through the  $H \rightarrow ZA \rightarrow \ell^+ \ell^- b \bar{b}$  process**

As largely described in Chapter 2, the 2HDM is one of the simplest extensions of the scalar sector of the SM, adding a second scalar doublet to it and thus predicting the existence of five new physical fields. In this thesis, the search for the scalar  $H$  and pseudoscalar  $A$  is presented.

The data collected by high-energy physics experiments can be analyzed in order to search for new resonances. Here, the data used were recorded by the CMS experiment in pp collisions during 2016 at  $\sqrt{s} = 13$  TeV, at an integrated luminosity  $\mathcal{L} = 35.9 \text{ fb}^{-1}$ .

When searching for one or more new resonances, two main components come into play: the signal and the background. The signal represents the process being searched for, that may or may not occur during a collision at colliders. Processes that mimic the signal, either because they are characterized by the same final state or because of particles being misidentified as particles contained in the signal, occur as well, and they are referred to as background. The chosen theoretical model where the signal is extracted from provides the expected number of signal events via MC simulation of the process. The expected number of background events can be similarly extracted from MC simulation of the background processes, or from data-derived background estimates.

The search effectively consists in looking for a deviation in the expected number of background events on the data collected by the experiment. Such deviation may be compatible with the predicted number of signal events, hence validating the existence of the signal. More in general, a significant difference in the shape of the distributions or in the number of events might represent a hint of new physics in a more model-independent perspective.

Disentangling the signal from the background on data is challenging and requires a very good understanding of the data. This is achieved by means of *control regions*, i.e. regions of the phase space populated by background events only. Such signal-free regions are used to check the MC simulation distributions and possibly correct and normalize them in order to match those of data within the statistical and systematic uncertainties. Control regions may also be used to derive a data-driven estimate of one or more background

processes. By doing so, one is able to remove the systematic uncertainties related to the MC simulation, improving the sensitivity of the search.

On the contrary, the *signal region* is defined as a region of the phase space that is likely to contain the signal, and it represents the place where the above-mentioned deviation is searched for.

A statistical analysis must be carried out to assess the level of compatibility of the observed data in the signal region with the hypothesis that there is no signal, by means of the p-value or significance, as explained in Chapter 4. Upper limits at 95% CL are also set, for instance, on the product of the observed signal cross section and its branching ratio. This can then be used to interpret the results in the context of the desired theoretical framework. In the case of this thesis, the theoretical Type-II 2HDM cross section is compared to the observed upper limits: this allows for regions of the 2HDM parameter space being examined to be constrained.

In Section 5.1, the signal process is presented together with the backgrounds contributing to this search. In Section 5.2, the object reconstruction is briefly presented; the event selection used is motivated and control regions are shown. Then, in Section 5.3 the definition of the signal region is discussed and a method to mitigate the mismodeling of the DY + jets background is presented in Section 5.4. In Section 5.5 the systematic uncertainties entering the search are discussed and results are presented in Section 5.6. Section 5.7 focuses on the method used to estimate the look-elsewhere effect in two dimensions, while in the last section of this chapter a comparison with the results obtained by other searches is discussed.

## 5.1. $H \rightarrow ZA \rightarrow \ell^+ \ell^- b\bar{b}$ : signal and backgrounds

In this section, an outline of the signal and background processes is given, together with details about their MC simulation used in this analysis.

### 5.1.1. The signal

The new bosons H and A predicted by the 2HDM are searched for in this analysis both in the classical and twisted mass hierarchy depicted in Fig. 2.2. The decay modes are chosen according to the trend of the probability decay of H and A displayed in Fig. 2.1. Therefore, the signal that we search for is:

$$H/A \rightarrow Z (\rightarrow \ell^+ \ell^-) A/H (\rightarrow b\bar{b}) .$$

This is depicted in Fig. 5.1. The leptons coming from the decay of the Z boson considered in this search are electrons and muons. Then, the signature of this search consists of two isolated b-tagged jets and two oppositely-charged and same-flavor (SF) leptons originating from the decay of the Z boson.

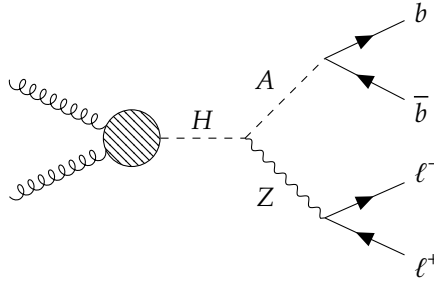


**Figure 5.1.** | Representative Feynman diagram of the production of the  $H \rightarrow ZA$  process.

The search is conducted in the plane defined by the reconstructed masses of the two new bosons. Because the masses are spin-independent variables, in practice the search is carried out for one process only ( $H \rightarrow ZA$ ) and then mirrored, i.e. the two masses are interchanged. This procedure allows for theoretical interpretation of the results in the context of the 2HDM in both the classical and twisted scenario.

Signal simulation samples were produced with MADGRAPH5\_aMC@NLO version 2.3.2 [88] interfaced with the parton shower generator PYTHIA 8.212 [90]. The parton distribution function (PDF) set is NNPDF 3.0 [108] at LO in the four-flavor scheme, and the factorization and renormalization scales are estimated dynamically.

The samples are produced under 207 different mass hypotheses, with the mass of the  $H$ ,  $m_H$ , ranging from 130 to 1000 GeV and the mass of the  $A$ ,  $m_A$ , from 30 to 1000 GeV. The choice of the masses in the  $m_A$  vs.  $m_H$  plane is roughly parametrized according to the resolution of the reconstructed mass distributions of 21 signal samples that were already available beforehand, and it is specifically chosen to achieve a complete coverage of the mass parameter space. The mass hypotheses used for the simulated samples are reported in Fig. 5.2. These samples have been generated close to the alignment limit, with  $\tan\beta = 1.5$  and  $\cos(\beta - \alpha) = 0.01$  in a Type-II 2HDM. The NNLO cross sections for each signal hypothesis are computed with SUSHI version 1.6.1 [109], while the corresponding branching ratios are computed with 2HDMC version 1.7.0 [110]. The product of the theoretical cross section and branching ratio for two Type-II 2HDM benchmarks is shown in Fig. 5.3. On the left, the  $m_A$  vs.  $m_H$  parameter space is shown for  $\tan\beta = 1.5$  and  $\cos(\beta - \alpha) = 0.01$ ; on the right, the  $\cos(\beta - \alpha)$  vs.  $\tan\beta$  parameter space is shown for  $m_H = 379$  GeV and  $m_A = 172$  GeV.

## 5.1.2. The backgrounds

We will now discuss the background processes relevant to this search. Thanks to the excellent  $b$  tagging and lepton identification, only backgrounds with two

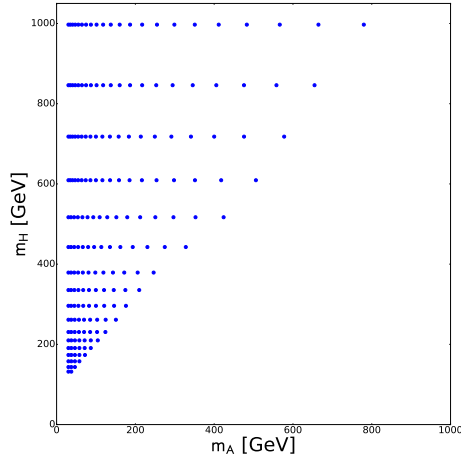


**Figure 5.2.** | Mass hypotheses in the  $m_A$  vs.  $m_H$  plane used for the production of the simulated signal samples.

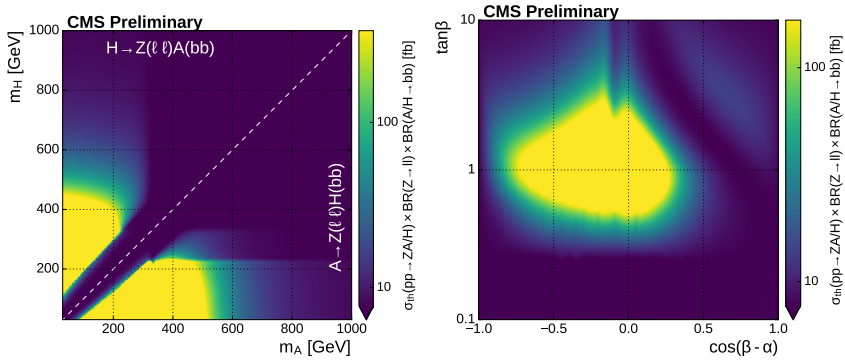


**Figure 5.3.** | Product of the theoretical cross section and branching ratio  $\text{BR}(H/A \rightarrow ZA/H) \times \text{BR}(Z \rightarrow ee/\mu\mu) \times \text{BR}(A/H \rightarrow b\bar{b})$  in the  $m_A$  vs.  $m_H$  parameter space for  $\tan\beta = 1.5$  and  $\cos(\beta - \alpha) = 0.01$  (left) and in the  $\cos(\beta - \alpha)$  vs.  $\tan\beta$  parameter space for  $m_H = 379$  GeV and  $m_A = 172$  GeV (right).

genuine b jets and two isolated leptons are relevant, with a small contribution coming from events with one misidentified lepton. In this scenario, the most dominant ones are the production of Drell-Yan in association with heavy-flavor jets (DY + jets in short), and production of a top quark pair in the fully leptonic final state. Figure 5.4 shows the signal and background cross sections, with the purpose of highlighting how they compare. It is trivial to see how the cross section of the signal is much lower compared to the background processes, motivating a search with high sensitivity. The signal cross section varies depending on the values of the 2HDM parameters. Here, it is set to 1 pb as a sensible representative value. It is worth pointing out that the process with the highest value of the cross section does not necessarily represent the most dominant background. Here, the W + jets background yields the highest cross section, but its contribution to the backgrounds is very sub-dominant, since its kinematics happen to be very different from the signal one: it is therefore a lot reduced when cuts are applied to select signal-like events.

Below, the background processes are listed and described from the most dominant to the least.

### Drell-Yan + jets

The Drell-Yan process occurs in high-energy hadron-hadron scattering when a quark from one hadron annihilates with the quark from another hadron into a virtual photon  $\gamma^*$  or a Z boson, which then decays into a pair of oppositely-charged leptons. Very frequently within the collisions, this process is produced in association with jets, coming from, for instance, gluons radiated by the annihilating quarks and/or from their subsequent splitting into a quark pair. In particular, if the number of produced jets amounts to more than 1, with the jets originating from b quarks, then this process constitutes a substantial background for the  $H \rightarrow ZA$  search, and it is irreducible. Indeed, the two leptons coming from the decay of the Z boson and the two b jets mimic exactly the signal final state. Instead, if the jets originate from light-flavor quarks, then the only way this process could be mistaken for the signal under study is if both jets are misidentified as b jets. Given that the b tagging WP used in this analysis yields a misidentification probability of about 1%, this background can be considered minor. Production of DY + b jets can occur in different ways. In Fig. 5.5, two examples of how its production takes place at LO are sketched. Simulation samples of this background are generated with MADGRAPH5\_aMC@NLO version 2.2.2 [88] with PYTHIA 8 [90] for parton showering at NLO precision in QCD, using the FxFx [111] procedure for NLO jet merging and MADSPIN [112] to properly propagate spin information in the matrix element of the process. The samples used for the search are binned in number of jets, from 0 to 2, generated with the invariant mass of the lepton pair ( $m_{\ell\ell}$ ) above 50 GeV. Another sample

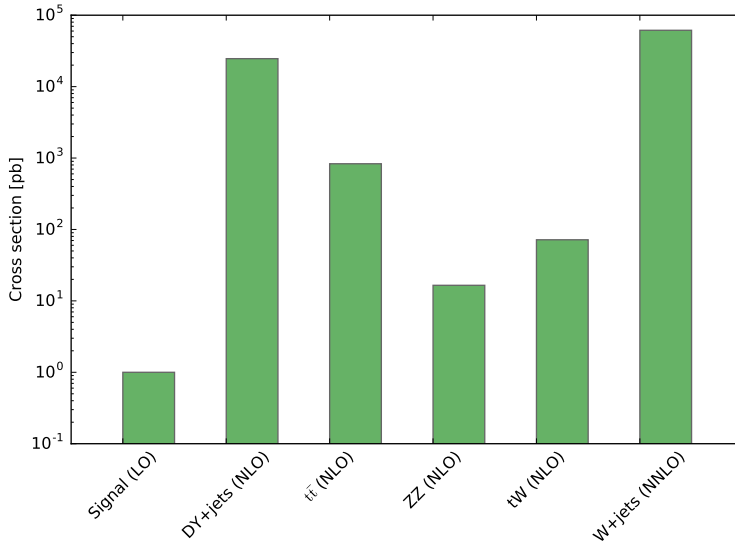


**Figure 5.4.** | Cross sections of the signal and of the background processes entering the search. The signal cross section is set to 1 pb as a sensible representative value. All cross sections are inclusive except for DY + jets and W + jets, where only leptonic decays are considered.

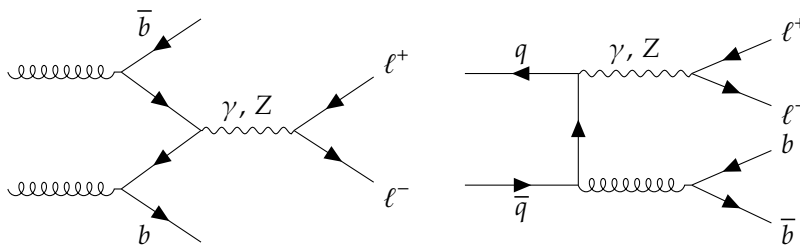


**Figure 5.5.** | Two examples of DY production in association with b jets at leading order.

is used with  $10 < m_{\ell\ell} < 50$  GeV. The total cross section amounts to  $24640^{+5.3\%}_{-5.2\%}$  pb at  $\sqrt{s} = 13$  TeV.

### Top quarks pair

The  $t\bar{t}$  background process consists in the production of a pair of top quarks from gluon-gluon fusion and more rarely from annihilation of a quark and an antiquark. Because of its phenomenology, this background plays a non-negligible role in the search: it is the second most dominant background. The signal final state is mimicked in the fully-leptonic case. This occurs when both the  $W$  bosons originating from the decay of the tops quarks decay to leptons. In particular, two scenarios are possible: both the  $W$  bosons decay to electrons or muons; or, less trivially, at least one of the  $W$  bosons decays to a  $\tau$  lepton, which then decays leptonically. An event of this kind contains two isolated  $b$ -tagged jets coming from the decay of the top quarks, two leptons with opposite charge, and  $E_T^{\text{miss}}$ , mostly originating from the presence of the neutrinos from the  $W$  decays. The fully-leptonic  $t\bar{t}$  background is therefore reducible, and its contribution can be mitigated by a cut on the  $E_T^{\text{miss}}$  variable, since the signal process is characterized by a low  $E_T^{\text{miss}}$  content. A sketch of the  $t\bar{t}$  fully-leptonic production process via gluon-gluon fusion at leading order is depicted in Fig. 5.6. The  $t\bar{t}$  samples used in this search are generated with POWHEG [89] version 2. An inclusive  $t\bar{t}$  sample is used together with a fully-leptonic sample with the purpose of increasing the statistics. The two samples are merged and fully-leptonic events from the inclusive sample are subtracted in order to avoid double counting. The inclusive sample yields a cross section of  $831.76^{+4.8\%}_{-5.4\%}$  pb at  $\sqrt{s} = 13$  TeV. The production of a SM Higgs boson in association with a top quark pair represents a very minor background. Its simulation sample is generated with POWHEG [89] version 2.

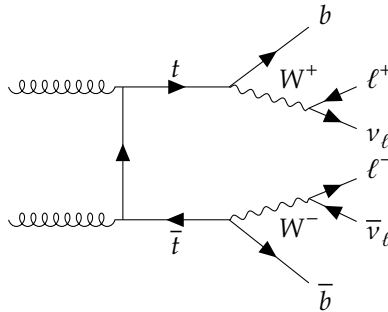


**Figure 5.6.** | Example of production of  $t\bar{t}$  process in the fully-leptonic final state at leading order via gluon-gluon fusion.

## ZZ and Zh

The production of a Z boson pair constitutes an irreducible background for this search when one of the two Z bosons decays leptonically to electrons or muons, and the other one decays to a pair of b quarks. A simulated  $ZZ \rightarrow \ell^+ \ell^- b\bar{b}$  sample is produced with MADGRAPH5\_aMC@NLO version 2.2.2 [88]. Processes with fully-hadronic decays of the Z bosons constitute a background, although minor, if two jets are misidentified as leptons, and therefore they are also considered in the search. The inclusive cross section amounts to  $16.52_{-2.4\%}^{+3.2\%}$  pb at  $\sqrt{s} = 13$  TeV.

Moreover, the production of a SM Higgs boson via higgs-strahlung (see Section 1.3) also constitutes a background for this search if the Higgs boson is radiated from a Z (subsequently decaying leptonically) and decays to a pair of b quarks. The simulation sample for this background is produced with POWHEG [89] version 2, and its inclusive cross section amounts to  $0.88_{-5.5}^{+6.4}$  pb. Figure 5.7 shows a sketch of the ZZ (left) and Zh (right) production at leading order. The minor backgrounds consisting of W boson pair production and WZ production, called, together with ZZ, *diboson* backgrounds (VV) and *triboson* (VVV, with  $V = W, Z$ ) production are also considered in the analysis and are generated at NLO precision with POWHEG [89] version 2. All background processes containing a SM Higgs boson are referred to as *SM Higgs* in the following.

## Single top quark

In addition to the production of top quarks pairs, a significant number of (anti)top quarks (*top*, for shortness) can be produced singly, via the weak interaction. Single top production proceeds through three separate sub-processes at LHC: the tW-channel, where the single top quark is produced in association with a W boson, the t-channel, and the s-channel. Among these, the process which gives the highest contribution to the single top quark production is the

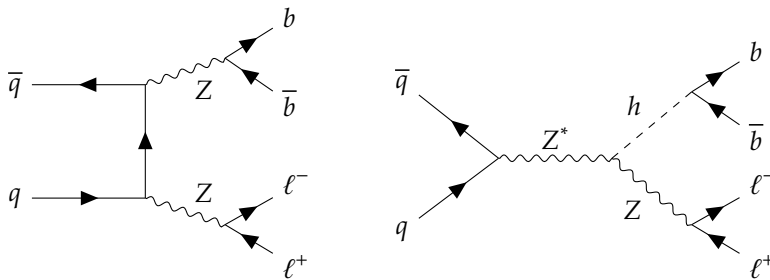


**Figure 5.7.** | Example of production of a Z boson pair (left) and of Zh via higgs-strahlung (right) at leading order.

t-channel, followed by the tW-channel, and finally by the s-channel. Despite the higher cross section, the t-channel represents a very minor background for the  $H \rightarrow ZA$  search, together with the s-channel: because of the presence of only one lepton in the final state, these contributions are heavily reduced when two leptons are required in the signal selection. Most of the single top background in the search originates from the tW-channel. Here, the two leptons come from the decay of the W bosons, and one b jet comes from the decay of the top. The signal is mimicked when a b quark is produced from gluon splitting or from particle misidentification.

Single top simulation samples in the three channels are generated with MADGRAPH5\_aMC@NLO version 2.2.2 [88]. In particular, the simulation of the tW-channel production is performed in the so-called five-flavor scheme, where the b quarks are treated as massless and can therefore be found in both initial and final states. Its inclusive cross section at NLO amounts to  $71.7 \pm 3.8$  pb at  $\sqrt{13}$  TeV. The t-channel and s-channel are generated in the four-flavor scheme, where the b quarks are treated as massive and therefore they can be in the final state only. The three production channels are depicted in Fig. 5.8.

### W + heavy-flavor jets

The production of a W boson in association with heavy-flavor quarks (W + heavy-flavor jets) represents another background to this search. The signal final state can be mimicked when one or more gluons are radiated. Its production is sketched in Fig. 5.9. A simulation sample of W + jets with leptonic decay of the W is produced with MADGRAPH5\_aMC@NLO version 2.2.2 [88], and its cross section at NNLO amounts to  $61527^{+1366}_{-1344}$  pb at  $\sqrt{s} = 13$  TeV.

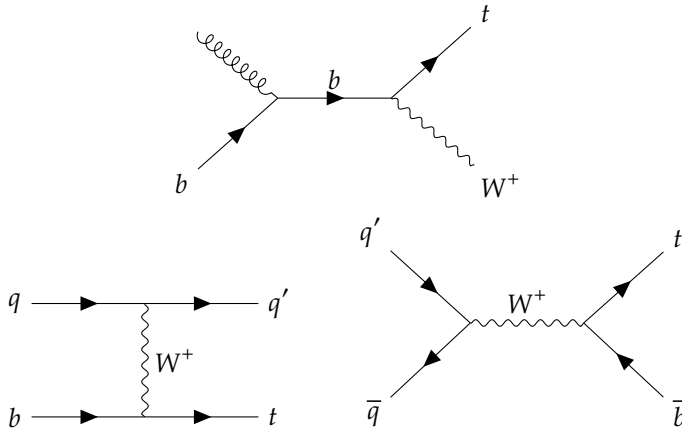


**Figure 5.8.** | Single top quark production in the tW-channel in the five-flavor scheme (upper), t-channel (lower left), and s-channel (lower right) at leading order. The single anti-top quark production diagrams are obtained by inverting the direction of the arrows and swapping each particle with its anti-particle.

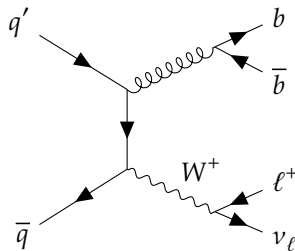


**Figure 5.9.** | Example of  $W +$  jets production at leading order.

## 5.2. Object reconstruction and event selection

Given the presence of two leptons in the signal final state, events for this search are selected by a trigger based on the di-lepton signature. Three trigger channels are considered, according to the di-lepton flavor:  $e^\pm e^\mp$ ,  $\mu^\pm \mu^\mp$ , and  $\mu^\pm e^\mp + e^\pm \mu^\mp$ . In this notation, the first (second) lepton of the pair corresponds to the one with the highest (lowest)  $p_T$  value and is called leading (subleading). To ease the reading, they are referred to  $ee$ ,  $\mu\mu$ , and  $\mu e$ , respectively, throughout this thesis. While the first two channels allow to select SF lepton events, that are signal-like and therefore of primary interest for the search, the latter selects mixed-flavor lepton events, which are used to define an auxiliary phase space region to better model the  $t\bar{t}$  background, as discussed in Section 5.3. The HLT paths are chosen such that the  $p_T$  thresholds applied to the leptons in the three channels are: 23 (12) GeV for the leading (subleading) lepton in the  $ee$  channel; 17 (8) GeV for the leading (subleading) lepton in the  $\mu\mu$  channel; 23 for the leading lepton and 8 (12) for the subleading muon (electron) in the  $\mu e$  channel. The trigger efficiencies are computed with the Tag & Probe technique [91] and applied to MC simulation.

Reconstruction of particle objects in CMS has been discussed in detail in Section 3.3. In this section, we will briefly summarize the selection requirements. Once reconstructed, corrections are applied to the simulated distributions in order to help match the observed data in specific control regions. The latter are shown with the purpose of emphasizing the importance of such corrections and of attesting that the data have been reproduced by the MC simulation and well understood, before moving on to discussing the actual search in the signal region.

### 5.2.1. Object reconstruction at a glance

We consider electrons (muons) with a  $p_T$  of at least 15 (10) GeV and in the range  $|\eta| < 2.5$  (2.4). The trigger, identification, and isolation efficiencies are extracted and scale factors are applied to each simulated event.

The so-selected muons and electrons in one event are paired. The leading electron is required to have a  $p_T$  of at least 25 GeV, while the leading muon is required to have  $p_T > 20$ (25) GeV for same (opposite)-flavor pairs. The pairs with same-sign leptons are discarded to keep only the candidate di-leptons originating from a  $Z$  boson. Among these, only the pair with the highest  $p_T$  is kept, defining a di-lepton object. Its invariant mass is required to be above a threshold of 12 GeV to suppress resonances from quarkonia [113].

Jets with  $p_T > 20$  GeV and lying in the pseudo-rapidity range  $|\eta| < 2.4$  are considered. Similarly to leptons, all selected jets in one event are paired together, defining di-jet objects.

Table 5.1 sums up the reconstruction and selection requirements.

**Table 5.1.** | Object definitions and selection cuts.

Object	Definition	Selection cuts
leading (sub-leading) $e$	Medium + HLT safe ID	$p_T > 25(15)$ GeV, $ \eta  < 2.5$
leading (sub-leading) $\mu$	Tight ID PF ISO ( $\Delta\beta$ -corr.) $< 0.15$	$p_T > 20(10)$ GeV, $ \eta  < 2.4$ $p_T > 25$ GeV for $\mu e$ events
$\ell\ell$	Di-lepton object	$m_{\ell\ell} > 12$ GeV
jets	PF anti- $k_T$ 0.4	$p_T > 20$ GeV, $ \eta  < 2.4$
b tagging	DeepCSV medium WP	$p_T > 20$ GeV, $ \eta  < 2.4$

### 5.2.2. Identifying the $\ell\ell jj$ final state

Once the di-lepton and the di-jet objects have been defined, these are further paired together, and only the one with the highest value of the deepCSV algorithm output is kept. This defines the  $\ell\ell jj$  object. The di-lepton object that constitutes it can either have same or opposite-flavor leptons, and the di-jet pair can either be b tagged or not. If the di-jet pair is b tagged, the event is flagged as such. Three categories are defined according to the flavor of the di-lepton:  $ee$ , when both leptons are electrons;  $\mu\mu$ , when both leptons are muons;  $\mu e$ , when one lepton is an electron and the other is a muon.

At this stage, various kinematics distributions can be looked at to check the agreement between data and MC simulation. Figure 5.10 (5.11) shows  $p_T$  and  $\eta$  distributions of the leading and sub-leading muon (electron) for events containing two muons (electrons), while Fig. 5.12 shows the  $p_T$  distribution of the di-jet system in the  $\mu\mu$  and  $ee$  categories for both non-b tagged (upper) and b tagged (lower) events. Error bars indicate statistical uncertainty, while shaded bands indicate systematic uncertainties, that are discussed in detail in Section 5.5. The label *Other* in the figures indicates the SM Higgs and  $W$  + jets minor backgrounds. Data and simulation are in agreement within uncertainties.

Once the  $\ell\ell jj$  object is defined, further selection cuts can be applied to define the signal region (or control regions where to further study compatibility between data and MC simulation and/or that can be used to constrain some backgrounds in the statistical analysis). This is discussed in the next section.

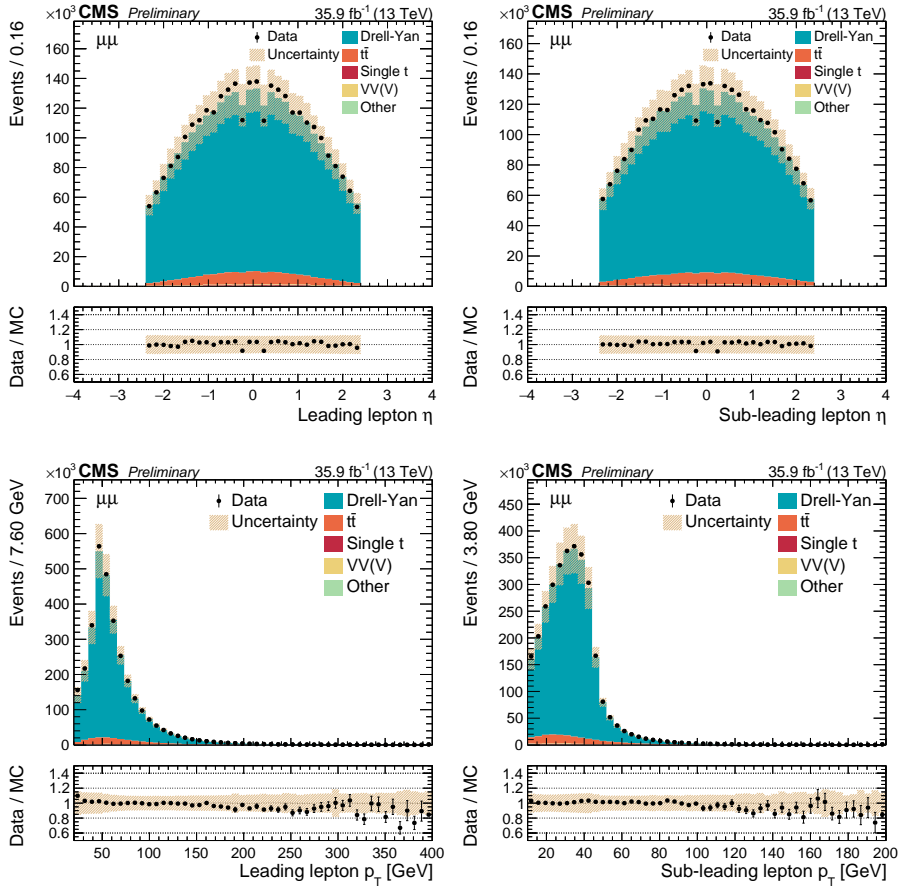


**Figure 5.10.** | Distributions of  $\eta$  (upper) and  $p_T$  (lower) for the leading (left) and sub-leading (right) muon.

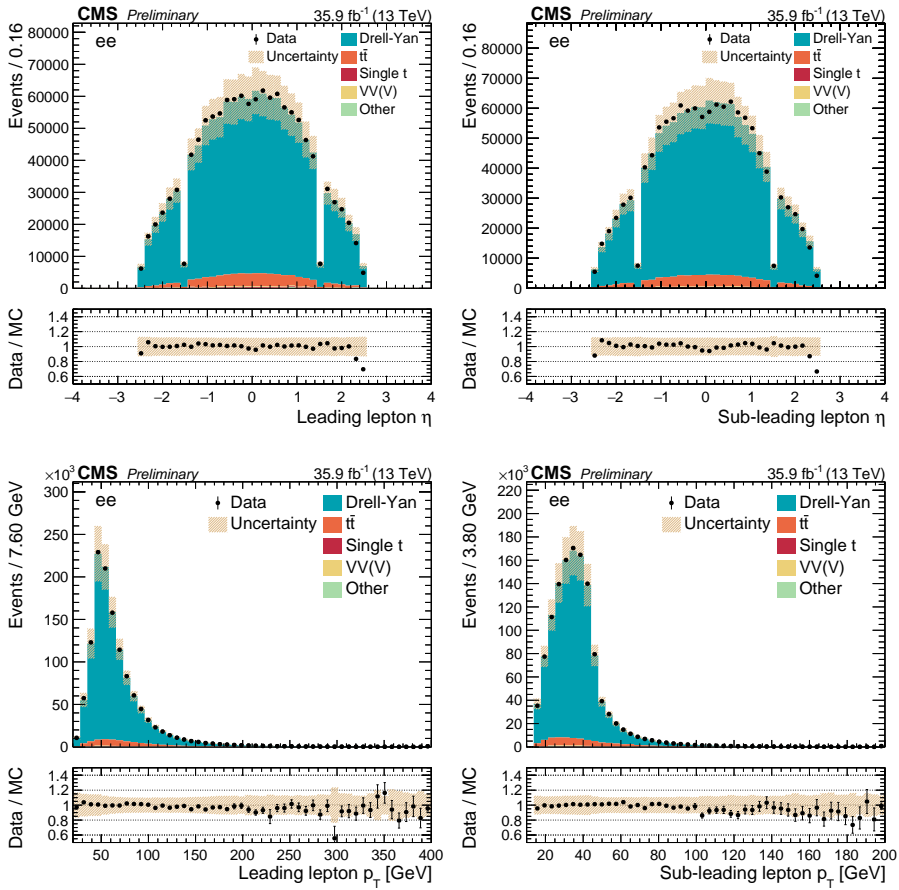


**Figure 5.11.** | Distributions of  $\eta$  (upper) and  $p_T$  (lower) for the leading (left) and sub-leading (right) electron.

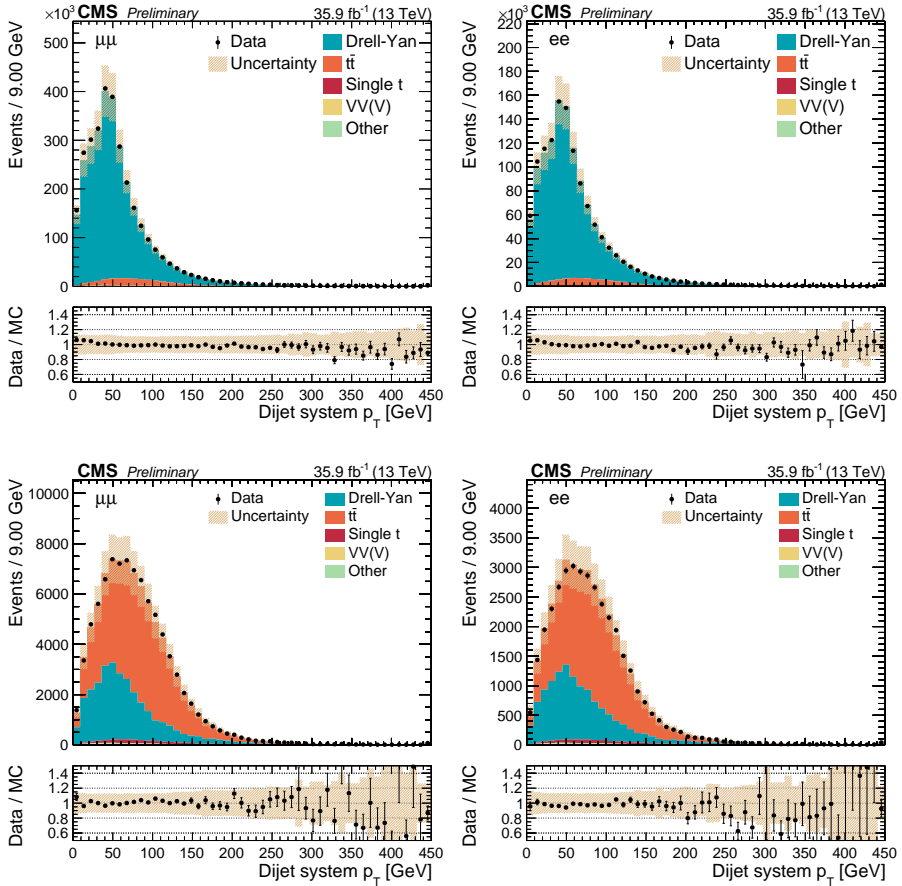


**Figure 5.12.** | Distributions of  $p_T$  of the di-jet system in the  $\mu\mu$  (left) and  $ee$  (right) channel for non-b tagged (upper) and b tagged (lower) events.

### 5.3. Signal region definition

Since the final state of the signal process consists of two leptons originating from a Z boson and two b quarks, in order to obtain signal-candidate events it would suffice to select events with two SF leptons and two b-tagged jets. This defines a *primary* signal region. However, there exist "preferred" regions of the phase space where the signal lies according to its kinematics. Figure 5.13 shows the  $m_{\ell\ell}$  and the  $E_T^{\text{miss}}$  distributions in the primary signal region with three signals under different mass hypotheses. As expected, the signal is mostly concentrated in the peak of the Z boson because of the two leptons originating from it; also, it is mostly located at low  $E_T^{\text{miss}}$ , because of the absence of neutrinos in its final state. Therefore, tightening the selection requirements to only accept events from these regions makes it possible to roughly keep the same number of signal events while reducing the number of background events, thus improving the sensitivity of the search. Specifically, the following two cuts are applied:

- $70 < m_{\ell\ell} < 110$  GeV: to enhance the presence of  $Z \rightarrow \ell\ell$  events;
- $E_T^{\text{miss}} < 80$  GeV: to reduce contribution from processes with real  $E_T^{\text{miss}}$ , such as  $t\bar{t}$ .

An optimization of the cut on  $E_T^{\text{miss}}$  has been performed. The signal significance can be defined with the following figure of merit:  $\xi = \sqrt{2[(S+B)\ln(1+S/B) - S]}$ , where  $S$  ( $B$ ) is the number of signal (background) events. One can compute this variable for different values of the  $E_T^{\text{miss}}$  cut and eventually pick the cut that yields the highest value. This is shown in Fig. 5.14 in the  $\mu\mu$  category (the result in the  $ee$  category is not shown to avoid redundancy as it is independent of the lepton flavor and hence very similar) and for six representative signal hypotheses. The best value of the cut slightly changes according to the signal hypothesis being considered. However, the requirement  $E_T^{\text{miss}} < 80$  GeV is overall a sensible choice to ensure high sensitivity throughout all hypotheses. With these additional selection requirements applied, Fig. 5.15 shows the final mass distributions of the di-jet object ( $m_{jj}$ ) and of the  $\ell\ell jj$  object ( $m_{\ell\ell jj}$ ) for the backgrounds and three different mass hypotheses. The observation of an excess of events with respect to the MC prediction in the former would indicate the presence of a resonance compatible with the A boson, while in the latter a resonance compatible with the H boson.

Examples of control regions are shown in Fig. 5.16. The upper part shows the distribution of the di-jet invariant mass and  $p_T$  for non-b tagged SF events (it can be seen that with these requirements a region rich in DY processes is selected), while the lower part shows the same distributions for b tagged and  $\mu e$  events (here, the control region is rich in  $t\bar{t}$  processes).

It is worth pointing out at this point that the signal  $m_{jj}$  and  $m_{\ell\ell jj}$  distributions

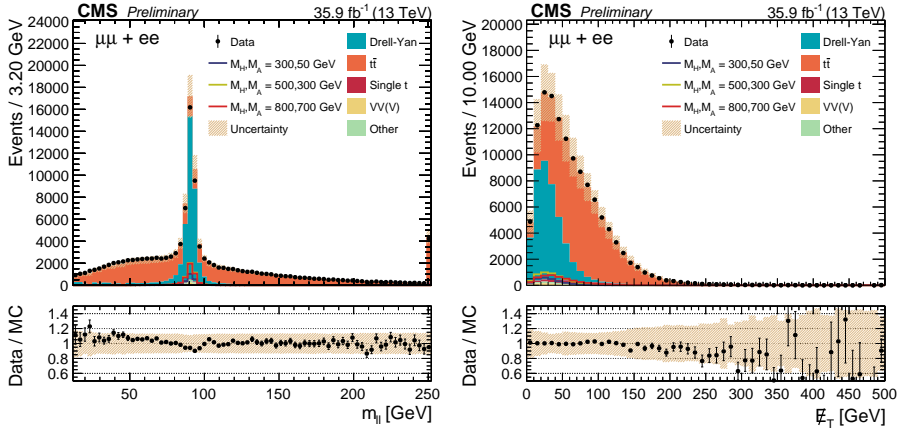


**Figure 5.13.** | Invariant mass distribution of the di-lepton system (left) and  $E_T^{\text{miss}}$  (right) in the primary signal region for SF events. This signal is normalized to 1 pb.

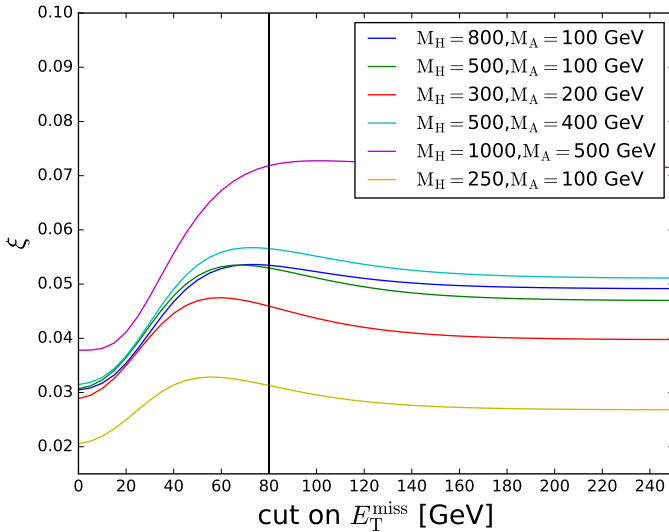


**Figure 5.14.** | Signal sensitivity  $\xi$  as a function of the cut on  $E_T^{\text{miss}}$  for six representative mass hypothesis. The black line indicated the final cut used for the analysis.

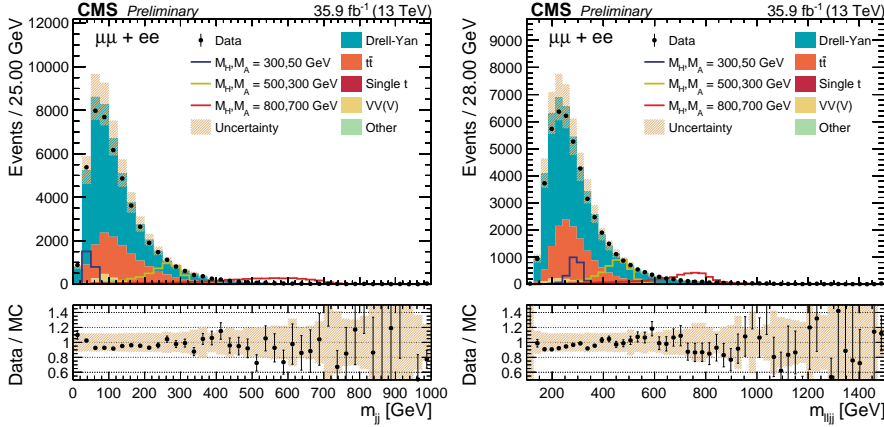


**Figure 5.15.** | Invariant mass distribution of the di-jet system (left) of the  $\ell\ell jj$  system (right) in the signal region. The  $\mu\mu$  and  $ee$  events are summed together. Simulated signals generated under the theoretical hypotheses  $(m_H, m_A) = (300, 50)$  GeV,  $(m_H, m_A) = (500, 300)$  GeV, and  $(m_H, m_A) = (800, 700)$  GeV are also plotted. They are normalized to 1 pb.

are inherently positively correlated under a particular signal hypothesis because of the signal kinematics. In order to exploit this correlation, the search is conducted in a two-dimensional phase space region, defined by the  $m_{jj}$  vs.  $m_{\ell\ell jj}$  mass plane (for shortness referred to as *mass plane* only throughout this thesis), rather than in one-dimensional (1D) mass distributions. The definition of the signal region is therefore further extended by additional requirements in order to ulteriorly enhance the sensitivity of the search. This is discussed in detail in the next section.

### 5.3.1. Parametrization of the signal region

The kinematics of the reconstructed  $m_{jj}$  and  $m_{\ell\ell jj}$  distributions for a specific signal process strongly depends on its theoretical parameters  $m_A$  and  $m_H$ . Moreover, the higher the value of the mass parameter, the more energetic its decay products and hence the larger the width of the associated mass distribution. This can be seen in Fig. 5.17, where the signal mass distributions are plotted for three different mass hypothesis and the  $\mu\mu$  and  $ee$  events are summed. A representation of such behavior in 2D is shown in Fig. 5.18, where the signal shape changes across the mass plane.

Another important feature emerges straightforwardly from Fig. 5.18: the signal distribution always shows a positive correlation, since the reconstruction of  $m_{\ell\ell jj}$  is strictly entangled with that of  $m_{jj}$ . Such correlation gives the 2D signal distribution an elliptical shape in the mass plane with parameters depending on the experimental resolution and on the mass hypothesis being considered.

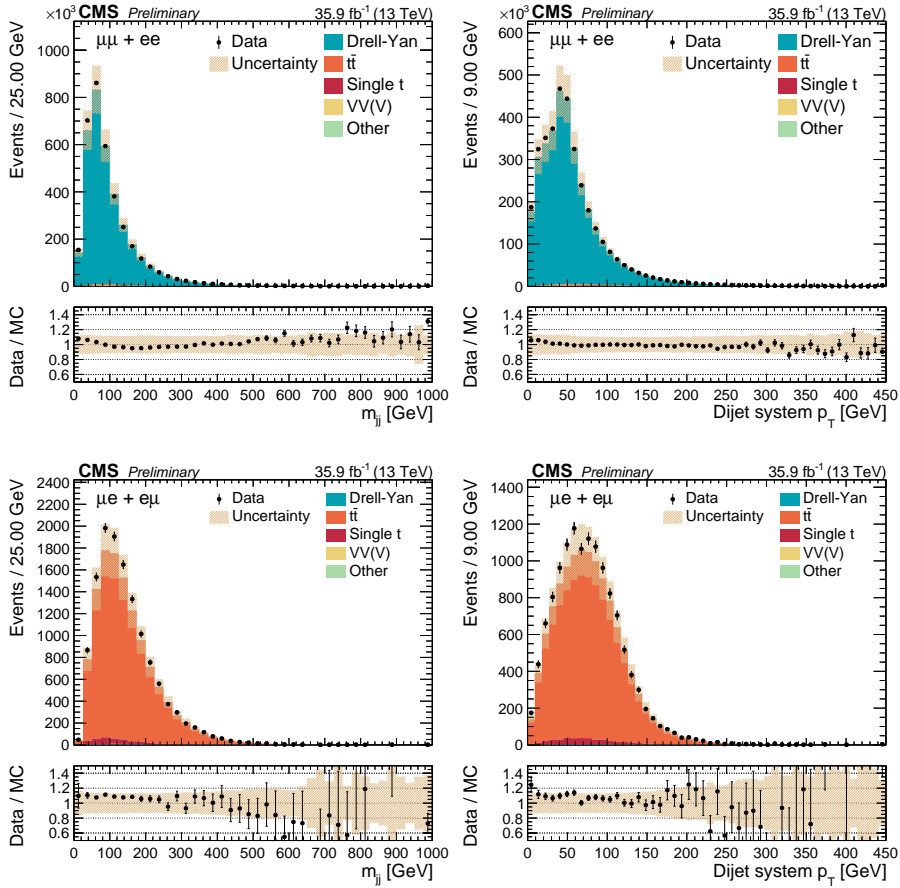


**Figure 5.16.** | Invariant mass (left) and  $p_T$  (right) distribution of the di-jet system in the SF (upper) and  $\mu e$  (lower) category after all the selection cuts are applied.

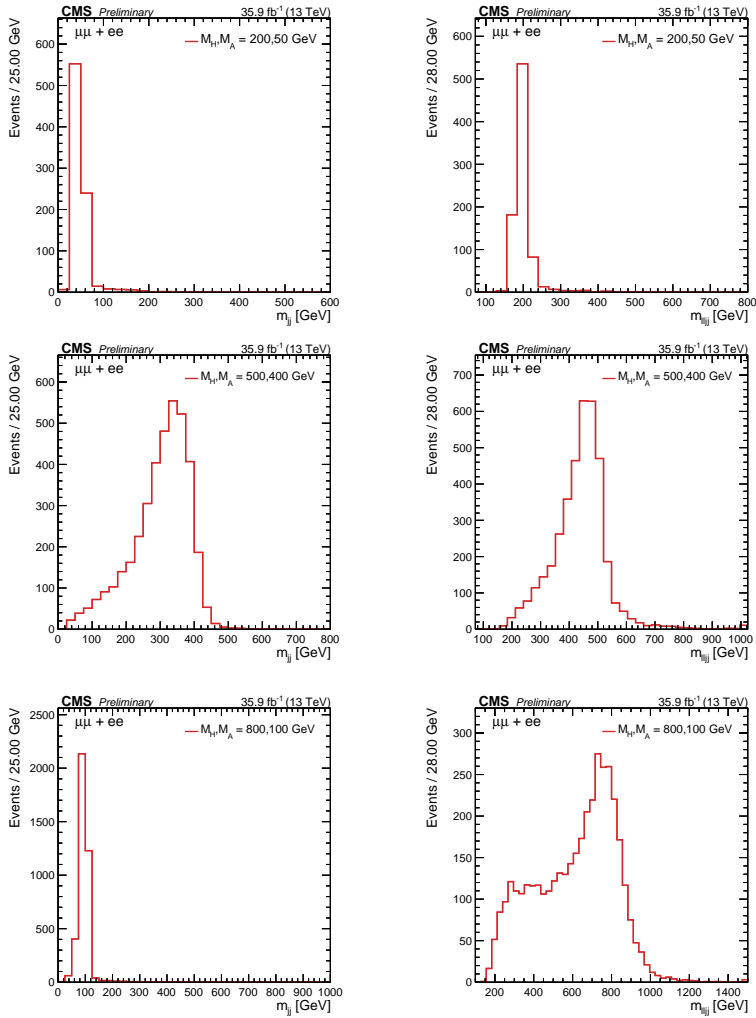


**Figure 5.17.** | Reconstructed  $m_{jj}$  (left) and  $m_{\ell\ell jj}$  (right) distributions for three representative mass hypotheses.

Elliptical curves enclosing the bulk of the signal distribution are drawn to emphasize this feature.

An elliptical cut on the 2D mass distribution of the signal appears like a sensible choice to further enhance the sensitivity, since it would be tailored to nicely enclose the signal while leaving out regions of the phase space where the signal contribution is null or very low and background events are present.

The definition of an elliptical signal region is the crucial feature of this search. This is an optimization of the strategy adopted for the same search with the data collected at  $\sqrt{s} = 8$  TeV and  $\mathcal{L} = 19.8 \text{ fb}^{-1}$  [114]. The main feature of this search is the definition of a rectangular signal region, with the size of the rectangle depending on the widths of the two reconstructed mass distributions. While this is certainly a sensible choice, it does not take into account the correlation between the two reconstructed masses, which is the main feature of the signal shape in the mass plane and should be exploited in order to achieve better sensitivity.

As pointed out in Chapter 4, nowadays many analyses are performed with MVA techniques which use supervised machine learning for signal vs. background discrimination and/or regression of kinematic variables. Methods such as *boosted decision trees* (BDTs) [115] are often used to discriminate between two different kinematic configurations: the output of a BDT gives an indication on how much a certain event is, for instance, signal-like, depending on the value of the output variable. Other common methods are based on the use of (deep) neural networks, which can be used to perform regression of kinematic variables of interest to the search. The advantage of using machine learning techniques is becoming more and more clear to the experimental scientific community. However, these methods often rely on a specific model, which is used to train the network. In the search presented in this chapter, while the use of machine learning for the definition of the signal region and/or for regression of the reconstructed masses is certainly possible, it is not pursued because it would make the analysis strategy too much dependent on the assumed model. The approach used for this search is purposefully kept as model-independent as possible, as this facilitates a re-interpretation of the results in different benchmarks or models. Moreover, because of the lack of neutrinos in the final state, the MEM would not be an optimal choice for this analysis, since the system is over-constrained by kinematics and the optimization performed by MoMEMta would not fully apply, making the MEM not competitive with other methods. However, it might show all its benefits if applied to the  $H \rightarrow ZA$  process with the A boson decaying to a pair of top quarks in the semi- or fully-leptonic final state, once the A mass is high enough to open the top quark pair production threshold. An interesting signal production mode for MEM application is also represented by the b-associated production, since it would allow the combinatorics of the final state to properly be taken into account.

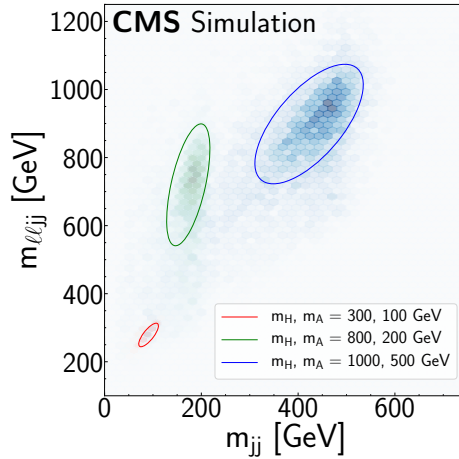


**Figure 5.18.** | Three signals in the mass plane defined by the two reconstructed masses  $m_{jj}$  and  $m_{\ell\ell jj}$  under three different mass hypothesis. The elliptical curves enclosing the bulk of the 2D distributions emphasize the positive correlation of the signal in the mass plane.

At this point, two main questions emerge and need to be addressed: how to parametrize the ellipses in the mass plane? And what criteria should one use to fix the size of the ellipse? These two points are discussed and tackled in the next sub-sections.

### 5.3.1.1. Ellipse parametrization

With the 207 signal simulation samples available, the "behavior" of the ellipses can be parametrized across the whole mass plane. This translates into extracting, for each mass hypothesis, the ellipse parameters: the centroid of the ellipse, with coordinates  $(c_x, c_y)$ ; the major and minor semi-axes  $a$  and  $b$ ; the tilt angle  $\theta$  (the angle spanning from the positive horizontal axis to the ellipse's major axis).

#### Extracting the centroid

The strategy adopted for the extraction of the coordinates of the centroid is to perform, for each signal hypothesis, a Gaussian fit of the  $m_{jj}$  and  $m_{\ell\ell jj}$  distributions and take the mean of  $m_{jj}$  ( $m_{\ell\ell jj}$ ) as the coordinate  $x_c$  ( $y_c$ ). This procedure works well for mass hypotheses up to 700 GeV. Above this threshold, the shape of the mass distributions (especially  $m_{\ell\ell jj}$ ) is highly non symmetric and with a peak towards low reconstructed masses, due to the presence of non-negligible non-resonant contributions to the signal production that become manifest at high masses, as shown in Fig. 5.17. There, the Gaussian fit fails at catching the resonant peak, providing a nonsensical centroid coordinate.

Moreover, for most hypotheses with low  $m_A$  (i.e.  $\sim 30$  GeV), the Gaussian fit performed on the  $m_{jj}$  distribution is not optimal at deriving the center of the distribution either, given its very narrow width. To overcome this issue, the centroid coordinates  $x_c$  ( $y_c$ ) that are well extracted from the fit are plotted as a function of the mass hypothesis  $m_A$  ( $m_H$ ) and fitted with a polynomial of grade 1. This is shown in Fig. 5.19 for the  $ee$  and  $\mu\mu$  channel. The fit function is then used for extrapolation of the centroid coordinates that could not be extracted from the Gaussian fit. It is to be noticed that the best-fit function lies a bit below the theoretical case, depicted with a dashed line in Fig. 5.19, where the reconstructed masses equal the theoretical ones. This is explained by the fact that the jet reconstruction technique does not account for neutrinos inside the jet cone which are frequent for b jets, lowering the reconstructed value.

### Extracting $a$ , $b$ , and $\theta$

The parameters  $a$ ,  $b$ , and  $\theta$  for each signal hypothesis are extracted from the covariance matrix of the 2D mass distribution in a window defined as  $(c_x \pm 50\%c_x, c_y \pm 50\%c_y)$ . The choice of not using the whole distribution but only a window centered on the corresponding extracted centroid is motivated by the fact that for high values of  $m_H$ , the covariance matrix encodes information also from the non-resonant tails at low reconstructed masses, yielding parameters that are non representative of the actual resonant shape of the signal. The definition of a window that mostly encloses the resonant part resolves this issue at high  $m_H$ , while mildly or not at all affecting the covariance matrix for other mass hypotheses. The diagonalization of the covariance matrix with a rotation angle  $\theta$  finally yields the parameters  $a$  and  $b$ , and  $\theta$  is taken to be the tilt angle of the ellipse. Figure 5.20 shows the distributions of these parameters as a function of the mass hypothesis ( $m_H, m_A$ ) for the  $\mu\mu$  and  $ee$  channels.

### 5.3.1.2. Ellipse size

At this point, each mass hypothesis is associated an ellipse which is well defined via the procedure defined above. The size of each ellipse comes inherently from the covariance matrix used to extract its parameters. This implies that each ellipse encloses all signal events that are contained roughly within one standard deviation of the corresponding mass distribution.

The extraction of the centroid of the ellipse relies on the signal 1D mass distributions being Gaussian, which is only an approximation since the distributions get more and more asymmetric as the value of the mass hypothesis increases. This might slightly shift the coordinates of the centroid. Therefore, the so-defined ellipse contains signal events within one standard deviation only in first approximation, and while using it to ultimately define the signal region is certainly a choice, a further optimization can be introduced to increase the

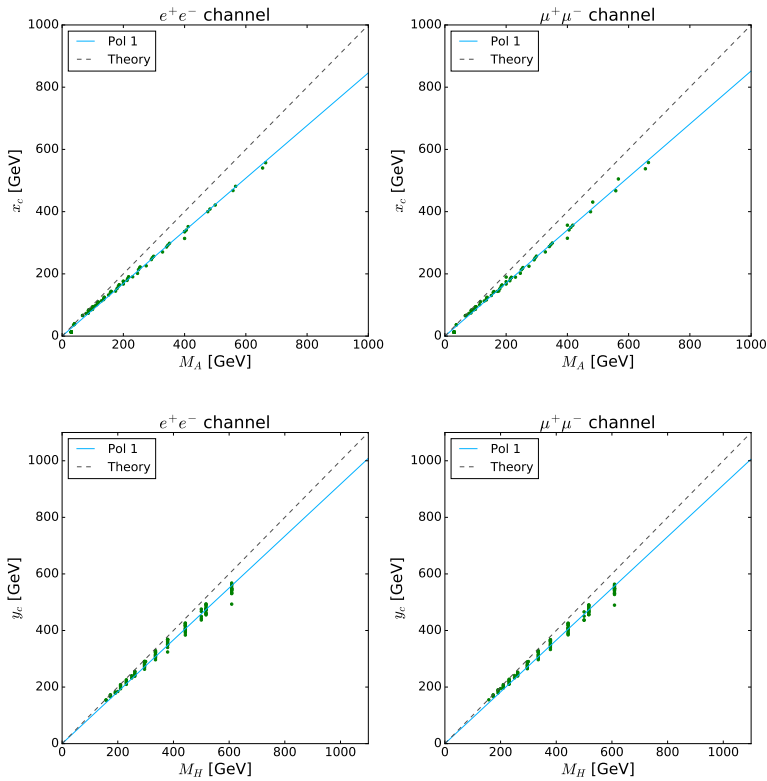


**Figure 5.19.** | Centroid coordinates well extracted from a Gaussian fit of the reconstructed mass distributions as a function of the mass hypothesis  $m_A$  (upper) and  $m_H$  (lower). The blue line represents the best-fit function, while the dashed line represents the theoretical scenario, where  $x_c = m_A$  and  $y_c = m_H$ .

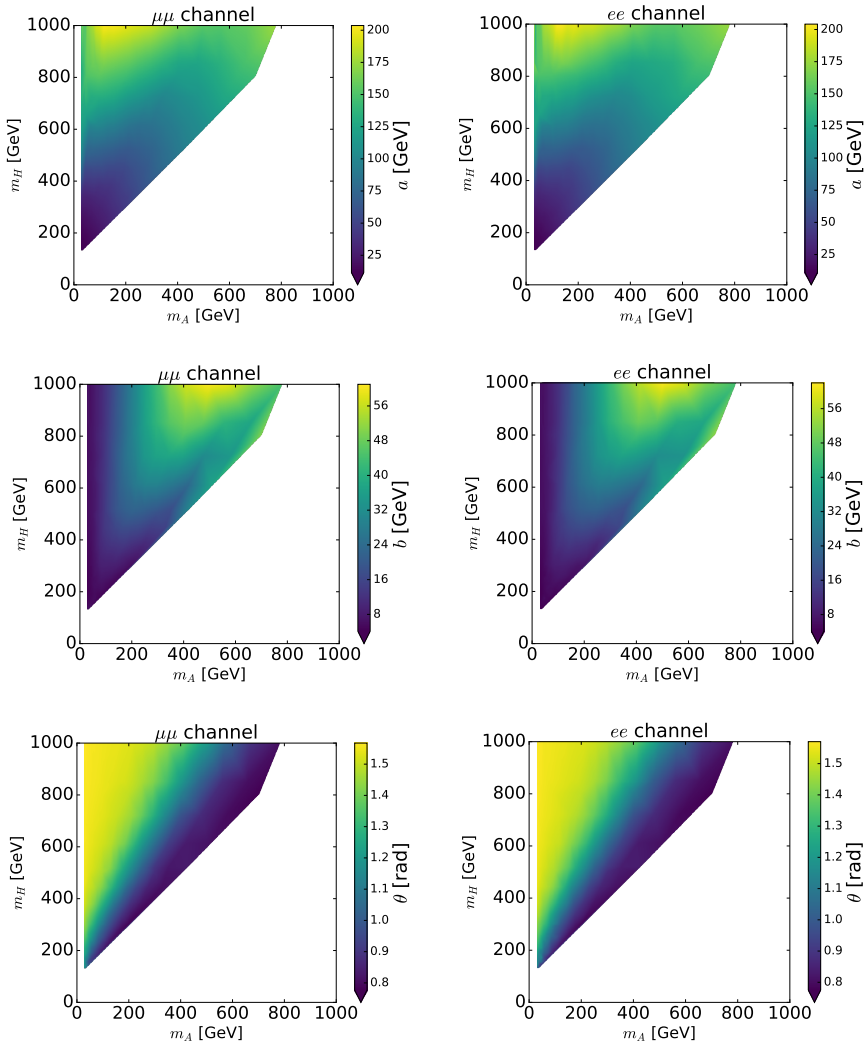


**Figure 5.20.** | Distribution of the ellipse major semi-axis (upper), minor semi-axis (middle), and tilt angle (lower) in the  $\mu\mu$  (left) and  $ee$  (right) channel as a function of the mass hypothesis ( $m_H$ ,  $m_A$ ).

acceptance of signal events.

The size of the ellipse is therefore represented by a parameter called  $\rho$ , defined such that ellipses with  $\rho = 1$  roughly contain events within one standard deviation of the corresponding signal distribution. This parameter is then varied from 0.0 to 3.0 in steps of 0.5, hence defining one ellipse and 5 concentric rings for each signal hypothesis. This is shown in Fig. 5.21 for the mass hypothesis  $(m_H, m_A) = (500, 300)$  GeV with the  $\mu\mu$  and  $ee$  channels summed together for illustrative purposes.

### 5.3.2. Final templates

At this stage, the signal region is fully defined via the selection requirements discussed in the previous sections, common to all signal hypotheses, and via elliptical cuts, specific to each hypothesis. The whole mass plane is therefore now covered with (concentric) ellipses, and a search for the H and A bosons can be performed.

In order to achieve this, for each hypothesis 6-bin histograms are filled with events falling inside each elliptical ring (or ellipse, in the case of  $\rho = 0.5$ ) shown in Fig. 5.21, for both data and simulation. Figure 5.22 shows the  $\rho$  distributions under three representative mass hypotheses for the  $\mu\mu$ ,  $ee$ , and  $\mu e$  channel. As expected, the signal is mostly contained at low values of the  $\rho$  parameter. We will refer to the  $\rho$  distributions as *final templates*. The Maximum Likelihood fit is simultaneously performed on the three channels. The reason why the  $\mu e$  channel is included in the statistical fit lies in the fact that it represents a control region rich in  $t\bar{t}$  events (with a minor contribution from Single top processes), and therefore a data-driven estimate of this background is obtained.

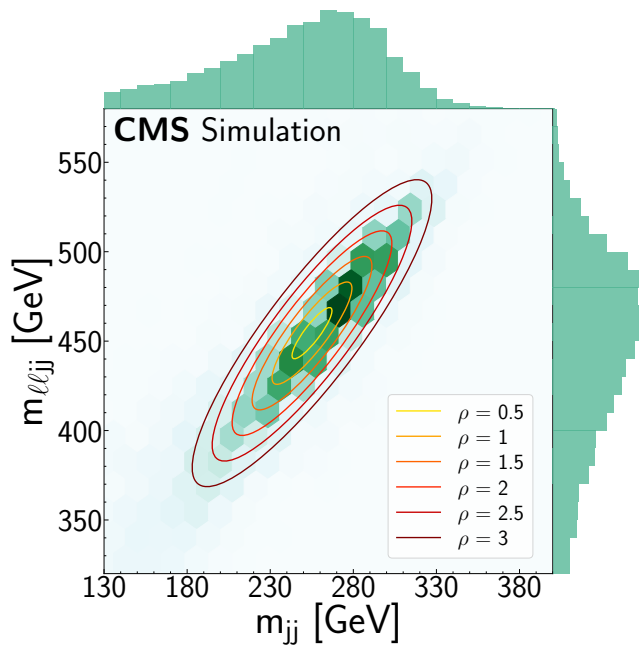


**Figure 5.21.** | Two-dimensional distribution of the reconstructed masses under the hypothesis  $(m_H, m_A) = (500, 300)$  GeV. The size of the ellipse is varied from 0 to 3 in steps of 0.5, hence defining one ellipse and 5 concentric rings. The  $\mu\mu$  and  $ee$  channels are summed together.

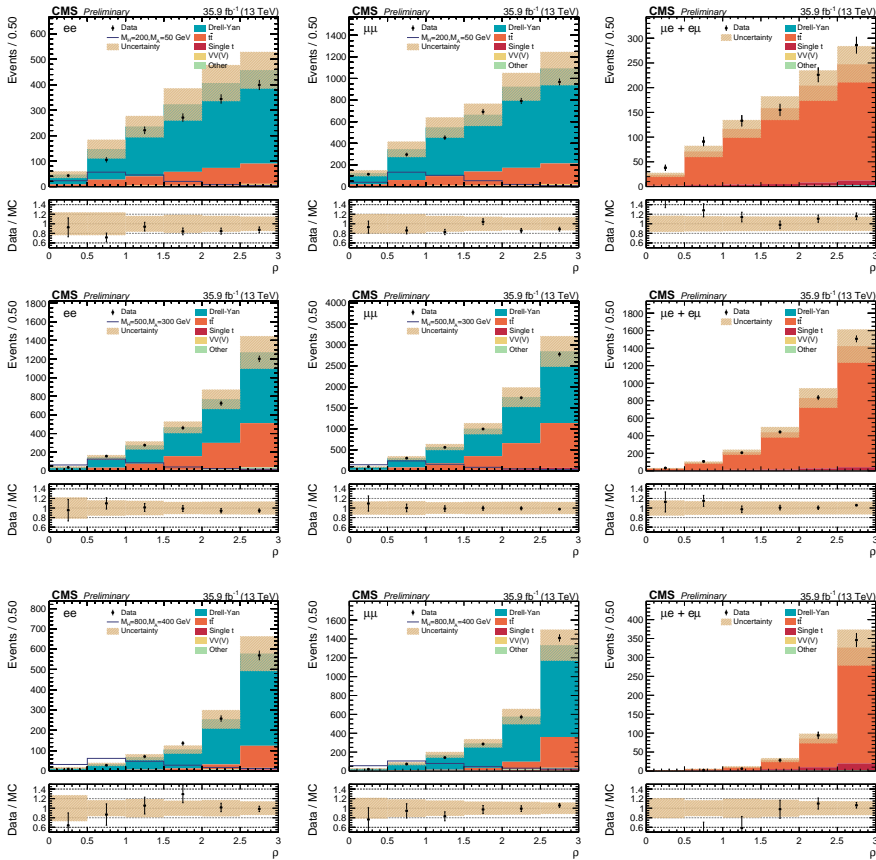


**Figure 5.22.** | Final templates for three representative signal hypothesis  $(m_H, m_A) = (200, 100)$  GeV (top),  $(m_H, m_A) = (500, 300)$  GeV (middle), and  $(m_H, m_A) = (800, 400)$  GeV (bottom) for  $ee$  (left),  $\mu\mu$  (middle), and  $\mu e$  (right) events. The signal is arbitrarily normalized.

## 5.4. DY reweighting

A good understanding and modeling of the background kinematic distributions is crucial when conducting a search, as already pointed out. In a control region defined by all the selection cuts as in the signal region defined in Section 5.3 but with no b tag requirement for the jets, that we will call *NB* control region, a discrepancy between data and MC simulation of up to 10% is observed in the invariant mass distributions  $m_{jj}$  and  $m_{\ell\ell jj}$  at low values of the reconstructed masses, as shown in Fig. 5.23a and 5.23b. This feature suggests the presence of a mismodeling of the DY + jets background in some specific regions of the mass plane, for instance in the so-called boosted region, where  $m_A$  is low and an increasing  $m_H$  transfers high  $p_T$  to the jets, that will appear as kinematically boosted.

To minimize the observed discrepancy, an event-by-event weight is mapped out from the NB region with a procedure defined as follows. The ratio data/MC of the  $m_{jj}$  ( $m_{\ell\ell jj}$ ) distribution is fitted with a polynomial function of 5<sup>th</sup> (6<sup>th</sup>) grade, that we will refer to as  $f_1$  ( $f_2$ ). Two weights can be extracted as:

$$w_{jj} = f_1(m_{jj}), \quad w_{\ell\ell jj} = f_2(m_{\ell\ell jj}). \quad (5.1.)$$

The event-by-event weight is defined as the product of these weights:

$$w_{DY} = w_{jj} \times w_{\ell\ell jj}, \quad (5.2.)$$

and it is applied to DY + jets events only. This procedure ensures a flat data/MC trend in the NB control region, as shown in Fig. 5.23c and 5.23d.

However, what observed in the NB control region does not trivially translate to the signal region. Indeed, the presence of heavy-flavor jets in the signal region implies different production modes and kinematics with respect to the light-flavor jets case. As a consequence, the above-described reweighting cannot be taken as a procedure to "correct" this background in all the regions of the phase space, since it is not guaranteed to provide the same correction as in the NB control region. Assuming that the accuracy of the MC model is similar in both the NB and the signal region, we go beyond the mere reweighting procedure by using  $w_{DY}$  to assign an uncertainty on the shape of the distributions. Specifically, the uncertainty is chosen to be 100% of the observed discrepancy and is considered as a source of systematic uncertainty for the DY + jets background. The nominal weight together with the up and down variations is reported in Table 5.2.

However, one must keep in mind that the shape and size of the signal region strongly depends on the width of the signal mass distributions: hence, at high masses the elliptical rings are large and can take up regions of the mass plane where the value of this uncertainty varies a lot. When the maximum likelihood fit (see Chapter 4) is performed, it is a possible scenario that regions falling

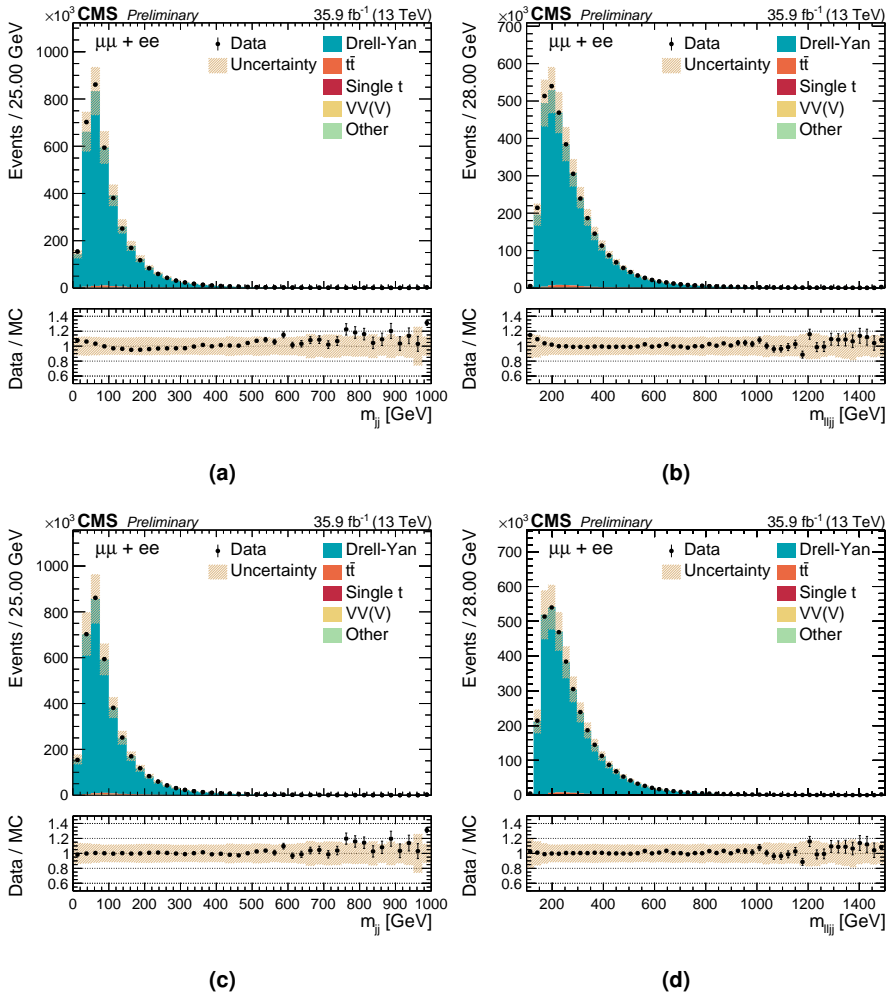


**Figure 5.23.** | Invariant mass distribution of the di-jet system (left) and of the  $\ell\ell jj$  system (right) in the NB control region without (upper) and with (lower) DY reweighting for SF events. Error bars indicate statistical uncertainty, while shaded bands indicate systematic uncertainties.

**Table 5.2.** | Summary of the event weight used to reweight DY + jets events together with its up and down variations, assigned as a source of systematic uncertainty.

Nominal	$w_{DY}$
Up variation	$ 1 - w_{DY} $
Down variation	$- 1 - w_{DY} $

inside the same elliptical ring and characterized by very different values of this uncertainty will constrain each other, effectively nullifying the purpose of introducing such uncertainty. Therefore, we face the risk that one global uncertainty might not be enough to properly take these differences in the mass plane into account.

The solution adopted is to uncorrelate this shape uncertainty across the mass plane. This is achieved by splitting the latter in 42 regions of approximately  $150 \times 150 \text{ GeV}^2$ , and assigning each region an independent uncertainty. This ensures that when the same elliptical ring encloses areas with different values of the DY uncertainty, the above-mentioned constraining effect is much reduced because of the presence of additional degrees of freedom in the maximum likelihood fit. The value of this shape uncertainty in the mass plane is plotted in Fig. 5.24, where the 42 regions, each with the associated uncertainty, are highlighted.

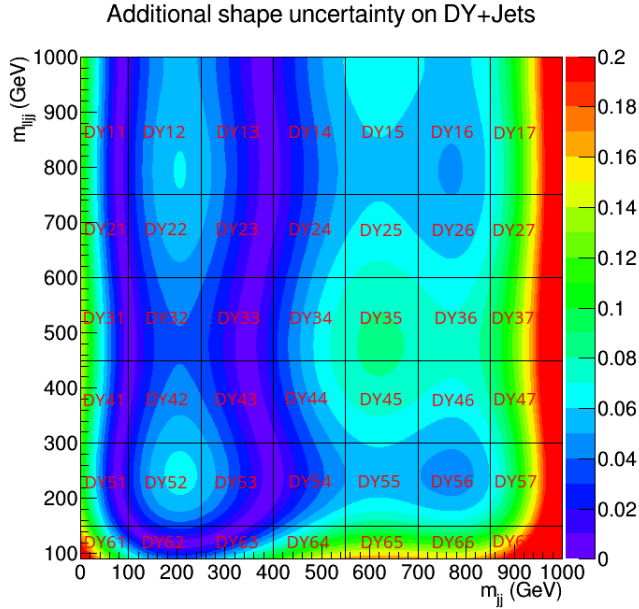


**Figure 5.24.** | Map of the 42 additional uncertainties applied to DY + jets events across the mass plane.

## 5.5. Systematic uncertainties

Background distributions are affected by sources of systematic uncertainties that are accounted for in the maximum likelihood fit and that can impact the sensitivity of the final result. A list of the sources of systematic uncertainties considered in this analysis is given below.

- **Luminosity.** The integrated luminosity for the analyzed data is measured to be  $35.9 \text{ fb}^{-1}$  with a relative uncertainty of 2.5%. Since each simulation sample is scaled by the luminosity, this represents an uncertainty on their normalization.
- **Background theoretical cross sections.** Each background is normalized to its theoretical cross sections to estimate the yields. The associated theoretical uncertainty is estimated by varying the process cross section by  $\pm 1\sigma$ .
- **Lepton identification and isolation.** Electrons and muons isolation and identification scale factors are extracted with the Tag & Probe technique [91], binned in the lepton  $p_T$  and  $\eta$ . Their effect on the analysis is estimated by varying these corrections by  $\pm 1\sigma$ .
- **Jet energy scale.** The jet energy scale is applied as a correction to the jet energy and its uncertainty is of the order of a few percent as a function of

the jet  $p_T$  and  $\eta$ . The uncertainty associated to it is obtained by varying the JES by  $\pm 1\sigma$ . In practice, 27 different sources of uncertainty are considered. These variations in jet energies are propagated to  $E_T^{\text{miss}}$ .

- **Jet energy resolution.** The jet energy resolution in simulation is worsened by about 10% to account for differences between data and simulation, the exact value depending on the jet  $\eta$ . The uncertainty associated to this is estimated by varying the JER by  $\pm 1\sigma$ . These variations in jet energies are propagated to  $E_T^{\text{miss}}$ .
- **Trigger efficiencies.** Trigger efficiencies are evaluated using the Tag & Probe technique [91] together with the associated uncertainties.
- **b tagging.** The b tagging efficiency and light-flavor mistag rate corrections are determined as a function of the jet  $p_T$  and  $\eta$ , and their effect on the analysis is estimated by varying these corrections by  $\pm 1\sigma$ .
- **Pileup.** The uncertainty associated to pileup reweighting is estimated by shifting the measured minimum-bias cross section by  $\pm 5\%$ .
- **$t\bar{t}$  shape uncertainty.** The uncertainty on the cross section of the  $t\bar{t}$  background is uncorrelated across the six bins of the final templates, such that more degrees of freedom are introduced in the Maximum Likelihood fit, yielding a more realistic data-driven estimate of this background.
- **DY shape uncertainty.** The DY + jets background is reweighted and the corresponding uncertainties are derived as explained in Section 5.4.
- **QCD scale uncertainty.** During MC generation, renormalization ( $\mu_R$ ) and factorization ( $\mu_F$ ) scales are used. The uncertainty from the fixed-order calculation is estimated by varying these values independently by a factor 0.5, 1, or 2. The cases where one scale fluctuates up while the other fluctuates down are not considered. Two envelopes are built from all the six possible variations by taking in each bin of the final template distribution the maximum and minimum variation, and are used as an estimate of the QCD scale uncertainties for all simulation samples.
- **Parton distribution functions (PDFs).** Each simulated process is generated with a given parton distribution function. The magnitude of the uncertainty associated to it and to the variation of the strong coupling constant is obtained using replicas of the nominal PDF set (NNPDF 3.0).
- **MC statistics.** The finite size of the MC simulation samples is considered to introduce systematic uncertainties. For each bin of the final template distributions, only the considered bin is altered by  $\pm 1\sigma$ , keeping the others at their nominal value.

The size of the event yield variation that these uncertainties introduce varies throughout the mass plane. However, it is common to the majority of the mass hypotheses that the major contribution comes from the QCD scale and jet

energy scale. The summary of the sources of systematic uncertainties and the variation that they induce on the event yields prior to the Maximum Likelihood fit for the dominant backgrounds and the signal is shown in Table 5.3 for the mass hypothesis  $(m_H, m_A) = (296, 68)$  GeV. The nuisance parameters that induce a yield variation of less than 0.1% are not displayed. It can be seen that, in this case, the most dominant contribution comes from the QCD scale.

A binned Maximum Likelihood fit on the final templates in the  $ee$ ,  $\mu\mu$ , and  $\mu e$  channels is performed in order to extract the best-fit signal cross sections. The best-fit values for all nuisance parameters as well as for the corresponding uncertainties are also extracted, as explained in Chapter 4. These are referred to as *post-fit* values.

After the Maximum Likelihood fit is performed, one can look at *impacts* and *pulls* to diagnose its behavior. The impact of a nuisance parameter  $\theta$  on the signal strength  $r$  is defined as the shift  $\Delta r$  that is induced as  $\theta$  is fixed and brought to its  $+1\sigma$  or  $-1\sigma$  post-fit values, with all the other nuisance parameters profiled as explained in Chapter 4. Impacts represent a useful tool for determining which nuisance parameters have the largest effect on the POI uncertainty. The *pull* of a nuisance parameter is instead defined as the variation of that parameter before and after the maximum likelihood fit normalized by the pre-fit uncertainty (for instance, a null pull means that the fit did not change the value of the corresponding nuisance parameter).

Since the probed mass range is large, nuisance parameters will yield different impacts depending on the considered mass hypothesis. For instance, in the case of the mass hypothesis  $(m_H, m_A) = (296, 68)$  GeV, the nuisance parameters with the highest impacts come from the statistical uncertainty due to the finite number of simulated events for the DY + jets background, JER, DY renormalization and factorization scales, and pileup. The full list is shown in the right panel of Fig. 5.25 for the first fifteen nuisance parameters, ranked from the highest impact to lowest. The left panel shows the pulls of these nuisance parameters. It can be seen that all of them are well within their pre-fit uncertainty.

**Table 5.3.** | Summary of the sources of systematic uncertainties and the variation, in percentages, that they induce on the total event yields prior to the Maximum Likelihood fit for the dominant backgrounds and the signal, corresponding to the mass hypothesis  $(m_H, m_A) = (296, 68)$  GeV.

Source	Background yield variation	Signal yield variation
Electron ID & ISO	2.7%	2.6%
Luminosity	2.5%	2.5%
Jet b-tagging (heavy)	2.5%	2.2%
Jet energy scale	1.8–1.9%	1.3%
Jet b-tagging (light)	1.0–1.1%	< 0.1%
Muon ID & ISO	0.6%	0.4%
Pileup	0.4%	0.6–1.0%
Trigger efficiency	0.1–0.3%	0.1–0.3%
Jet energy resolution	< 0.1%	0.2–0.4%
Affecting only $t\bar{t}$ (27.3% of the total bkg.)		
$\mu_R$ and $\mu_F$ scales	12.1–12.3%	
$t\bar{t}$ cross section	5.3%	
PDFs	0.7%	
Affecting only DY (69.2% of the total bkg.)		
$\mu_R$ and $\mu_F$ scales	9.8–10.4%	
DY cross section	4.9%	
MC statistics	1.3–2.7%	
DY_weight51	2.5–2.7%	
PDFs	0.8–1.0%	
DY_weight41	0.2%	
Affecting only VV (2.1% of the total bkg.)		
$\mu_R$ and $\mu_F$ scales	4.0–4.4%	
PDFs	0.5–0.7%	
Affecting only signal		
$\mu_R$ and $\mu_F$ scales		3.4–3.5%
PDFs		0.3–0.4%

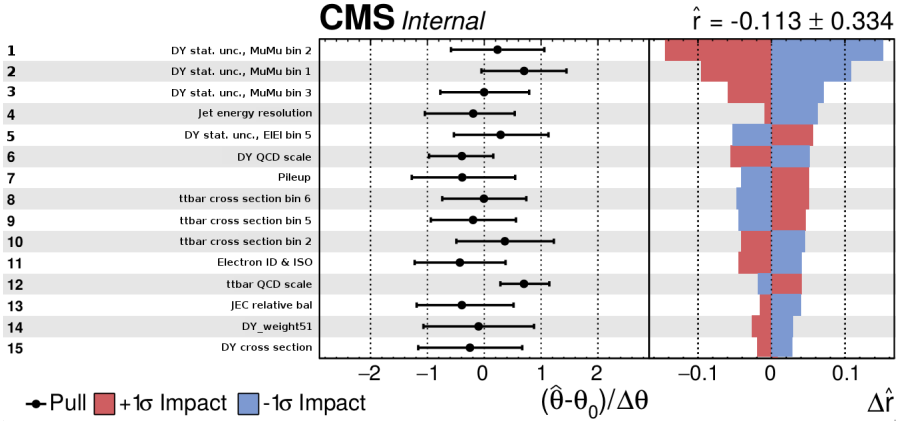


**Figure 5.25.** | Pulls (left panel) and impacts (right panel) for ten nuisance parameters ranked from highest impact to lowest corresponding to the mass hypothesis  $(m_H, m_A) = (296, 68)$  GeV.

## 5.6. Results

The generation of simulation samples demands time and computational resources, and a choice has to be made on the number of samples that one needs for the search. In the case of this analysis, only 207 signal samples of 100,000 events each were produced to perform a *scan* of the mass plane. In order to spot possible signals that might escape observation because of an insufficient resolution of this scan,  $\sim 900$  ellipses were parametrized and the p-value was computed for each of them. The result is shown in Fig 5.26.

The maximum observed local significance is  $3.9\sigma$  for the signal hypothesis with  $(m_H, m_A) = (627, 162)$  GeV. This can be seen in Fig. 5.27, that shows the post-fit  $\rho$  distributions for the  $ee$  and  $\mu\mu$  channel. However, this globally becomes  $1.3\sigma$  once accounting for the look-elsewhere effect [95], which needs to be estimated in two dimensions in the case of this analysis, given that two parameters are defined under the alternative hypothesis. The procedure used to quantify the LEE is addressed in Section 5.7.

A smaller excess of events emerges from the p-value scan corresponding to the mass hypothesis  $(m_H, m_A) = (371, 57)$  GeV, yielding a local significance of  $3.1\sigma$ . This is shown in Fig. 5.28.

### 5.6.1. Upper limits and interpretation in Type-II 2HDM

The upper limits are computed using the asymptotic CLs method, combining the  $ee$  and  $\mu\mu$  channels.

As anticipated at the beginning of this chapter, the search has been conducted for  $H \rightarrow ZA$  only. At this stage, the two theoretical masses are interchanged to allow coverage of the mass plane for the process  $A \rightarrow ZH$ . Model independent

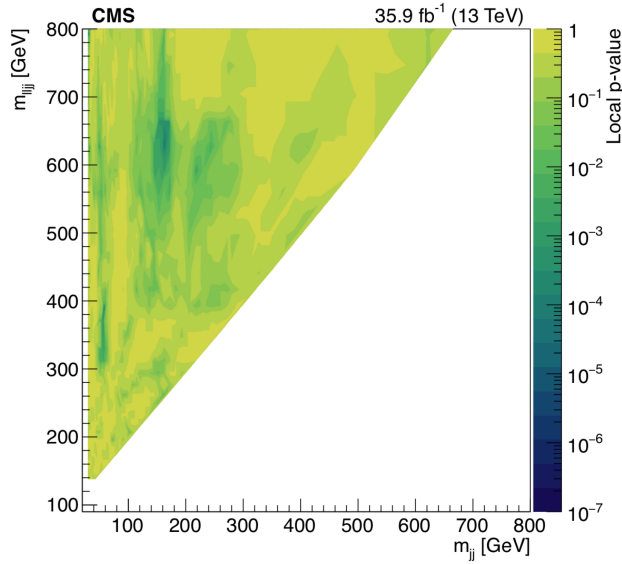


Figure 5.26. | P-value scan in the mass plane calculated on  $\sim 900$  ellipses.

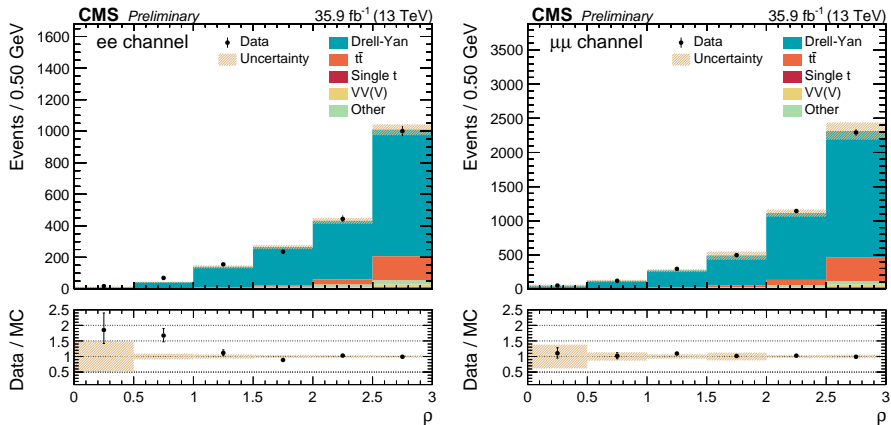
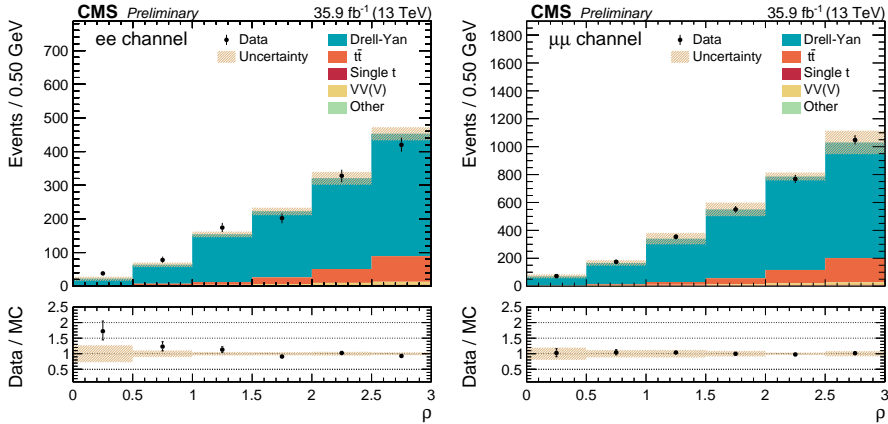


Figure 5.27. | Final templates for the mass hypothesis  $(m_H, m_A) = (627, 162)$  GeV in the  $ee$  (right) and  $\mu\mu$  (left) channels. The shaded bands indicate post-fit uncertainties.



**Figure 5.28.** Final templates for the mass hypothesis  $(m_H, m_A) = (371, 57)$  GeV in the  $ee$  (right) and  $\mu\mu$  (left) channels. The shaded bands indicate post-fit uncertainties.

upper limits at 95% CL on the product of the signal production cross section and branching ratio for  $H(A) \rightarrow ZA(H) \rightarrow \ell^+ \ell^- b\bar{b}$  ( $\sigma_{obs}$  for shortness) are set in the mass plane as a function of the mass hypotheses  $m_H$  and  $m_A$ . These are reported in Fig. 5.29. The region marked with "unexplored" in this figure is not kinematically allowed for an on-shell Z boson.

These results are interpreted in the context of the Type-II 2HDM for the theoretical benchmark  $\tan\beta = 1.5$  and  $\cos(\beta - \alpha) = 0.01$ . Here,  $\sigma_{obs}$  is compared to the theoretical cross section multiplied by the theoretical branching ratio ( $\sigma_{th}$ ) shown in Fig. 5.3 (left). This allows the regions of the 2HDM parameter space to be determined which are incompatible with the observed cross section, and can therefore be excluded. Figure 5.30 shows the excluded region at 95% CL, indicated with a gray area, in the mass parameter space. Under the benchmark conditions, the scalar H and the pseudoscalar A are excluded for masses ranging from  $\sim 200$  GeV to  $\sim 700$  GeV.

Similarly, results for one particular mass point can be re-casted in a different parameter space. In this case, we consider the  $\cos(\beta - \alpha)$  vs.  $\tan\beta$  plane for the benchmark  $m_H = 379$  GeV,  $m_A = 172$  GeV. The corresponding theoretical cross section is shown in Fig. 5.3 (right). The excluded region is delimited by the gray area in Fig. 5.31: values of  $\cos(\beta - \alpha)$  ranging from approximately  $-0.9$  to  $0.3$  and of  $\tan\beta$  from approximately  $0.5$  to  $7.0$  can be excluded at 95% CL [116].

## 5.6.2. Discussion

It is here worth remarking that the excesses shown in Figs. 5.27 and 5.28 appear only for  $ee$  events, while a good agreement of the data with the simulated backgrounds is observed in the  $\mu\mu$  channel. This "asymmetry" makes the

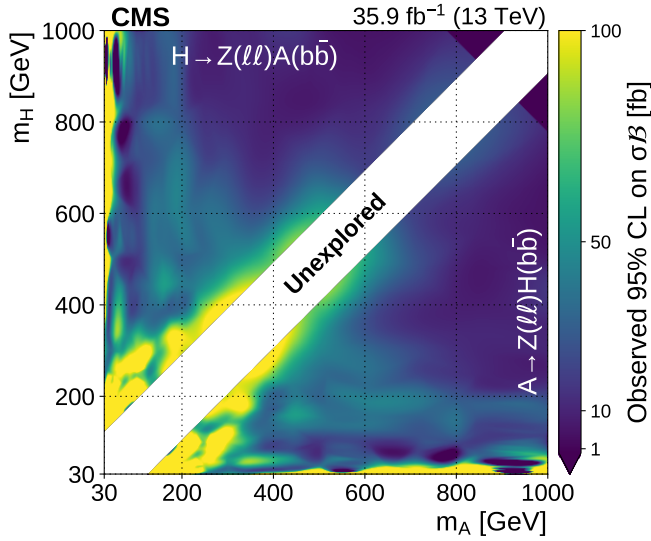


**Figure 5.29.** | Observed 95% CL upper limits on the product of the production cross section and branching ratio for  $H(A) \rightarrow Z A (H) \rightarrow \ell^+ \ell^- b \bar{b}$  as a function of  $m_A$  and  $m_H$ .

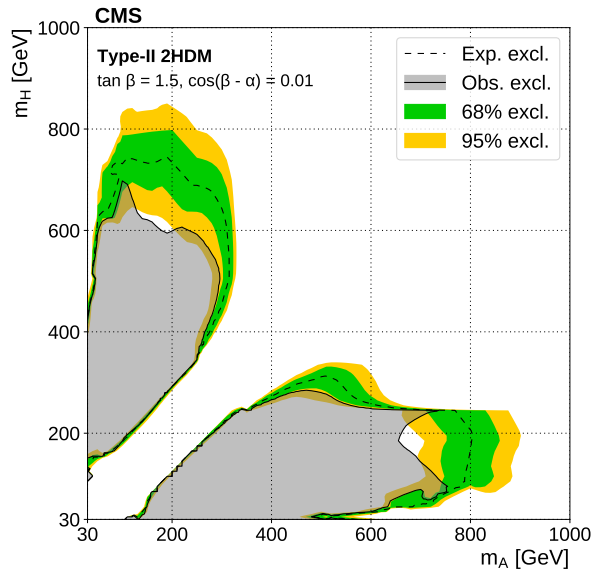


**Figure 5.30.** | Expected (with  $\pm 1, \pm 2$  standard deviation bands) and observed 95% CL upper limits on the quantity  $\sigma_{obs}/\sigma_{th}$  for the Type-II 2HDM benchmark  $\tan\beta = 1.5$  and  $\cos(\beta - \alpha) = 0.01$  as a function of  $m_A$  and  $m_H$ .

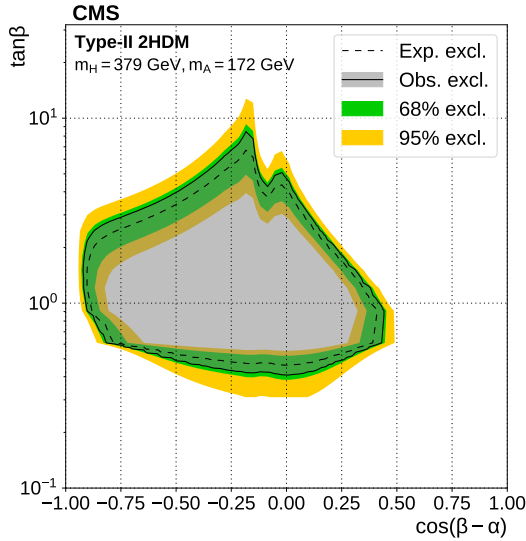


**Figure 5.31.** | Expected (with  $\pm 1, \pm 2$  standard deviation bands) and observed 95% CL upper limits on the quantity  $\sigma_{obs}/\sigma_{th}$  for the Type-II 2HDM benchmark  $m_H = 379 \text{ GeV}$  and  $m_A = 172 \text{ GeV}$  as a function of  $\cos(\beta - \alpha)$  and  $\tan\beta$ .

significance of the excess questionable: an excess of  $ee$  events with respect to  $\mu\mu$  events would imply a branching ratio of  $Z \rightarrow ee$  higher than  $Z \rightarrow \mu\mu$ , which is highly disfavored by the *lepton universality* [117]. This property holds between the first two lepton families with a precision of better than 0.3% in  $Z$  boson decays<sup>1</sup> [118]. However, it is not excluded that an excess of such type might also be a real excess with the events in the  $\mu\mu$  channel down-fluctuating, and in this case the LEE plays a crucial role to determine its global significance. Bearing this in mind, one could further investigate the nature of a possible excess encountered in a search. The signal cross section for the mass hypothesis yielding a high significance can be used to constrain the 2HDM parameter space, narrowing it down to allowed regions where new physics would lie if the excess was actually to come from new resonances with masses equal the mass hypothesis.

The signal cross section is extracted with a Maximum Likelihood fit for both the mass hypotheses yielding an excess in this analysis, as well as the theoretical cross section in the  $\cos(\beta - \alpha)$  vs.  $\tan\beta$  plane in the Type-II 2HDM benchmark. This can be seen in Fig. 5.32: on the left (right) is the plane under the mass hypothesis that yields a  $3.9\sigma$  ( $3.1\sigma$ ) excess. The dashed line represents the

<sup>1</sup> Some tensions with SM prediction have emerged in recent measurements in decays of B hadrons [118, 119], however this is not further discussed as it goes beyond the scope of this thesis.

contour where the cross section from the Maximum Likelihood fit equals the theoretical one, while the solid lines represent its  $\pm 1\sigma$  variations. In the case of the mass hypothesis  $(m_H, m_A) = (627, 162)$  GeV (left), the fit returns a cross section which is too high for the theoretical model, and what is shown is only its down variation. This excess would then be only marginally compatible with the Type-II 2HDM hypothesis.

More interesting is instead the case of  $(m_H, m_A) = (371, 57)$  GeV (right). The region in between the solid lines represents the region of the parameter space compatible with the excess that this mass hypothesis brings up. Here, when restricting the space to the alignment limit only ( $\cos(\beta - \alpha) = 0$ ), possible values for  $\tan\beta$  would lie in the ranges  $[0.23, 0.24]$  and  $[3, 10]$ . It is important to stress here that the nature of this discussion is purely general and it has the sole purpose of discussing a possible way of interpreting a possible excess encountered in an analysis. The origin of an excess of events with a significance of  $3\sigma$  might lie in mere statistical fluctuations as well as in new physics that has not emerged yet because of lack of sensitivity. In this last case, the range of values extracted as mentioned above is useful to constrain the Type-II 2HDM parameter space to regions allowed by the presence of such excess. Moreover, the hypothesis of new physics is not refuted if the found allowed range has not been excluded by previous searches (although this does not represent by any means a proof of its existence). The nature of such excess is then certainly worth investigating further by refining the data analysis techniques and conducting the search on data collected at a higher luminosity, in order to gain an enhancement in sensitivity. Only then one will be able to shed light on the origin of the excess, either confirming or disproving the hypothesis of a statistical fluctuation.

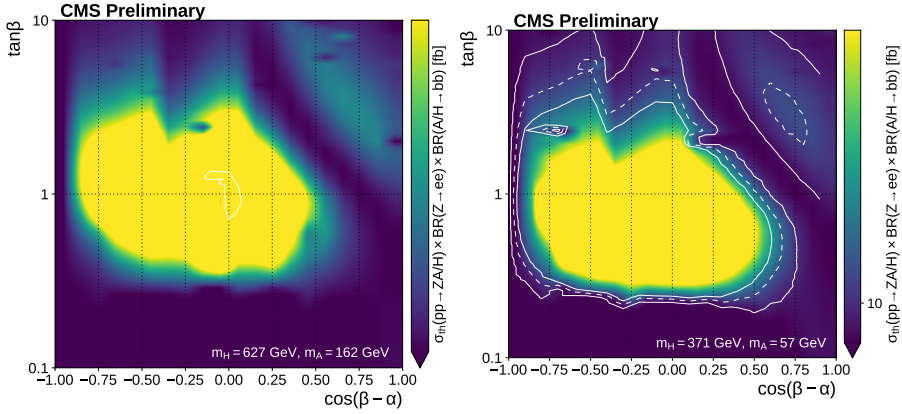


**Figure 5.32.** | Theoretical cross sections in the  $\cos(\beta - \alpha)$  vs.  $\tan\beta$  plane in the Type-II 2HDM benchmark for the  $(m_H, m_A) = (627, 162)$  GeV (left) and  $(m_H, m_A) = (371, 57)$  GeV (right). The dashed line represents the contour where the cross section extracted from the Maximum Likelihood fit equals the theoretical one, while the solid lines represent its  $\pm 1\sigma$  variations.

## 5.7. Estimating the LEE in 2D

In the case of the  $H \rightarrow ZA$  search, two parameters,  $m_H$  and  $m_A$ , are defined under the alternative hypothesis. This makes the estimation of the LEE a two-dimensional problem.

The general procedure to obtain the global p-value is described in Section 4.1.5. It is briefly recalled here that the global p-value depends on two coefficients  $N_1$  and  $N_2$  that are estimated through the expectation values of the Euler characteristic at two arbitrarily chosen thresholds  $u_0$  and  $u_1$  (see Eq. 4.15). In order to obtain these expectation values, background toys are needed.

Toys represent random statistical fluctuations in the data, and are used as replacement of the real data when computing the test statistic in Eq. 4.4 under the background-only hypothesis. They are estimated from the background distributions in the mass plane. In this analysis, the most dominant background contributions come from  $DY + \text{jets}$  and  $t\bar{t}$ , and only these two backgrounds are therefore considered in the toy generation. Indicating with  $n$  the desired number of toys, we need to generate  $n$  different statistically independent mass planes all drawn from the  $DY + t\bar{t}$  2D distribution (which we will refer to as *nominal distribution* in this section). For each toy, final templates are then built with the same  $\sim 900$  ellipses used for the p-value scan.

For explanatory purposes, let us consider only one toy. This will look like a 2D distribution of events randomly sampled from the nominal background distribution according to its shape. The normalization is instead determined from data. Then, for one mass hypothesis, the corresponding template has to

be built. This is achieved by filling the  $\rho$  histograms (see Fig. 5.22 for reference) with events falling in the six concentric elliptical rings. Therefore, it is crucial that the nominal distribution in the mass plane is as smooth as possible, in order to guarantee a realistic construction of the final template.

### 5.7.1. Background smoothing: a "customized" KDE

In order to smooth the background, a "customized" Gaussian Kernel Density Estimator (KDE) [120] is used. The KDE is a fundamental data smoothing problem where inferences about the population are made, based on a finite data sample. Indicating with  $(x_1, x_2, \dots, x_k)$  an independent and identically distributed sample drawn from some distribution with an unknown density  $f$ , the (Gaussian) smoothing occurs via centering a Gaussian function with variance  $\sigma$  around each point  $x_i$ , called *observation*, and then summing all the Gaussian distributions together. An illustration of this is shown in Fig. 5.33, where a sample of points is smoothed with a Gaussian Kernel. Mathematically, the Gaussian KDE  $\hat{f}(x)$  is given by:

$$\hat{f}(x) = \sum_{\text{observations}} K\left(\frac{x - \text{observation}}{\text{variance}}\right) \quad (5.3.)$$

where  $K$  is the Gaussian kernel.

Since in the case of this analysis the background distribution lies in a two-dimensional space, the Gaussian kernel used for the smoothing must be two-dimensional as well. The general equation for a 2D Gaussian function with unitary amplitude is given by:

$$f(x) = \exp(-(\lambda_1(x - x_0)^2 + 2\lambda_2(x - x_0)(y - y_0) + \lambda_3(y - y_0)^2)) \quad (5.4.)$$

where  $x_0$  and  $y_0$  are the coordinates of its center, and  $\lambda_1$ ,  $\lambda_2$ , and  $\lambda_3$  are three coefficients defined as:

$$\begin{aligned} \lambda_1 &= \frac{\cos^2 \xi}{2\sigma_x^2} + \frac{\sin^2 \xi}{2\sigma_y^2}, \\ \lambda_2 &= -\frac{\sin 2\xi}{4\sigma_x^2} + \frac{\sin 2\xi}{4\sigma_y^2}, \\ \lambda_3 &= \frac{\sin^2 \xi}{2\sigma_x^2} + \frac{\cos^2 \xi}{2\sigma_y^2} \end{aligned} \quad (5.5.)$$

Here,  $\sigma_x^2$  and  $\sigma_y^2$  are the variances along the x and y-axis, respectively, and  $\xi$  is the tilt angle of the Gaussian with respect to the y-axis. For the Gaussian kernel used in this analysis, for a given point  $(m'_{jj}, m'_{\ell\ell jj})$  of the background distribution, the following parameters are used:

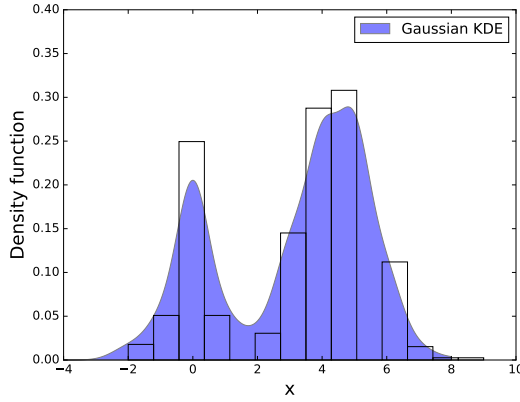


**Figure 5.33.** | Example of Gaussian kernel density estimator, represented by the area in purple, of the distribution of an observable  $x$ .

$$\begin{aligned}
 x_0 &= m'_{jj}, \\
 y_0 &= m'_{\ell\ell jj}, \\
 \sigma_X &= b, \\
 \sigma_Y &= a, \\
 \xi &= \frac{\pi}{2} - \theta
 \end{aligned}
 \tag{5.6}$$

with  $a$ ,  $b$ , and  $\theta$  parameters of an ellipse centered in  $(m'_{jj}, m'_{\ell\ell jj})$  interpolated from the already existing parameter map. In other words, an elliptical smoothing directly related to the resolution of the signal in the mass plane is applied. In practice, points are "thrown" in a Gaussian fashion according to Eq. 5.4 around each event of the background distribution in the mass plane. The weight of each point is rescaled by the number of thrown points to ensure the correct normalization. Then, a finely binned 2D histogram is filled, from which the toys are subsequently sampled. Figure 5.34 shows the comparison between the nominal 2D histogram and the smoothed one only for the  $DY + 2\text{jets}$  sample, for illustrative purposes.

### 5.7.2. Quantification of the LEE

After the smoothed 2D histogram is built, toys can be generated by sampling from the bins of the smoothed histogram according to the associated bin content. For this analysis, 15 toys are generated. Figure 5.35 shows three different generated toys in the  $ee$  and  $\mu\mu$  channels for the mass point  $(m_H, m_A) = (652, 64)$  GeV. It can be seen how statistical fluctuations are introduced in each bin.

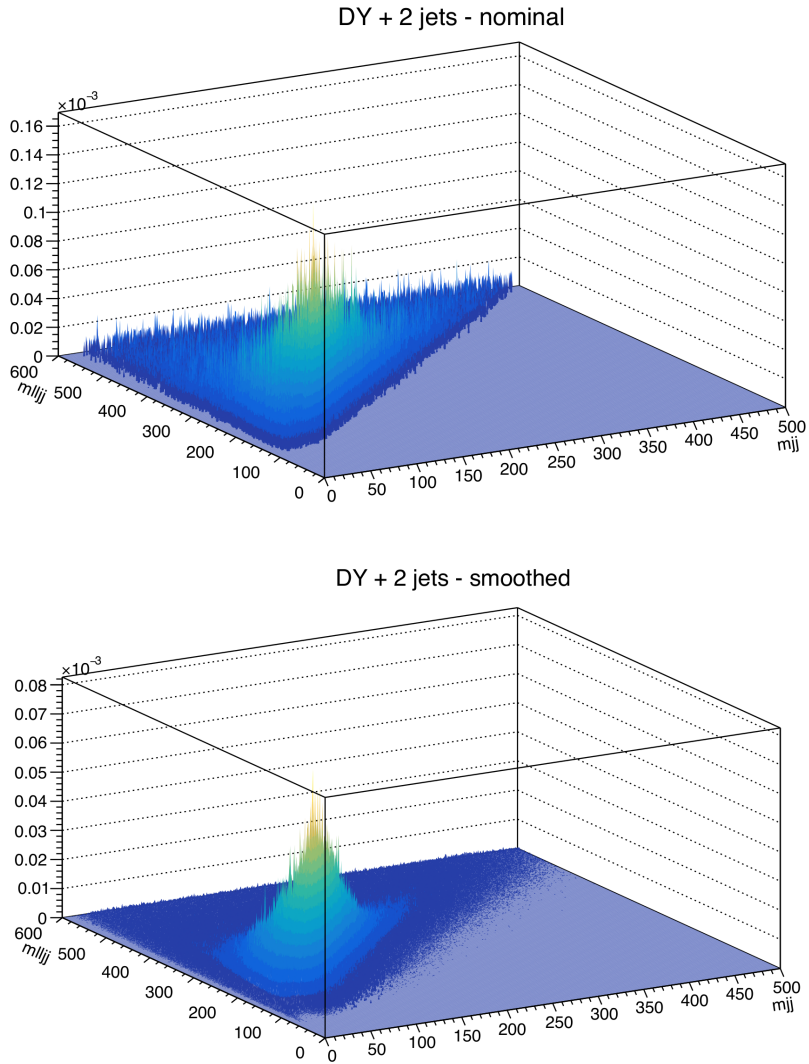


**Figure 5.34.** | Nominal (upper) and smoothed (lower) histogram for the DY + 2jets background sample.

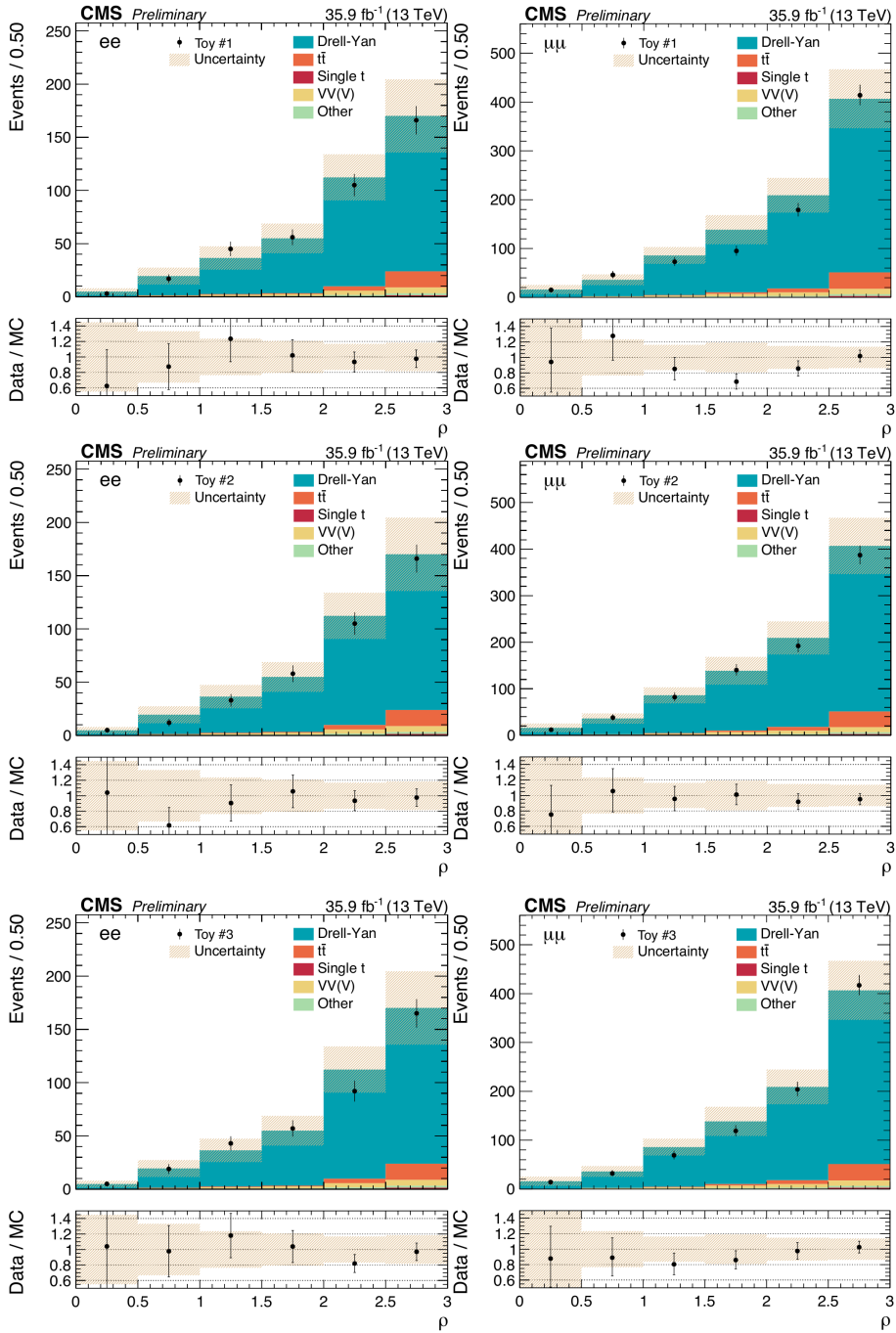


**Figure 5.35.** | Final templates with background toys instead of the real data. The rows show histograms with three different toys, while the columns show the  $ee$  and  $\mu\mu$  channels. All histograms are relative to the mass point  $(m_H, m_A) = (652, 64)$  GeV.

With  $\sim 900$  signal regions covering the mass plane, the LEE can now be quantified. The thresholds  $u_0$  and  $u_1$  introduced in Section 4.1.5 are chosen to be 0.1 and 1.0, respectively, but this choice does not matter if the number of toys is sufficiently high. The chosen number of toys is enough to guarantee this.

The test statistic  $q_0$  of Eq. 4.9 for two mass parameters is calculated for each mass point and then interpolated in the mass plane. This is shown in the first column of Fig. 5.36 for three representative toys. The second and third column of the figure represent the intersection of the  $q_0$  distribution at thresholds 0.1 and 1.0, respectively. The blue areas correspond to regions where  $q_0$  is above the indicated threshold. The expectation values of the Euler characteristic are found to be  $\mathbb{E}[\phi(A_{0.1})] = 13$  and  $\mathbb{E}[\phi(A_{1.0})] = 27$ . With these numbers, the global significance can be computed. This amounts to  $1.3\sigma$ , which is much lower than the local  $3.9\sigma$  previously observed, with a trial factor of  $\sim 800$ . This result marks the observed excess as non statistically significant.

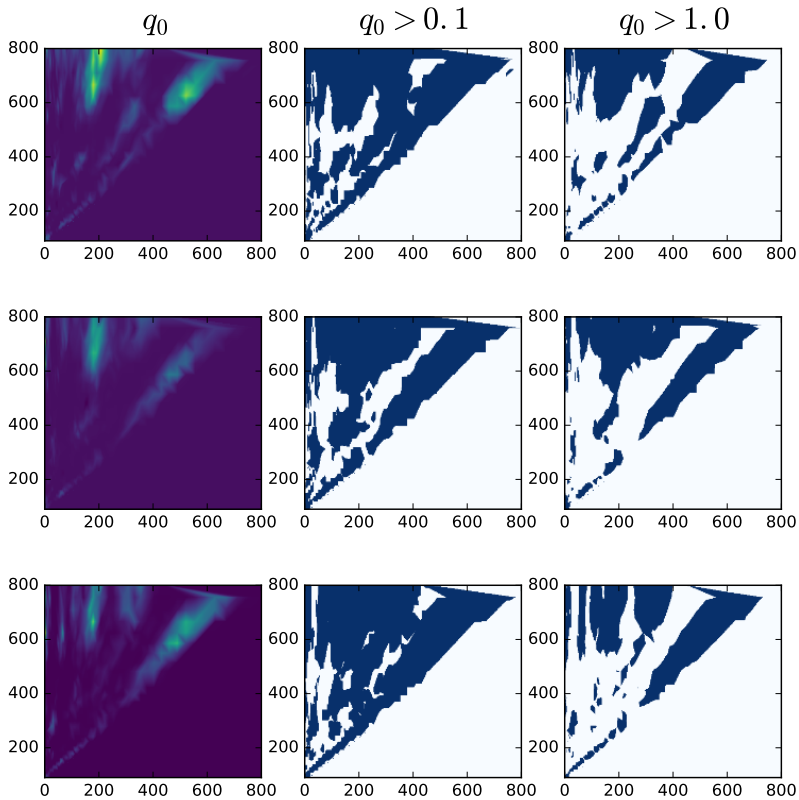


**Figure 5.36.** | Distribution of the test statistic  $q_0$  (left) intersected with the thresholds 0.1 (middle) and 1.0 (right). Each row shows the results from one toy. The blue areas correspond to regions where  $q_0$  is above the indicated threshold.

## 5.8. Comparison with previous searches

Another point worth of attention is how the results presented in this chapter compare to existing results from previous searches performed by the CMS and ATLAS Collaborations. In particular, we will comment on the comparison with two searches conducted by the CMS Collaboration, one at  $\sqrt{s} = 8$  TeV and  $\mathcal{L} = 19.8 \text{ fb}^{-1}$  [114] and one at  $\sqrt{s} = 13$  TeV and  $\mathcal{L} = 2.3 \text{ fb}^{-1}$  [4], and the search performed by the ATLAS Collaboration at  $\sqrt{s} = 13$  TeV and  $\mathcal{L} = 36.1 \text{ fb}^{-1}$  [121]. The main feature of the analysis strategy adopted by the CMS searches is the definition of a rectangular signal region around each mass hypothesis in the reconstructed mass plane  $m_{jj}$  vs.  $m_{\ell\ell jj}$ , where the size of the rectangle is set to three times the experimental resolution. A cut & count approach is used to set upper limits on the product of the signal production cross section and branching ratio. In this perspective, the analysis presented in this chapter is an optimization of these searches: the definition of an elliptical signal region instead of a rectangular one makes it possible to roughly keep the same number of signal events while discarding more background events; the binning of the mass plane in concentric ellipses allows simultaneous fitting of the regions containing the signal and of regions where the signal is very low or null and the background contribution is high (roughly first three and last three bins of the final templates, respectively), allowing better constraining of the background nuisance parameters. Both these two points contribute to improving the sensitivity of the search at  $\mathcal{L} = 35.9 \text{ fb}^{-1}$  with respect to the previous ones. The search at  $\sqrt{s} = 8$  TeV in the  $\ell\ell bb$  final state was also combined with the  $\ell\ell\tau\tau$  final state to increase the exclusion power. The exclusion plots in the 2HDM parameter space are shown in Figs. 5.37a and 5.37b and should be compared with Figs. 5.30 and 5.31, respectively. A moderate excess with a local significance of  $2.6\sigma$  was observed at  $(m_H, m_A) = (285, 95)$  GeV and is visible in Fig. 5.37a, where the point is not excluded. The improved sensitivity of the search presented in this chapter allows for exclusion of that mass point at 95% CL, classifying the excess as a statistical fluctuation. The exclusion contours at  $\tan\beta = 1.5$  (and more generally low values of  $\tan\beta$ ) are limited in both analyses at  $m_A \approx 350$  GeV, as the threshold for  $t\bar{t}$  production opens and the branching ratio  $A \rightarrow t\bar{t}$  becomes sizable.

Regarding the  $\cos(\beta - \alpha)$  vs.  $\tan\beta$  parameter space, a much larger region can now be excluded with respect to the previous search for a very similar mass point benchmark (Fig. 5.37b).

The results of the search at  $\sqrt{s} = 13$  TeV and  $\mathcal{L} = 2.3 \text{ fb}^{-1}$  were not combined with the  $\ell\ell\tau\tau$  final state. The upper limits from this search and from the search presented in this chapter are shown in Figs. 5.38a and 5.38b, respectively, for three representative mass hypotheses:  $m_H = 300$  GeV and  $m_A = 50, 100, 200$  GeV. An improvement in the sensitivity is expected from the fact that the most recent

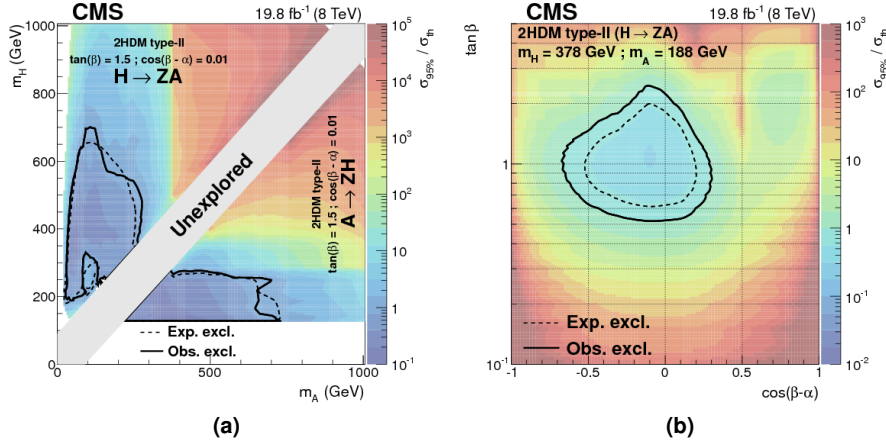


**Figure 5.37.** | Expected and observed 95% CL upper limits on the quantity  $\sigma_{obs}/\sigma_{th}$  for the Type-II 2HDM benchmark  $\tan\beta = 1.5$  and  $\cos(\beta - \alpha) = 0.01$  as a function of  $m_A$  and  $m_H$  (a) and  $(m_H, m_A) = (378, 188)$  GeV as a function of  $\cos(\beta - \alpha)$  and  $\tan\beta$  (b) [114].

data sample analyzed has higher integrated luminosity and from the optimized analysis strategy. This can be seen in the fact that current limits are lower than the previous ones by up to a factor 10.

The ATLAS Collaboration carried out the search for the pseudoscalar  $A$  via the cascade decay  $A \rightarrow Z(\rightarrow \ell^+ \ell^-)H(\rightarrow b\bar{b})$  in the alignment limit and in the mass range  $m_A < 800$  GeV. A cut on the  $m_{jj}$  invariant mass is used in the definition of the signal region to ensure compatibility with the assumed  $H$  boson mass and in general slightly tighter cuts are applied to the kinematic observables. Two categories are defined through the  $b$  jet multiplicity  $n_b$  to take into account both the contributions from gluon-gluon fusion ( $n_b = 2$ ) and from  $b$ -associated production ( $n_b \geq 3$ ), while we do not consider the contribution from the latter, as it is sub-dominant at low  $\tan\beta$ . The normalization of the  $t\bar{t}$  and  $DY + jets$  backgrounds are determined from control regions, and similar working points are used for the  $b$  tagging in both the analyses. A template defined by the binned invariant mass of the  $\ell\ell jj$  object is used for the Maximum Likelihood fit. While the upper limits on the product of the signal production cross section and branching ratio  $BR(A \rightarrow ZH) \times BR(H \rightarrow b\bar{b})$  are set separately for gluon-gluon fusion (Fig. 5.39a) and  $b$ -associated production, a new signal model weighted by the predicted cross sections of the two processes is built and upper limits are compared with predictions from the Type-II 2HDM (Fig. 5.39b). While the observed upper limits show similar sensitivity as the limits we set (Fig. 5.29), a difference can be observed in the exclusion contours. Because of the 2HDM phenomenology, at low  $\tan\beta$  the gluon-gluon fusion production via top quark loop dominates, while the contribution from  $b$ -associated production becomes

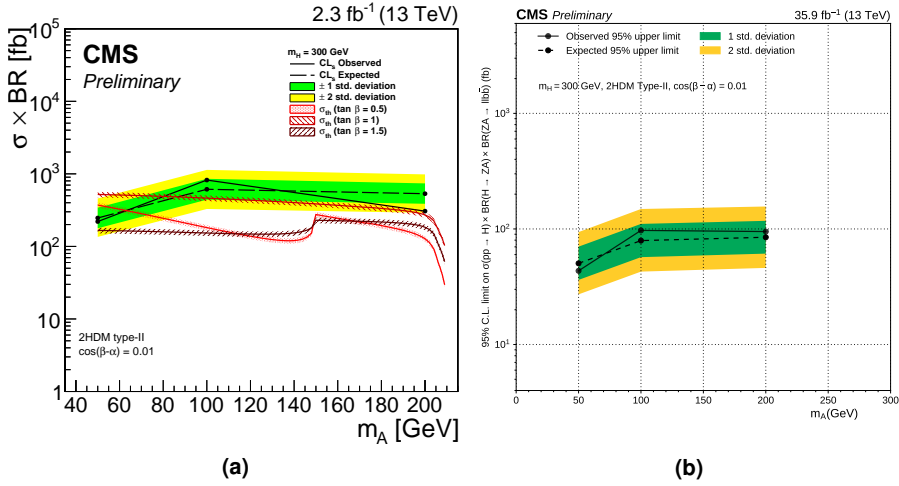


**Figure 5.38.** | Expected and observed 95% CL upper limits on the product of the signal production cross section and branching ratio  $\text{BR}(H \rightarrow ZA) \times \text{BR}(A \rightarrow b\bar{b}) \times \text{BR}(Z \rightarrow \ell^+ \ell^-)$  for three representative mass hypotheses  $m_H = 300 \text{ GeV}$  and  $m_A = 50, 100, 200 \text{ GeV}$  from the search at  $\mathcal{L} = 2.3 \text{ fb}^{-1}$  (a) and  $\mathcal{L} = 35.9 \text{ fb}^{-1}$  (b) [4].

dominant at high  $\tan\beta$ . It is seen that the exclusion reaches up to  $m_H \approx 400 \text{ GeV}$  at low  $\tan\beta$  ( $< 10$ ) and  $m_H \approx 600 \text{ GeV}$  at high  $\tan\beta$  ( $= 20$ ). This shows that a separate handling of the b-associated production mode should be included in the analysis on the full Run 2 dataset in order to increase the exclusion power at high values of  $\tan\beta$ .

Finally, a difference in the scanned mass range is to be highlighted: we set limits also at small values of  $m_H$  (starting from  $30 \text{ GeV}$ ), while in the ATLAS search the interpretation of the results in the 2HDM is performed starting from  $m_H = 130 \text{ GeV}$ . This makes our results more interesting to study the mechanism of electroweak baryogenesis, that is favored by a large splitting between the values of  $m_A$  and  $m_H$  [122].

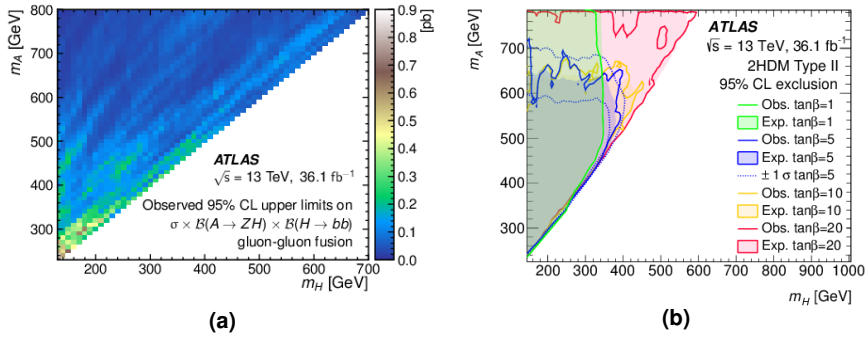


**Figure 5.39.** | Observed 95% CL upper limits on the product of the signal production cross section and branching ratio  $\mathcal{B}(A \rightarrow ZH) \times \mathcal{B}(H \rightarrow b\bar{b})$  for gluon-gluon fusion (a); observed and expected 95% CL exclusion regions in the  $m_H$  vs.  $m_A$  plane for various  $\tan\beta$  values for Type-II 2HDM (b) [121].

## Conclusions

The existence of new physics is strongly suggested by the inability of the Standard Model (SM) to explain in a satisfactory way some observed phenomena, and a large programme of experimental research is currently ongoing focusing on the quest for new particles. In this context, the analysis presented in this thesis aims at searching for two additional Higgs bosons  $H$  and  $A$ , predicted in the two-Higgs-doublet model (2HDM), which is built by adding a second Higgs doublet to the SM scalar sector. The search is performed via the decay chain  $H \rightarrow ZA$ , with the  $Z$  boson decaying to a pair of leptons and the  $A$  boson decaying to a pair of  $b$  quarks, on the data collected by the CMS experiment in 2016 with a center-of-mass energy of 13 TeV and an integrated luminosity of  $35.9 \text{ fb}^{-1}$ . A search for an excess of events is performed in the plane defined by the reconstructed invariant masses of the two  $b$  jets ( $m_{jj}$ ), and of the two leptons and the two  $b$  jets ( $m_{\ell\ell jj}$ ). This introduces an inherent correlation in the two-dimensional mass distribution of the signal. The main feature of the search is the definition of elliptical signal regions exploiting such correlation in order to optimize the sensitivity of the analysis.

Upper limits are set on the product of the signal production cross section and branching ratio. The results are then interpreted in the context of the Type-II 2HDM, and exclude masses of the bosons ranging from  $\sim 200 \text{ GeV}$  to  $\sim 700 \text{ GeV}$  under the benchmark  $\cos(\beta - \alpha) = 0.01$  and  $\tan\beta = 1$ ; and values of  $\cos(\beta - \alpha)$  ranging from approximately  $-0.9$  to  $0.3$  and of  $\tan\beta$  from approximately  $0.5$  to  $7.0$  under the benchmark  $m_H = 379 \text{ GeV}$  and  $m_A = 172 \text{ GeV}$  at 95% CL. The highest local significance observed in the search amounts to  $3.9\sigma$ , corresponding to the signal hypothesis  $(m_H, m_A) = (627, 162) \text{ GeV}$ . This is then reduced to  $1.3\sigma$  once the look-elsewhere effect [95] is quantified in two dimensions, making the excess not statistically significant.

The analysis provides stronger constraints on the parameters of the 2HDM with respect to the search conducted on data collected during the Run 1 data-taking [4] by the CMS Collaboration at the Large Hadron Collider (LHC). This is due to both the optimization of the analysis strategy and the increase of integrated luminosity. Moreover, the sensitivity provided by the analysis is comparable to the one obtained by the ATLAS Collaboration on the search for an  $A$  boson via the cascade decay  $A \rightarrow Z(\rightarrow \ell^+ \ell^-) H(\rightarrow b\bar{b})$  [121]. Unlike the ATLAS search, the  $b$ -associated production mode of the signal is not accounted for in the search presented in this thesis, as it is sub-dominant at low values of  $\tan\beta$ . However, its inclusion in the analysis would increase the exclusion

power at high values of  $\tan\beta$  and should be considered for the search that will be conducted on the full Run 2 dataset.

An application of the Matrix Element Method (MEM) for estimate of the Wilson coefficient  $c_{Qq}^{11}$  of the Standard Model Effective Field Theory (SMEFT) is also presented. The MEM represents a powerful tool for statistical parameter inference, as it provides a direct connection between the underlying physics processes and the detector-level physical observables. The MEM weights are computed with MoMEMt [7], a software specifically designed to facilitate the applicability of the MEM and speed up its computation. The study is presented as a proof of concept. A fully-leptonic  $t\bar{t}$  sample is simulated under the SM hypothesis, where the value of the Wilson coefficient is trivially zero. A minimization of the negative log-likelihood yields values compatible with the true one within the  $1\sigma$  confidence interval. The results are promising and might lead to future applications to data analyses.

During Run 2, the LHC has provided an integrated luminosity of  $\sim 150 \text{ fb}^{-1}$ . The increase in the statistics of the data to be analyzed, together with improved analysis techniques, are key for an improvement in the sensitivity of future searches, allowing to set stronger constraints on the parameters of BSM models. If no significant deviation from the Standard Model is found, the hypothesis that masses of new particles might be lying at very high energy scales becomes more and more legitimate. In this context, future particle accelerators that aim at probing much higher energy scales than the LHC one play a key role together with indirect searches and precision measurements, that represent a valuable, complementary way to direct searches in the ultimate goal of finding new physics.

## References

- [1] ATLAS Collaboration, “Observation of a new particle in the search for the Standard Model Higgs boson with the ATLAS detector at the LHC”, *Phys. Lett.* **B716** (2012) 1–29. doi:10.1016/j.physletb.2012.08.020, arXiv:1207.7214.
- [2] CMS Collaboration, “Observation of a New Boson at a Mass of 125 GeV with the CMS Experiment at the LHC”, *Phys. Lett.* **B716** (2012) 30–61. doi:10.1016/j.physletb.2012.08.021, arXiv:1207.7235.
- [3] G. C. Branco et al., “Theory and phenomenology of two-Higgs-doublet models”, *Phys. Rept.* **516** (2012) 1–102. doi:10.1016/j.physrep.2012.02.002, arXiv:1106.0034.
- [4] CMS Collaboration, “Search for H to Z(l)l+A(bb) with 2015 data”, Technical Report CMS-PAS-HIG-16-010, 2016. <https://cds.cern.ch/record/2140613>.
- [5] N. P. Hartland et al., “A Monte Carlo global analysis of the Standard Model Effective Field Theory: the top quark sector”, *JHEP* **04** (2019) 100. doi:10.1007/JHEP04(2019)100, arXiv:1901.05965.
- [6] M. F. Canelli, “Helicity of the W boson in single - lepton  $t\bar{t}$  events”, PhD thesis, Rochester U. [http://lss.fnal.gov/cgi-bin/find\\_paper.pl?thesis-2003-22](http://lss.fnal.gov/cgi-bin/find_paper.pl?thesis-2003-22).
- [7] S. Brochet et al., “MoMEMta, a modular toolkit for the Matrix Element Method at the LHC”, *Eur. Phys. J.* **C79** (2019), no. 2, 126. doi:10.1140/epjc/s10052-019-6635-5, arXiv:1805.08555.
- [8] ATLAS Collaboration, “Measurement of the W-boson mass in pp collisions at  $\sqrt{s} = 7$  TeV with the ATLAS detector”, *Eur. Phys. J.* **C78** (2018), no. 2, 110. doi:10.1140/epjc/s10052-018-6354-3, 10.1140/epjc/s10052-017-5475-4, arXiv:1701.07240. [Erratum: *Eur. Phys. J.*C78,no.11,898(2018)].
- [9] CMS Collaboration, “W-like measurement of the Z boson mass using dimuon events collected in pp collisions at  $\sqrt{s} = 7$  TeV”, Technical Report CMS-PAS-SMP-14-007, 2016. <https://cds.cern.ch/record/2139655>.
- [10] P. W. Higgs, “Broken Symmetries and the Masses of Gauge Bosons”, *Phys. Rev. Lett.* **13** (Oct, 1964) 508–509. doi:10.1103/PhysRevLett.13.508.

- [11] F. Englert et al., “Broken Symmetry and the Mass of Gauge Vector Mesons”, *Phys. Rev. Lett.* **13** (Aug, 1964) 321–323. doi:10.1103/PhysRevLett.13.321.
- [12] G. S. Guralnik et al., “Global Conservation Laws and Massless Particles”, *Phys. Rev. Lett.* **13** (Nov, 1964) 585–587. doi:10.1103/PhysRevLett.13.585.
- [13] P. Langacker, “The standard model and beyond; 2nd ed.”. High energy physics, cosmology and gravitation. CRC Press, <https://cds.cern.ch/record/2256595>.
- [14] M. Herrero, “The Higgs System in and Beyond the Standard Model”, *Springer Proc. Phys.* **161** (2015) 188–252. doi:10.1007/978-3-319-12238-0\_5, arXiv:1401.7270.
- [15] ATLAS Collaboration, “The ATLAS Experiment at the CERN Large Hadron Collider”, *JINST* **3** (2008) S08003. doi:10.1088/1748-0221/3/08/S08003.
- [16] CMS Collaboration, “The CMS Experiment at the CERN LHC”, *JINST* **3** (2008) S08004. doi:10.1088/1748-0221/3/08/S08004.
- [17] CMS Collaboration, “Measurements of properties of the Higgs boson decaying into the four-lepton final state in pp collisions at  $\sqrt{s} = 13$  TeV”, *JHEP* **11** (2017) 047. doi:10.1007/JHEP11(2017)047, arXiv:1706.09936.
- [18] ATLAS Collaboration, “Measurement of the Higgs boson mass in the  $H \rightarrow ZZ^* \rightarrow 4\ell$  and  $H \rightarrow \gamma\gamma$  channels with  $\sqrt{s} = 13$  TeV pp collisions using the ATLAS detector”, *Phys. Lett. B* **784** (2018) 345. doi:10.1016/j.physletb.2018.07.050, arXiv:1806.00242.
- [19] ATLAS, CMS Collaboration, “Combined Measurement of the Higgs Boson Mass in pp Collisions at  $\sqrt{s} = 7$  and 8 TeV with the ATLAS and CMS Experiments”, *Phys. Rev. Lett.* **114** (2015) 191803. doi:10.1103/PhysRevLett.114.191803, arXiv:1503.07589.
- [20] “SM Higgs production cross sections at  $\sqrt{s} = 13 - 14$  TeV”. <https://twiki.cern.ch/twiki/bin/view/LHCPhysics/CERNYellowReportPageAt1314TeV2014>.
- [21] H. M. Georgi et al., “Higgs Bosons from Two Gluon Annihilation in Proton Proton Collisions”, *Phys. Rev. Lett.* **40** (1978) 692. doi:10.1103/PhysRevLett.40.692.
- [22] LHC Higgs Cross Section Working Group, “Handbook of LHC Higgs Cross Sections: 1. Inclusive Observables”. CERN Yellow Reports: Monographs. CERN, Geneva, <http://cds.cern.ch/record/1318996>. Comments: 153 pages, 43 figures, to be submitted to CERN Report. Working Group web page: <https://twiki.cern.ch/twiki/bin/view/LHCPhysics/CrossSections>.

- [23] J. D. Wells, "Higgs naturalness and the scalar boson proliferation instability problem", *Synthese* **194** (2017), no. 2, 477–490. doi:10.1007/s11229-014-0618-8, arXiv:1603.06131.
- [24] G. F. Giudice, "Naturally Speaking: The Naturalness Criterion and Physics at the LHC",. doi:10.1142/9789812779762\_0010, arXiv:0801.2562.
- [25] L. Bergstrom, "Dark Matter Evidence, Particle Physics Candidates and Detection Methods", *Annalen Phys.* **524** (2012) 479–496. doi:10.1002/andp.201200116, arXiv:1205.4882.
- [26] G. Bertone et al., "Particle dark matter: Evidence, candidates and constraints", *Phys. Rept.* **405** (2005) 279–390. doi:10.1016/j.physrep.2004.08.031, arXiv:hep-ph/0404175.
- [27] F. Zwicky, "Die Rotverschiebung von extragalaktischen Nebeln", *Helv. Phys. Acta* **6** (1933) 110–127. doi:10.1007/s10714-008-0707-4. [Gen. Rel. Grav.41,207(2009)].
- [28] G. Bertone et al., "History of dark matter", *Rev. Mod. Phys.* **90** (2018), no. 4, 045002. doi:10.1103/RevModPhys.90.045002, arXiv:1605.04909.
- [29] A. B. McDonald, "Evidence for neutrino oscillations. I. Solar and reactor neutrinos", *Nucl. Phys.* **A751** (2005) 53–66. doi:10.1016/j.nuclphysa.2005.02.102, arXiv:nucl-ex/0412005.
- [30] Super-Kamiokande Collaboration, "Evidence for oscillation of atmospheric neutrinos", *Phys. Rev. Lett.* **81** (1998) 1562–1567. doi:10.1103/PhysRevLett.81.1562, arXiv:hep-ex/9807003.
- [31] A. D. Sakharov, "Violation of CP Invariance, C asymmetry, and baryon asymmetry of the universe", *Pisma Zh. Eksp. Teor. Fiz.* **5** (1967) 32–35. doi:10.1070/PU1991v034n05ABEH002497. [Usp. Fiz. Nauk161,no.5,61(1991)].
- [32] G. Degrandi et al., "Higgs mass and vacuum stability in the Standard Model at NNLO", *JHEP* **08** (2012) 098. doi:10.1007/JHEP08(2012)098, arXiv:1205.6497.
- [33] R. D. Peccei, "The Strong CP problem and axions", *Lect. Notes Phys.* **741** (2008) 3–17. doi:10.1007/978-3-540-73518-2\_1, arXiv:hep-ph/0607268. [3(2006)].
- [34] R. D. Peccei et al., "CP Conservation in the Presence of Instantons", *Phys. Rev. Lett.* **38** (1977) 1440–1443. doi:10.1103/PhysRevLett.38.1440. [328(1977)].
- [35] M. Trodden, "Electroweak baryogenesis: A Brief review", in *Proceedings, 33rd Rencontres de Moriond 98 electroweak interactions and unified theories: Les Arcs, France, Mar 14-21, 1998*, pp. 471–480. 1998. arXiv:hep-ph/9805252.

- [36] H. E. Haber et al., “The Search for Supersymmetry: Probing Physics Beyond the Standard Model”, *Phys. Rept.* **117** (1985) 75–263. doi:10.1016/0370-1573(85)90051-1.
- [37] I. F. Ginzburg et al., “Symmetries of two Higgs doublet model and CP violation”, *Phys. Rev.* **D72** (2005) 115013. doi:10.1103/PhysRevD.72.115013, arXiv:hep-ph/0408011.
- [38] A. Arhrib et al., “Double Neutral Higgs production in the Two-Higgs doublet model at the LHC”, *JHEP* **08** (2009) 035. doi:10.1088/1126-6708/2009/08/035, arXiv:0906.0387.
- [39] M. Carena et al., “Higgs Boson Theory and Phenomenology”, *Prog. Part. Nucl. Phys.* **50** (2003) 63–152. doi:10.1016/S0146-6410(02)00177-1, arXiv:hep-ph/0208209.
- [40] S. L. Glashow et al., “Natural Conservation Laws for Neutral Currents”, *Phys. Rev.* **D15** (1977) 1958. doi:10.1103/PhysRevD.15.1958.
- [41] P. Langacker, “Grand Unified Theories and Proton Decay”, *Phys. Rept.* **72** (1981) 185. doi:10.1016/0370-1573(81)90059-4.
- [42] Particle Data Group Collaboration, “Review of particle physics”, *J. Phys.* **G37** (2010) 075021. doi:10.1088/0954-3899/37/7A/075021.
- [43] N. Craig et al., “The Hunt for the Rest of the Higgs Bosons”, *JHEP* **06** (2015) 137. doi:10.1007/JHEP06(2015)137, arXiv:1504.04630.
- [44] CMS Collaboration, “Combined measurements of the Higgs boson’s couplings at  $\sqrt{s} = 13$  TeV”, Technical Report CMS-PAS-HIG-17-031, 2018. <https://cds.cern.ch/record/2308127>.
- [45] D. Chowdhury et al., “Update of Global Two-Higgs-Doublet Model Fits”, *JHEP* **05** (2018) 161. doi:10.1007/JHEP05(2018)161, arXiv:1711.02095.
- [46] A. V. Manohar, “Introduction to Effective Field Theories”, in *Les Houches summer school: EFT in Particle Physics and Cosmology Les Houches, Chamonix Valley, France, July 3-28, 2017*. 2018. arXiv:1804.05863.
- [47] G. Passarino et al., “The Standard Model Effective Field Theory and Next to Leading Order”, (2016). arXiv:1610.08356.
- [48] C. Degrande et al., “Effective Field Theory: A Modern Approach to Anomalous Couplings”, *Annals Phys.* **335** (2013) 21–32. doi:10.1016/j.aop.2013.04.016, arXiv:1205.4231.
- [49] ALICE Collaboration, “The ALICE experiment at the CERN LHC”, *JINST* **3** (2008) S08002. doi:10.1088/1748-0221/3/08/S08002.
- [50] LHCb Collaboration, “The LHCb Detector at the LHC”, *JINST* **3** (2008) S08005. doi:10.1088/1748-0221/3/08/S08005.

- [51] E. Mobs, "The CERN accelerator complex. Complexe des accélérateurs du CERN", (Jul, 2016). <https://cds.cern.ch/record/2197559>. General Photo.
- [52] H. Bartosik et al., "Performance potential of the injectors after LS1", Technical Report CERN-2012-006, 2012. <https://cds.cern.ch/record/1492996>.
- [53] O. S. Brüning et al., "LHC Design Report". CERN Yellow Reports: Monographs. CERN, Geneva, <https://cds.cern.ch/record/782076>.
- [54] "CMS luminosity - public results". [twiki.cern.ch/twiki/bin/view/CMSPublic/LumiPublicResults](https://twiki.cern.ch/twiki/bin/view/CMSPublic/LumiPublicResults). Accessed on 20/11/2017.
- [55] G. Apollinari et al., "High-Luminosity Large Hadron Collider (HL-LHC)", *CERN Yellow Rep. Monogr.* **4** (2017) 1–516. doi:10.23731/CYRM-2017-004.
- [56] A. Barachetti et al., "Final Project Report: Deliverable D1.14", (Jan, 2016). <https://cds.cern.ch/record/2120851>.
- [57] P. A. Cherenkov, "Visible emission of clean liquids by action of  $\gamma$  radiation", *Doklady Akademii Nauk SSSR* **2** (1934), no. 451, 252.
- [58] CMS Collaboration, "CMS Physics: Technical Design Report Volume 1: Detector Performance and Software", Technical Report CERN-LHCC-2006-001. CMS-TDR-8-1, 2006. <https://cds.cern.ch/record/922757>.
- [59] T. Sakuma et al., "Detector and Event Visualization with SketchUp at the CMS Experiment", *J. Phys. Conf. Ser.* **513** (2014) 022032. doi:10.1088/1742-6596/513/2/022032, arXiv:1311.4942.
- [60] "CMS tracker material budget plots". [twiki.cern.ch/twiki/bin/view/CMSPublic/TrackerMaterialBudgetplots](https://twiki.cern.ch/twiki/bin/view/CMSPublic/TrackerMaterialBudgetplots).
- [61] M. Chaichian et al., "An Essay on color confinement", (1999). arXiv:hep-th/9909158.
- [62] CMS Collaboration, "The CMS electromagnetic calorimeter project: Technical Design Report". Technical Design Report CMS. CERN, Geneva, 1997. <http://cds.cern.ch/record/349375>.
- [63] CMS Collaboration, "Performance of CMS Hadron Calorimeter Timing and Synchronization using Test Beam, Cosmic Ray, and LHC Beam Data", *JINST* **5** (2010) T03013. doi:10.1088/1748-0221/5/03/T03013, arXiv:0911.4877.
- [64] CMS Collaboration, "The CMS hadron calorimeter project: Technical Design Report". Technical Design Report CMS. CERN, Geneva, 1997. <http://cds.cern.ch/record/357153>. The following files are from [http://uscms.fnal.gov/pub/hcal\\_tdr](http://uscms.fnal.gov/pub/hcal_tdr) and may not be the version as printed, please check the printed version to be sure.

- [65] CMS HCAL Collaboration, “Design, performance, and calibration of CMS hadron-barrel calorimeter wedges”, *Eur. Phys. J.* **C55** (2008), no. 1, 159–171. doi:10.1140/epjc/s10052-008-0573-y.
- [66] M. Shopova et al., “Performance of Resistive Plate Chambers installed during the first long shutdown of the CMS experiment”, in *Proceedings, 13th Workshop on Resistive Plate Chambers and Related Detectors (RPC2016): Ghent, Belgium, February 22-26, 2016*. 2016. arXiv:1605.06798.
- [67] CMS Collaboration, “The CMS muon project: Technical Design Report”. Technical Design Report CMS. CERN, Geneva, 1997. <https://cds.cern.ch/record/343814>.
- [68] CMS Collaboration, “CMS Technical Design Report for the Level-1 Trigger Upgrade”, Technical Report CERN-LHCC-2013-011. CMS-TDR-12, Jun, 2013. <https://cds.cern.ch/record/1556311>. Additional contacts: Jeffrey Spalding, Fermilab, Jeffrey.Spalding@cern.ch Didier Contardo, Universite Claude Bernard-Lyon I, didier.claude.contardo@cern.ch.
- [69] CMS Collaboration, “The CMS trigger system”, *JINST* **12** (2017), no. 01, P01020. doi:10.1088/1748-0221/12/01/P01020, arXiv:1609.02366.
- [70] CMS Collaboration, “Particle-flow reconstruction and global event description with the CMS detector”, *JINST* **12** (2017), no. 10, P10003. doi:10.1088/1748-0221/12/10/P10003, arXiv:1706.04965.
- [71] CMS Collaboration, “Commissioning and Performance of the CMS Silicon Strip Tracker with Cosmic Ray Muons”, *JINST* **5** (2010) T03008. doi:10.1088/1748-0221/5/03/T03008, arXiv:0911.4996.
- [72] T. Bergauer, “Design, Construction and Commissioning of the CMS Tracker at CERN and Proposed Improvements for Detectors at the Future International Linear Collider”, PhD thesis, Vienna, Tech. U. 2008.
- [73] CMS Collaboration, “Description and performance of track and primary-vertex reconstruction with the CMS tracker”, *JINST* **9** (2014), no. 10, P10009. doi:10.1088/1748-0221/9/10/P10009, arXiv:1405.6569.
- [74] CMS Collaboration, “Performance of Electron Reconstruction and Selection with the CMS Detector in Proton-Proton Collisions at  $\sqrt{s} = 8$  TeV”, *JINST* **10** (2015), no. 06, P06005. doi:10.1088/1748-0221/10/06/P06005, arXiv:1502.02701.
- [75] E. Meschi et al., “Electron Reconstruction in the CMS Electromagnetic Calorimeter”, Technical Report CMS-NOTE-2001-034, Jun, 2001. <https://cds.cern.ch/record/687345>.
- [76] CMS Collaboration, “Performance of the CMS muon detector and muon reconstruction with proton-proton collisions at  $\sqrt{s} = 13$  TeV”, *JINST* **13** (2018), no. 06, P06015. doi:10.1088/1748-0221/13/06/P06015, arXiv:1804.04528.

- [77] E. James et al., “Muon Identification in CMS”, Technical Report CMS-NOTE-2006-010, Jan, 2006. <http://cds.cern.ch/record/927392>.
- [78] M. Cacciari et al., “The anti- $k_t$  jet clustering algorithm”, *JHEP* **04** (2008) 063. doi:10.1088/1126-6708/2008/04/063, arXiv:0802.1189.
- [79] M. Cacciari et al., “FastJet user manual”, *Eur. Phys. J. C* **72** (2012) 1896. doi:10.1140/epjc/s10052-012-1896-2, arXiv:1111.6097.
- [80] CMS Collaboration, “The Jet Plus Tracks Algorithm for Calorimeter Jet Energy Corrections in CMS”, Technical Report CMS-PAS-JME-09-002, 2009. <https://cds.cern.ch/record/1190234>.
- [81] CMS Collaboration, “Determination of Jet Energy Calibration and Transverse Momentum Resolution in CMS”, *JINST* **6** (2011) P11002. doi:10.1088/1748-0221/6/11/P11002, arXiv:1107.4277.
- [82] CMS Collaboration, “Measurements of the CMS jet energy scale and resolution at 13 TeV”, Technical Report CMS-CR-2018-216, Sep, 2018. <https://cds.cern.ch/record/2646769>.
- [83] CMS Collaboration, “Identification of heavy-flavour jets with the CMS detector in pp collisions at 13 TeV”, *JINST* **13** (2018), no. 05, P05011. doi:10.1088/1748-0221/13/05/P05011, arXiv:1712.07158.
- [84] CMS Collaboration, “Heavy flavor identification at CMS with deep neural networks”, (Mar, 2017). <https://cds.cern.ch/record/2255736>.
- [85] CMS Collaboration, “Missing transverse energy performance of the CMS detector”, *JINST* **6** (2011) P09001. doi:10.1088/1748-0221/6/09/P09001, arXiv:1106.5048.
- [86] CMS Collaboration, “CMS Offline Software”. <https://github.com/cms-sw/cmssw>.
- [87] GEANT4 Collaboration, “GEANT4: A Simulation toolkit”, *Nucl. Instrum. Meth. A* **506** (2003) 250–303. doi:10.1016/S0168-9002(03)01368-8.
- [88] J. Alwall et al., “The automated computation of tree-level and next-to-leading order differential cross sections, and their matching to parton shower simulations”, *JHEP* **07** (2014) 079. doi:10.1007/JHEP07(2014)079, arXiv:1405.0301.
- [89] S. Alioli et al., “A general framework for implementing NLO calculations in shower Monte Carlo programs: the POWHEG BOX”, *JHEP* **06** (2010) 043. doi:10.1007/JHEP06(2010)043, arXiv:1002.2581.
- [90] T. Sjöstrand et al., “An Introduction to PYTHIA 8.2”, *Comput. Phys. Commun.* **191** (2015) 159–177. doi:10.1016/j.cpc.2015.01.024, arXiv:1410.3012.

- [91] CMS Collaboration, “Measurement of the inclusive W and Z production cross sections in pp collisions at  $\sqrt{s} = 7\text{TeV}$  with the CMS experiment”, *JHEP* **10** (2011) 132. doi:10.1007/JHEP10(2011)132, arXiv:1107.4789.
- [92] K. Cranmer, “Practical Statistics for the LHC”, in *Proceedings, 2011 European School of High-Energy Physics (ESHEP 2011): Cheile Gradistei, Romania, September 7-20, 2011*, number 247, pp. 267 – 308. 2015. arXiv:1503.07622.
- [93] J. Neyman et al., “On the Problem of the Most Efficient Tests of Statistical Hypotheses”, *Phil. Trans. R. Soc. Lond. A* **231** (1933), no. 694-706, 289–337. doi:10.1098/rsta.1933.0009.
- [94] A. L. Read, “Presentation of search results: The  $CL_s$  technique”, *J. Phys.* **G28** (2002), no. 11, 2693–2704. doi:10.1088/0954-3899/28/10/313.
- [95] E. Gross et al., “Trial factors for the look elsewhere effect in high energy physics”, *Eur. Phys. J.* **C70** (2010) 525–530. doi:10.1140/epjc/s10052-010-1470-8, arXiv:1005.1891.
- [96] E. Gross, “Practical Statistics for High Energy Physics”, *CERN Yellow Reports: School Proceedings* **4** (2017), no. 0, 165.
- [97] ATLAS Collaboration, “Observation of an Excess of Events in the Search for the Standard Model Higgs boson with the ATLAS detector at the LHC”, Technical Report ATLAS-CONF-2012-093, Jul, 2012. <https://cds.cern.ch/record/1460439>.
- [98] O. Vitells et al., “Estimating the significance of a signal in a multi-dimensional search”, *Astropart. Phys.* **35** (2011) 230–234. doi:10.1016/j.astropartphys.2011.08.005, arXiv:1105.4355.
- [99] B. Grzadkowski et al., “Dimension-Six Terms in the Standard Model Lagrangian”, *JHEP* **10** (2010) 085. doi:10.1007/JHEP10(2010)085, arXiv:1008.4884.
- [100] C. Zhang, “Constraining  $qqtt$  operators from four-top production: a case for enhanced EFT sensitivity”, *Chin. Phys.* **C42** (2018), no. 2, 023104. doi:10.1088/1674-1137/42/2/023104, arXiv:1708.05928.
- [101] F. Fiedler et al., “The Matrix Element Method and its Application in Measurements of the Top Quark Mass”, *Nucl. Instrum. Meth.* **A624** (2010) 203–218. doi:10.1016/j.nima.2010.09.024, arXiv:1003.1316.
- [102] P. Artoisenet et al., “Automation of the matrix element reweighting method”, *JHEP* **12** (2010) 068. doi:10.1007/JHEP12(2010)068, arXiv:1007.3300.
- [103] T. Ohl, “Vegas revisited: Adaptive Monte Carlo integration beyond factorization”, *Comput. Phys. Commun.* **120** (1999) 13–19. doi:10.1016/S0010-4655(99)00209-X, arXiv:hep-ph/9806432.

- [104] T. Hahn, “Cuba-a library for multidimensional numerical integration”, *Computer Physics Communications* **168** (2005), no. 2, 78 – 95. doi:<https://doi.org/10.1016/j.cpc.2005.01.010>.
- [105] DELPHES 3 Collaboration, “DELPHES 3, A modular framework for fast simulation of a generic collider experiment”, *JHEP* **02** (2014) 057. doi:[10.1007/JHEP02\(2014\)057](https://doi.org/10.1007/JHEP02(2014)057), arXiv:1307.6346.
- [106] D0 Collaboration, “A precision measurement of the mass of the top quark”, *Nature* **429** (2004) 638–642. doi:[10.1038/nature02589](https://doi.org/10.1038/nature02589), arXiv:hep-ex/0406031.
- [107] J. C. Estrada Vigil, “Maximal use of kinematic information for the extraction of the mass of the top quark in single-lepton  $t$  anti- $t$  events at D0”, PhD thesis, Rochester U. [http://lss.fnal.gov/cgi-bin/find\\_paper.pl?thesis-2001-07](http://lss.fnal.gov/cgi-bin/find_paper.pl?thesis-2001-07).
- [108] NNPDF Collaboration, “Parton distributions for the LHC Run II”, *JHEP* **04** (2015) 040. doi:[10.1007/JHEP04\(2015\)040](https://doi.org/10.1007/JHEP04(2015)040), arXiv:1410.8849.
- [109] R. V. Harlander et al., “SusHi: A program for the calculation of Higgs production in gluon fusion and bottom-quark annihilation in the Standard Model and the MSSM”, *Comput. Phys. Commun.* **184** (2013) 1605–1617. doi:[10.1016/j.cpc.2013.02.006](https://doi.org/10.1016/j.cpc.2013.02.006), arXiv:1212.3249.
- [110] D. Eriksson et al., “2HDMC: Two-Higgs-Doublet Model Calculator Physics and Manual”, *Comput. Phys. Commun.* **181** (2010) 189–205. doi:[10.1016/j.cpc.2009.09.011](https://doi.org/10.1016/j.cpc.2009.09.011), arXiv:0902.0851.
- [111] R. Frederix et al., “Merging meets matching in MC@NLO”, *JHEP* **12** (2012) 061. doi:[10.1007/JHEP12\(2012\)061](https://doi.org/10.1007/JHEP12(2012)061), arXiv:1209.6215.
- [112] P. Artoisenet et al., “Automatic spin-entangled decays of heavy resonances in Monte Carlo simulations”, *JHEP* **03** (2013) 015. doi:[10.1007/JHEP03\(2013\)015](https://doi.org/10.1007/JHEP03(2013)015), arXiv:1212.3460.
- [113] E. G. Ferreira, “Quarkonium: a theory overview”, *Nucl. Phys.* **A982** (2019) 127–133. doi:[10.1016/j.nuclphysa.2018.12.002](https://doi.org/10.1016/j.nuclphysa.2018.12.002), arXiv:1810.00477.
- [114] CMS Collaboration, “Search for neutral resonances decaying into a Z boson and a pair of b jets or  $\tau$  leptons”, *Phys. Lett.* **B759** (2016) 369–394. doi:[10.1016/j.physletb.2016.05.087](https://doi.org/10.1016/j.physletb.2016.05.087), arXiv:1603.02991.
- [115] A. Hoecker et al., “TMVA - Toolkit for Multivariate Data Analysis”, 2007. arXiv:physics/0703039.
- [116] CMS Collaboration, “Search for new neutral Higgs bosons through the  $H \rightarrow ZA \rightarrow \ell^+ \ell^- b \bar{b}$  process in pp collisions at  $\sqrt{s} = 13$  TeV”, (2019). arXiv:1911.03781.
- [117] B. Martin et al., “Particle Physics”. Manchester Physics Series. Wiley, 2008. <https://books.google.be/books?id=whIbrWJdEJQC>.

- [118] S. Bifani et al., “Review of Lepton Universality tests in  $B$  decays”, *J. Phys.* **G46** (2019), no. 2, 023001. doi:10.1088/1361-6471/aaf5de, arXiv:1809.06229.
- [119] LHCb Collaboration, “Search for lepton-universality violation in  $B^+ \rightarrow K^+ \ell^+ \ell^-$  decays”, *Phys. Rev. Lett.* **122** (2019), no. 19, 191801. doi:10.1103/PhysRevLett.122.191801, arXiv:1903.09252.
- [120] K. S. Cranmer, “Kernel estimation in high-energy physics”, *Comput. Phys. Commun.* **136** (2001) 198–207. doi:10.1016/S0010-4655(00)00243-5, arXiv:hep-ex/0011057.
- [121] ATLAS Collaboration, “Search for a heavy Higgs boson decaying into a  $Z$  boson and another heavy Higgs boson in the  $\ell\ell b\bar{b}$  final state in  $pp$  collisions at  $\sqrt{s} = 13$  TeV with the ATLAS detector”, *Phys. Lett.* **B783** (2018) 392–414. doi:10.1016/j.physletb.2018.07.006, arXiv:1804.01126.
- [122] G. C. Dorsch et al., “Echoes of the Electroweak Phase Transition: Discovering a second Higgs doublet through  $A_0 \rightarrow ZH_0$ ”, *Phys. Rev. Lett.* **113** (2014), no. 21, 211802. doi:10.1103/PhysRevLett.113.211802, arXiv:1405.5537.